Università
Ca'Foscari
Venezia

cmcc
Centro Euro-Mediterraneo
sui Cambiamenti Climatici

Ca' Foscari Università di Venezia

and

Centro Euro-Mediterraneo sui Cambiamenti
Climatici

Numerical modelling of the benthic-pelagic coupling in coastal marine ecosystems at contrasting sites

Corso di Dottorato di ricerca in Science and Management of Climate Change
Ciclo 32
SSD: GEO12

Ph.D. Coordinator:
Carlo Carraro

Supervisor:
Simona Masina

Ph.D. Candidate:
Carolina Amadio
Ph.D. Matriculation number:
956323

Cosupervisors:
Marco Zavatarelli
Tomas Lovato
Momme Butenschon

December, 2019

Abstract

Continental shelves (bottom depth <150-200m) cover less than 5% of the global ocean surface, but play a crucial role in the marine global biogeochemical cycling. Coastal waters biogeochemical cycling is governed and constrained by the biogeochemical processes occurring in the benthic domain. Such processes define the so called benthic-pelagic coupling (hereafter BPC), i.e. two-way exchange of organic matter (particulate and dissolved) and inorganic compounds. The physically mediated exchanges structuring the BPC are constituted by the sinking and resuspension fluxes of particulate organic matter and by the diffusion of inorganic nutrients. Despite the importance of the benthic domain for the coastal water ecosystems and the continuous enhancement of model resolution, BPC in marine ecosystem models is in general approximated through a simple closure term for mass conservation. Moreover, observational data focusing on the BPC dynamics are scanty and sparse both in time and space, thereby hampering model parameterization and validation. The main objectives of this study are (i) develop and test a detailed numerical model addressing benthic dynamics and BPC processes (ii), assess the skills of the coupled physical-biogeochemical models in simulating the BPC and (iii) evaluate ecosystem dynamics in marine areas with different climatic and ecological characteristics. The benthic

sub-model implemented is based on two crucial parameters: the sinking velocity of particulate matter and the diffusive fluxes of inorganic dissolved matter at the benthic-pelagic interface. The benthic sub-model has been calibrated accounting for the complex pelagic food web and for the main ecological and physical characteristics of continental shelf areas. The model has been implemented in different sites: Gulf of Trieste (Italy), St Helena Bay (South Africa), Svinøy Fyr (Norway). At each implementation site, the one-dimensional coupled BFM-NEMO modelling system was setup with prescribed temperature and salinity vertical profiles and surface wind stress as forcing for NEMO, while the surface incident shortwave radiation acts as forcing for the BFM. Model results have been compared with in situ data. A set of sensitivity tests has been performed, for each station, to investigate the role of benthic remineralization and organic matter deposition in the determination of the macronutrient seasonal cycling and primary producer biomass and to carry out a comparative analysis between the obtained results and the ecological and environmental site specific characteristics.

Contents

Chapter 1

Overview

1.1 Overview

Covering about the 70% of the Earth's surface, interacting with atmosphere, cryosphere, land, and biosphere, the oceans have a deep influence on the climate system. Oceans ability to store and transport large amounts of energy, heat and organic/inorganic matter across time and space scales, depending on the region, depth and nature of interaction with the atmosphere, acts as a giant flywheel to the climate system, moderating change but prolonging it once change commences [1]. The amount of heat stored, the pathways and mechanisms of heat transport around the globe (through currents, eddies and gyres) are critical issues in understanding the present state of climate system and its future changes [2]. Moreover, the oceans role in the climate system is enhanced by the fact that oceans are (trough physico-chemical and biological processes) a large carbon sink.

Starting from the past century, there has been a growing interest about the development of numerical models of the climate system representing, de-

tecting and predicting the ocean dynamics at different spatial and temporal scales.

Simulating the large-scale patterns of ocean circulation and water masses properties distribution is pivotal to understand the climate system dynamics, to provide a quantitative framework for assessing the contributions of different processes, and to interpret ocean observations [3, 4, 5, 6]. Numerical simulations also are one of the few tools available for making projections of the responses and feedbacks of the marine carbon system to past and future climate change [7, 5, 8, 9].

Given the need to understand the present climate system dynamics driven by the 'global warming' issue, the Earth System Models are experiencing improvements derived from the enhanced coupled atmosphere-ocean model spatial resolution, from the improvement of the global data service network and from the increased high spatial and temporal resolution data availability [10]. This improvements, supported by the increasing computing capabilities, better data assimilation techniques and the development of more complex models, is paving the way to the so called 'environmental predictions', namely the attempt to predict the dynamics of the biogeochemical state variables not traditionally included in numerical models [10].

The focus on the ocean biogeochemical dynamics is motivated by the fact that approximately the 93% of the carbon dioxide pool is located in the oceans (pre-industrial period) likely influencing the future CO_2 atmospheric concentration [11].

Despite the continuous improvements of numerical models, the representation of shelf and coastal seas is still poorly constrained in the present generation of Earth System Models because of the still coarse spatial resolution and the processes representation. According to [12] the coarse grid

spacing of the Ocean General Circulation Models (OGCM's) can represent only the largest dominant scale processes affecting shelf dynamics while vertical turbulent processes require finer resolution.

On the biogeochemical side, coastal waters properties are strongly depending on the interactions and boundary fluxes at the sea floor, atmosphere and land interfaces. This has a strong connection with the global (present and future) climate state.

Coastal waters host the world's most productive ecosystems, providing 30% of the global primary production, 80% of the organic matter burial and 50% of the marine denitrification [13]. All these processes occur in the marine ecosystem which is usually divided into two different interacting compartments: the pelagic (water column) and the benthic (seabed) environment. The two-way exchanges of energy and matter occurring between the seafloor and the overlying water column, define the so called Benthic-Pelagic Coupling (hereafter BPC), that plays an important role in determining the pelagic biogeochemical characteristics of coastal waters [14, 15].

Despite its importance, there are significant gaps in our understanding of the inorganic nutrient and organic matter fluxes between the benthic and pelagic realms [15]. In this framework the effort required in ecological modelling is to consider the BPC as a crucial component for the biogeochemical elements cycling closure.

The ambition of this thesis is to contribute to improve the representation of biogeochemical processes in coastal waters by quantifying (through proper parameterization) the fluxes related to the BPC.

Chapter 2

Introduction: The Benthic-Pelagic Coupling

2.1 Scientific Framework

The improvements in simulating the biogeochemical processes, occurring in the pelagic realm of the marine ecosystem, are now calling for the inclusion and a better definition of the interactions between the pelagic and benthic domain (the Benthic-Pelagic coupling, BPC), given the important role played by the sediment in the general ocean biogeochemical cycling [16] and given the perturbation of such cycling operated by the anthropogenic pressure on the coastal domain [17].

Here it is briefly described the structure of the BPC and the main fluxes of organic and inorganic matter between the two realms.

In figure 2.1 it is reported a scheme of the matter fluxes connecting the pelagic and the benthic domain along with the main benthic state variables operating the organic matter recycling.

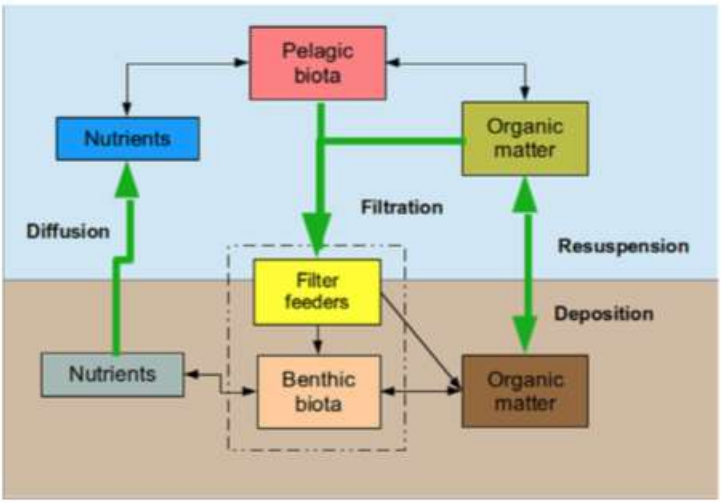

Figure 2.1: A scheme representing the main benthic–pelagic fluxes of matter along with indication of the state variables operating the organic matter cycling from [18].)

There is then an almost direct connection (modulated by depth [19]) between the trophic state of the pelagic system and the magnitude of the BPC processes [20, 21, 22, 23].

Once embedded into the sediments, the organic matter constitutes the main energy source for the benthic biota (bacteria and heterotrophic fauna), with the only, but very important exception of the 'filter feeders' functional group that feeds directly on the sinking organic matter prior to its embedding into sediments. Filter feeders are then an important element in structuring the BPC and the coastal marine ecosystem [24].

A fraction of the organic matter embedded into the sediment is directly taken up by bacteria, operating remineralization.

At the water bottom interface and below the euphotic zone, the BPC processes are essentially driven by the pelagic domain, as the main input of

organic matter into the sediment originates from the net deposition (organic matter sinking by gravity) and resuspension (benthic organic matter re-injection into the water column due to turbulent processes [14]).

Benthic fauna feeds on organic matter and contributes to organic matter biogeochemical cycling through excretion and respiration processes that contribute to the dissolved nutrients and carbon dioxide [25, 26, 27, 28], sediment enrichment and to benthic oxygen depletion.

The backward (sediment to water) BPC fluxes determine the return of the sediment recycled nutrient and carbon dioxide into the water column. This occurs essentially through diffusive processes at the water sediment interface.

The connection between the pelagic trophic state, depth and the BPC intensity, stated above, implies that shallow nutrients enriched areas, such as coastal regions directly influenced by a river discharge nutrients load are interested by intense BPC processes determined by an enhanced organic matte deposition at the water sediment interface [22, 23].

Finally, it has to be stressed that also the mixing/stratification characteristics and time variability affect BPC processes intensity as intense mixing (due to the winds) redistribute over the whole water column the inorganic nutrients remineralized by the benthic cycling and diffused back into the lower levels of the water column. Conversely stratified conditions partially isolate the water sediment interface from water column sections, thereby limiting nutrients input from the bottom.

The mid-latitude seasonal variability of the water column density structure then acts as a regulator of the trophic dynamics, modulating both the input and output processes governing the BPC [14, 25, 29, 30].

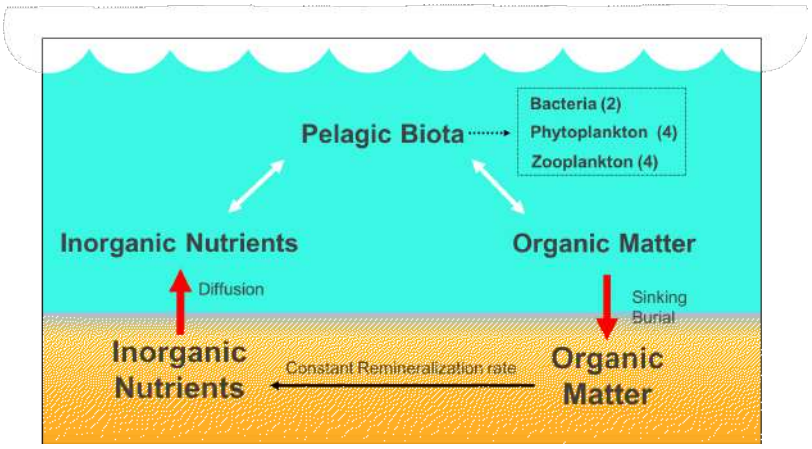

Figure 2.2: Scheme of the benthic closure adopted in biogeochemical models of the pelagic domain.

2.2 State of the art of BPC in numerical modelling

Despite the importance of the benthic domain for the coastal waters ecosystems and the continuous enhancement of models resolution, BPC in ecological models is in general approximated through a simple closure term for mass conservation [31, 14, 32], that is to say that the water column organic matter losses, due to the sedimentation of phytoplankton and organic detritus are in balance with the diffusive fluxes.

This means that, with respect to Figure 2.1 the structure of the BPC water sediment interactions is simplified as depicted in Figure 2.2.

It has easily noted that the organic matter cycling is no longer modulated by the dynamic of the benthic fauna, but is governed by a constant (in time and space) remineralization rate, parameterizing almost the whole benthic ecosystem functioning. Such simple definition of the BPC structure implies that the whole BPC dynamics is governed by three values: the rate at which the sinking organic matter is embedded into the sediments (hereafter defined

as 'burial velocity'), the diffusive rate at the water sediment interface and the constant remineralization rate.

There are few studies (based on rather poor datasets in terms of number of measurements and area of study) aimed to quantify the sediment–water exchange processes [33, 34, 35]. However a proper consideration of the benthic biogeochemical cycling must therefore be done at least at the level of parameterizations taking into consideration the mentioned parameters.

The parameterization of the temporal and spatial scales of BPC is a very challenging issue because observational data focusing on the BPC exchanges are scanty and sparse both in time and space; this thereby hampers model parameterization and validation. Given the scanty observational base, in light of what has been said so far, it can be deduced the improvements work in representing BPC processes neglecting to follow a "step by step" procedure in simulating the BPC. In this research, this procedure starts with the development of a parameterized simple BPC numerical model (using a one dimension coupled model configuration).

2.3 Aims of the thesis

The purposes of this thesis are: 1. To develop a simple model addressing BPC processes with the parameterized benthic organic matter cycling (in view of the use in global models) 2. To assess the skills of one-dimensional coupled physical-biogeochemical models in simulating the BPC by implementing the NEMO-BFM-1D model in marine areas with different physical and biogeochemical characteristics, seeking practical parameterizations able to describe different oceanic regimes.

The numerical tool used in this work is the one-dimensional version of

the BFM-NEMO coupled physical-biogeochemical model in order to evaluate the sensitivity of the pelagic biogeochemical dynamics to a simple BPC parameterization by implementing the numerical tool in different sites characterized by contrasting oceanographic characteristics and covered by rich observational datasets, so that a meaningful validation procedure could be carried out.

2.4 Structure of the thesis

The next Chapter (Chapter 3.1) gives an overview of the coupled NEMO-BFM model with particular reference to the BPC sub-model implementation. Chapter 4.1 motivates the choice of the model implementation sites and provides the description of the numerical experiments performed. Chapter 5.1, 6.1 and 7.1 provide a description of the main characteristics of each implementation site and of the simulation results. The conclusive Chapter 8.1 is devoted to an in depth assessment of the skill of the BPC sub-model in simulating different environmental characteristics in contrasting sites. This assessment is achieved through an extensive sensitivity analysis procedure. Chapter 9 summarizes the achieved results and presents the possible further developments.

Chapter 3

The NEMO-BFM model

3.1 Coupled physical–biogeochemical model

This work has been carried out using the one-dimensional (1D) version of the NEMO-BFM modelling system of the coupled physical-biogeochemical dynamics of the marine environment. The general characteristics of the modelling system are given here. However, for an in-depth description of the theoretical basis and the technical implementation of each model, the reader can refer for NEMO to Madec [36] and for BFM to Vichi et al. [37], while the coupling strategy between the two models is documented in Vichi et al. [38].

3.1.1 NEMO 1D

NEMO (Nucleus for European Modelling of the Ocean) 1D is a numerical tool that enables simulations of the physical vertical dynamics of the ocean [39]. Here, it is used to simulate the biogeochemical dynamics coupled with the vertical mixing processes and to perform sensitivity analysis with low

computational costs [39].

The 1D configuration is based on a 3 x 3 horizontal grid and the horizontal derivatives, around the central point, the T-point, are zero. The staggered C grid along the vertical direction adopted by the model is computed directly by the NEMO code on the basis of the bathymetry and the chosen number of vertical levels. As shown in Figure 3.1, the vertical grid levels are mostly concentrated close to the surface by means of a logarithmic distribution to provide a detailed representation close to the surface.

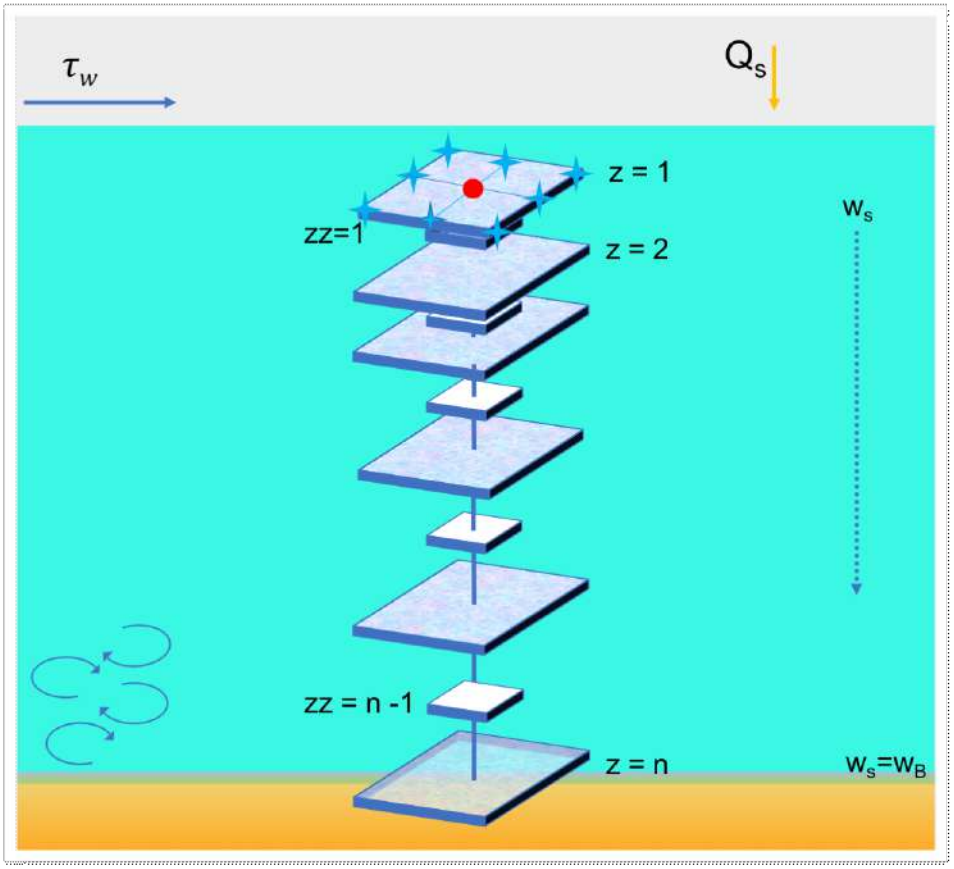

Figure 3.1: NEMO vertical staggered C grid scheme of the water column with the drivers of seasonality (τ_w is the wind stress, Q_s is the incoming solar radiation).

The primitive set of equations governing NEMO derives from:

- The Reynolds averaged Navier–Stokes equation:

$$\frac{\delta u_i}{\delta t} + u_j \frac{\delta(u_i)}{\delta x_j} = -\frac{1}{\rho_0}\frac{\delta P}{\delta x_i} - \frac{\delta}{\delta x_j}\left(\overline{u_j' u_i}' - \upsilon_{mol}\frac{\delta u_i}{\delta x_j}\right) + f_i \tag{3.1}$$

- The temperature transport equation:

$$\frac{\delta T}{\delta t} + u_j \frac{\delta(T)}{\delta x_j} = -\frac{\delta}{\delta x_j}\left(\overline{u_j' T'} - K_{mol}\frac{\delta T}{\delta x_j}\right) - \frac{1}{\rho_0 C_p} - \frac{\delta I(F_{sol}, z)}{\delta z} \tag{3.2}$$

- The salinity transport equation:

$$\frac{\delta S}{\delta t} + u_j \frac{\delta(S)}{\delta x_j} = -\frac{\delta}{\delta x_j}\left(\overline{u_j' S'} - K_{mol}\frac{\delta S}{\delta x_j}\right) + E_f - P_f \tag{3.3}$$

Reffray [39].

where $u_{i\{i=1,2,\}}$ is the horizontal component of the velocity field, T and S are the temperature and salinity respectively, $x_{j\{j=1,2,3\}} = (x, y, z)$ are the zonal, meridional and vertical directions, t is the time, $f_{i\{i=1,2\}}$ is the Coriolis term, P is the pressure, I is the downward irradiance, F_{sol} is the penetrative part of the surface heat flux, E_f and P_f are the evaporation and precipitation fluxes, and υ_{mol} and K_{mol} are the molecular viscosity and diffusivity terms.

The $\overline{u_j' u_i}'$ term refers to the Reynolds stresses while $\overline{u_j' T'}$ and $\overline{u_j' S'}$ refer to the turbulent scalar fluxes. Reynolds stresses can be expressed, after a scale analysis, as:

$$\overline{u_i' w'} = -\upsilon_t \frac{\delta u_i}{\delta z} \tag{3.4}$$

$$\overline{T' w'} = -K_t \frac{\delta T}{\delta z} \tag{3.5}$$

$$\overline{S'w'} = -K_t \frac{\delta S}{\delta z} \tag{3.6}$$

where υ_t and K_t are vertical turbulent viscosity and diffusivity terms respectively.

Combining Eqs. 3.1, 3.2, 3.3, respectively with Eqs. 3.4, 3.5 and 3.6, and considering that the horizontal derivatives in the one-dimensional case are zero, the general governing equations can be simplified to:

$$\frac{\delta u_i}{\delta t} = -\frac{\delta}{\delta z} - \upsilon_t \frac{\delta u_i}{\delta z} + f_i \tag{3.7}$$

$$\frac{\delta T}{\delta t} = -\frac{1}{\rho_0 C_p} - \frac{\delta I(F_{sol}, z)}{\delta z} - \frac{\delta}{\delta z} K_t \frac{\delta T}{\delta z} \tag{3.8}$$

$$\frac{\delta S}{\delta t} = -\frac{\delta}{\delta z} K_t \frac{\delta S}{\delta z} + E_f - P_f \tag{3.9}$$

Among the different vertical turbulent schemes available in NEMO, it was here selected the generic length scale (GLS) turbulent closure scheme that has the advantage to be easily applicable at different marine regions (see details in [39]). The GLS scheme is based on the turbulent kinetic energy ($\overline{k}$) equation and the transport equation for a generic statistical field variable (ψ) [40]. The rate of change of the turbulent kinetic energy deriving from the contraction of the transport equation of the Reynolds stress tensor, is:

$$\frac{\delta k}{\delta t} = D_k + P + G + \epsilon \tag{3.10}$$

where D_k summarizes the turbulent and viscous transport terms (Eq. 3.11), P is the production of turbulent kinetic energy by shear (Eq. 3.12), G relates to the production of turbulent kinetic energy by buoyancy (Eq. 3.13) and ϵ is the turbulent kinetic energy rate of dissipation (Eq. 3.14).

$$D_k = \frac{\delta}{\delta z}\frac{\delta \upsilon_t}{\delta \sigma_k}\frac{\delta k}{\delta z} \tag{3.11}$$

$$P = \upsilon_t M^2 \tag{3.12}$$

$$G = k_t N^2 \tag{3.13}$$

$$\epsilon = \left(C_\mu^0\right)^3 \frac{k^{3/2}}{l} \tag{3.14}$$

The term σ_t in equation 3.11 is the constant Schmidt–number and N^2 in equation 3.13 is the Brunt–Väisälä frequency. In equation 3.14, C_μ^0 represents the stability function of the vertical turbulent viscosity and diffusivity (constant in the model) and l is the mixing length.

The dissipation term (ϵ), the kinetic energy (k) and the mixing length (l) are expressed using a generic length scale, as described by Umlauf and Burchard [40]:

$$\Psi = \left(C_\mu^0\right)^p k^m l^n \tag{3.15}$$

where p, m, n are constants that allow to recover a number of well-known turbulent closures [36]. For Ψ the transport equation is:

$$\frac{\delta \psi}{\delta t} = D_\psi - \frac{\psi}{\delta k}\Big(C_{\psi 1}P + C_{\psi 3}G - C_{\psi 2^\epsilon}\Big) \tag{3.16}$$

where $C_{\psi 1}, C_{\psi 3}$ and $C_{\psi 2^\epsilon}$ are settled constant.

D_ψ represents the turbulent and viscous transport terms and it is defined as:

$$D_\psi = \frac{\delta}{\delta z}\frac{\delta \upsilon_t}{\delta \sigma_\psi}\frac{\delta \Psi}{\delta z} \tag{3.17}$$

In this work, the $\kappa - \epsilon$ scheme was adopted in all numerical experiments with the set of parameters listed in Table 3.1. This scheme enables for a

satisfactory representation of the spatial and temporal cycles of physical dynamics and, more specifically, the main features of stratification, mixed layer depth, and the position of both thermocline and halocline.

Scheme	(p, n, m)	σ_k	σ_ψ	C1	C2	C3
$\kappa - \epsilon$	(3 , 1.5 , -1)	1.	1.3	1.44	1.92	1.

Table 3.1: Parameters setting for $\kappa - \epsilon$ used with the GLS turbulence closure scheme [36]

A potential problem that may arise in the use of a one-dimensional configuration is the occurrence of drifts in temperature and salinity determined by either an imbalance in the surface water/heat fluxes or the missing contribution of lateral dynamic processes [25, 41]. This will lead to a limited capability of the 1D physical model to correctly represent the vertical water density structure. These problems can be tackled through the application of a restoring term towards observed values to ensure a more realistic simulation of ocean properties [42]. In NEMO, such a restoring procedure is done using a Newtonian damping term that can be applied to temperature, salinity and any oceanic tracers.

The equations describing the rectification of the model tracers computations are:

$$\frac{\delta T}{\delta t} = ...\gamma(T - T_0) \tag{3.18}$$

$$\frac{\delta S}{\delta t} = ...\gamma(S - S_0) \tag{3.19}$$

$$\frac{\delta N}{\delta t} = ...\gamma(N - N_0) \tag{3.20}$$

where γ is the restoring coefficient frequency (s^{-1}), T_0, S_0 and N_0 are the data towards which temperature, salinity and an oceanic tracer (e.g.

nitrate, phosphate) will be restored.

3.1.2 BFM

The Biogeochemical Flux Model, BFM, is a biomass and functional group based marine ecosystem model, representing the system in eulerian coordinates by a selection of chemical and biological processes that simulates the pelagic (water column) and the benthic (water sediment interface) dynamics in the marine ecosystems. The model also includes a sea ice component [43] not used in this thesis.

The formalism describing the BFM functional approach is explained in the reference paper of Vichi et al. [44], and it is based on the concepts of the Chemical Functional Families (CFF) and the Living Functional Groups (LFG). CFFs (Table 3.2) are divided into three main groups: non-living organic, living- organic and inorganic.

The LFG (listed in Table 3.2) notation is based on the concept of a standard organism that is frequently used in marine and terrestrial ecosystem modelling as a theoretical construct without any specific taxonomic value [45, 46, 47]. The biomass of the standard organism is constituted by living CFFs and interacts with living and non living CFFs by means of physiological and ecological processes (see Figure 3.2).

Variable	Type	Const	Units	Description
$N^{(1)}$	CFFs	P	mmol P m^{-3}	Phosphate
$N^{(3)}$	CFFs	N	mmol N m^{-3}	Nitrate
$N^{(4)}$	CFFs	N	mmol N m^{-3}	Ammonium
$N^{(5)}$	CFFs	Si	mmol Si m^{-3}	Silicate
$N^{(6)}$	CFFs	R	mmol S m^{-3}	Reduction equivalents
$N^{(7)}$	CFFs	Fe	μmol Fe m^{-3}	Dissolved iron
$O^{(2)}$	CFFs	O	mmol O_2 m^{-3}	Dissolved Oxygen
$O^{(3)}$	CFFs	C	mg C m^{-3}	Carbon Dioxide
$O^{(5)}$	CFFs	-	mmol Eq m^{-3}	Alkalinity
$P_i^{(1)}$	LFG	C N P Si Chl	mg C m^{-3}, mmol N-P m^{-3}, mg Chl-a m^{-3}	Diatoms
$P_i^{(2)}$	LFG	C N P Chl	mg C m^{-3}, mmol N-P m^{-3}, mg Chl-a m^{-3}	Flagellates
$P_i^{(3)}$	LFG	C N P Chl	mg C m^{-3}, mmol N-P m^{-3}, mg Chl-a m^{-3}	Picophytoplankton
$P_i^{(4)}$	LFG	C N P Chl	mg C m^{-3}, mmol N-P m^{-3}, mg Chl-a m^{-3}	Large Phytoplankton
B_i	LFG	C N P	mg C m^{-3}, mmol N-P m^{-3}	Pelagic Bacteria (Anaerobic-aerobic)
$Z_i^{(3)}$	LFG	C N P	mg C m^{-3}, mmol N-P m^{-3}	Carnivorous mesozooplankton
$Z_i^{(4)}$	LFG	C N P	mg C m^{-3}, mmol N-P m^{-3}	Omnivorous mesozooplankton
$Z_i^{(5)}$	LFG	C N P	mg C m^{-3}, mmol N-P m^{-3}	Microzooplankton
$Z_i^{(6)}$	LFG	C N P	mg C m^{-3}, mmol N-P m^{-3}	Heterotrophic Flagellates
$R_i^{(1)}$	CFFs	C	mg C m^{-3}	Labile dissolved organic matter
$R_i^{(2)}$	CFFs	C	mg C m^{-3}	Semi-labile dissolved organic carbon
$R_i^{(3)}$	CFFs	C	mg C m^{-3}	Semi-refractory dissolved organic carbon
$R_i^{(6)}$	CFFs	C N P Si Fe	mg C m^{-3}, mmol N-P-Si m^{-3}, μmol Fe m^{-3}	Particulate organic detritus

Table 3.2: List of the Chemical Functional Families (CFF) and Living Functional Groups (LFG) state variables for the pelagic model. The subscript i indicates the basic components (if any) of the variables.

Figure 3.2 summarizes the complexity of the pelagic state variables and the main biological, physiological and ecological processes accounted by the BFM model in its standard configuration, while a complete list of the standard biogeochemical parameterization can be found in Appendix A.1.

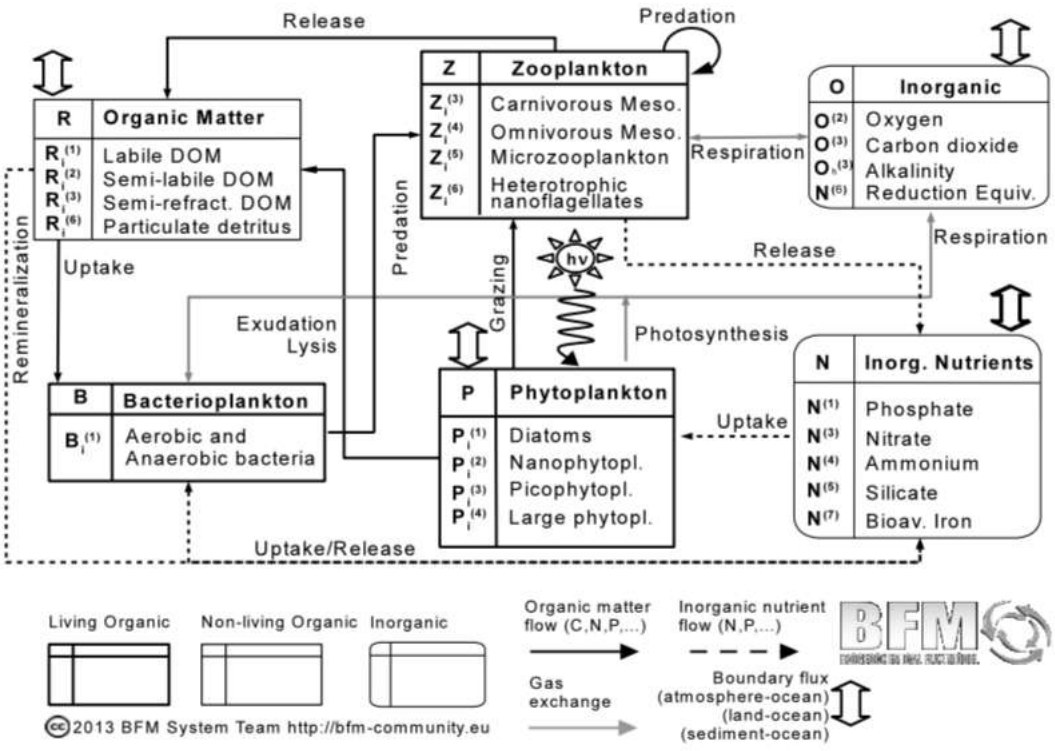

Figure 3.2: Scheme of the state variables and pelagic interactions of the BFM model. Living (organic) Chemical Functional Families (CFF) are indicated with bold-line square boxes, non-living organic CFFs with thin-line square boxes and inorganic CFFs with rounded boxes (modified after Blackford and Radford (1995)[48]). Fig. from BFM manual [44].

All the physiological processes simulated in the BFM show dependence on temperature. The temperature effect is parametrized in the following non-dimensional form:

$$f^T = Q_{10}^{\frac{T-10}{10}} \tag{3.21}$$

where the Q_{10} parameter is LFG -specific (see Appendix A.1).

The portion of solar radiation used by the primary producers to fix carbon is the Photosynthetic Available Radiation (PAR). PAR is strictly dependent on the optical properties of the sea waters and it is strongly influenced by sea water turbidity expressed in terms of dissolved matter, suspended matter and chlorophyll concentration. The parameterization of PAR comes from the Lambert-Beer formulation with the broadband, depth-dependent extinction coefficients:

$$E_{PAR}(z) = \epsilon_{PAR} Q_s e^{\lambda_w z + \int_z^0 \lambda_{bio}(z')dz'} \tag{3.22}$$

where Q_s is the short-wave surface irradiance flux, ϵ_{PAR} is the fraction of PAR in Q_s. λ_w is the background extinction coefficient of the water, λ_{bio} is the biological extinction term due to the phytoplankton (P_l^j) and detritus (R_c^6).

The numerical description of each LFG is formulated using the same primitive equations but different physiological and ecological parameters (see Appendix A.1)). Figure 3.2 and Table 3.3 summarize the physiological processes and the ecological interactions considered in the BFM pelagic model.

The biological reactions terms, for the phytoplankton, the zooplankton and bacteria are generically indicated as:

$$\frac{dP}{dt} = Uptake - Exudation - Respiration - Grazing \tag{3.23}$$

$$\frac{dZ}{dt} = Ingestion - Egestion - Respiration - Predation \tag{3.24}$$

$$\frac{dB}{dt} = Uptake - Remineralization - Respiration - Predation \tag{3.25}$$

The complete formulation of the living state variables governing equations is listed in Table 3.4-3.6, while the abbreviations used for the description of the processes are listed in Table 3.3:

Abbreviation	**Process**
gpp	Gross Primary Production
rsp	Respiration
prd	Predation
rel	Release
exu	Exudation
lys	Lysis
syn	Biochemical Synthesis
nit/denit	Nitrification/Denitrification
scv	Scavenging
rmn	Biochemical remineralization
sed	Sedimentation
bur	Burial

Table 3.3: List of all abbreviations for the physiological and ecological processes described in the BFM equations

P_c: $$\left.\frac{dP_c}{dt}\right|_{bio} = \left.\frac{dP_c}{dt}\right|^{gpp}_{O^{(3)}} - \left.\frac{dP_c}{dt}\right|^{exu}_{R_c^{(1)}} - \left.\frac{dP_c}{dt}\right|^{rsp}_{O^{(3)}} - \sum_{j=1,6} \left.\frac{dP_c}{dt}\right|^{lys}_{R_c^{(j)}} - \sum_{k=3}^{6} \left.\frac{dP_c}{dt}\right|^{prd}_{Z_c^{(k)}} \tag{3.26}$$

P_n $$\left.\frac{dP_n}{dt}\right|_{bio} = \sum_{j=3,4} \left.\frac{dP_n}{dt}\right|^{upt}_{N^{(i)}} - \sum_{j=1,6} \left.\frac{dP_n}{dt}\right|^{lys}_{R_n^{(j)}} - \frac{P_n}{P_c} \sum_{k=3}^{6} \left.\frac{dP_c}{dt}\right|^{prd}_{Z_c^{(k)}} \tag{3.27}$$

P_p: $$\left.\frac{dP_p}{dt}\right|_{bio} = \left.\frac{dP_p}{dt}\right|^{upt}_{N^{(1)}} - \left.\frac{dP_p}{dt}\right|^{lys}_{R_p^{(i)}} - \frac{P_p}{P_c} \sum_{k=3}^{6} \left.\frac{dP_c}{dt}\right|^{prd}_{Z_c^{(k)}} \tag{3.28}$$

P_s: $$\left.\frac{dP_s}{dt}\right|_{bio} = \left.\frac{dP_s}{dt}\right|^{upt}_{N^{(5)}} - \sum_{j=1,6} \left.\frac{dP_s}{dt}\right|^{lys}_{R_s^{(6)}} - \frac{P_s}{P_c} \sum_{k=3}^{6} \left.\frac{dP_c}{dt}\right|^{prd}_{Z_c^{(k)}} \quad if P_s = P_s^{(1)} \quad \frac{dP_s}{dt} \neq 0 \tag{3.29}$$

P_l: $$\left.\frac{dP_l}{dt}\right|_{bio} = \left.\frac{dP_l}{dt}\right|^{syn} - \frac{P_l}{P_c} \sum_{j} \left.\frac{dP_c}{dt}\right|^{prd}_{Z_c^{(j)}} \tag{3.30}$$

P_f: $$\left.\frac{dP_f}{dt}\right|_{bio} = \left.\frac{dP_f}{dt}\right|^{upt}_{N^{(7)}} - \left.\frac{dP_f}{dt}\right|^{lys}_{R_f^{(6)}} - \frac{P_f}{P_c} \sum_{k=3}^{6} \left.\frac{dP_c}{dt}\right|^{prd}_{Z_c^{(k)}} \tag{3.31}$$

Table 3.4: Governing equations of phytoplankton Functional Family. For the processes notation see Table 3.3

$$\mathrm{Z}_c: \quad \left.\frac{dZ_c}{dt}\right|_{bio} = \sum_{X=P,Z} \left.\frac{dZ_c}{dt}\right|_{X_c}^{prd} - \sum_{j=1,6} \left.\frac{dZ_c}{dt}\right|_{R_c^{(j)}}^{rel} - \left.\frac{dZ_c}{dt}\right|_{O^{(3)}}^{rsp} - \sum_{k=3}^{6} \left.\frac{dZ_c}{dt}\right|_{Z_c^{(k)}}^{prd} \tag{3.32}$$

$$\mathrm{Z}_n: \quad \left.\frac{dZ_n}{dt}\right|_{bio} = \frac{F_n}{F_c} \sum_{X=P,Z} \left.\frac{dZ_c}{dt}\right|_{X_c}^{prd} - \sum_{j=1,6} \left.\frac{dZ_n}{dt}\right|_{R_n^{(j)}}^{rel} - \left.\frac{dZ_n}{dt}\right|_{N^{(4)}}^{rel} - \frac{Z_n}{Z_c} \sum_{k=3}^{6} \left.\frac{dZ_c}{dt}\right|_{Z_c^{(k)}}^{prd} \tag{3.33}$$

$$\mathrm{Z}_p: \quad \left.\frac{dZ_p}{dt}\right|_{bio} = \frac{F_p}{F_c} \sum_{X=P,Z} \left.\frac{dZ_c}{dt}\right|_{X_c}^{prd} - \sum_{j=1,6} \left.\frac{dZ_p}{dt}\right|_{R_p^{(j)}}^{rel} - \left.\frac{dZ_p}{dt}\right|_{N^{(1)}}^{rel} - \frac{Z_p}{Z_c} \sum_{k=3}^{6} \left.\frac{dZ_c}{dt}\right|_{Z_c^{(k)}}^{prd} \tag{3.34}$$

Table 3.5: Governing equations of zooplankton Functional Family. For the processes notation see Table 3.3

$$B1_c: \quad \left.\frac{dB_c}{dt}\right|_{bio} = \sum_{j=1,6} \left.\frac{dB_c}{dt}\right|_{R_c^{(j)}}^{upt} - \left.\frac{dB_c}{dt}\right|_{O^{(3)}}^{rsp} - \sum_{k=3}^{6} \left.\frac{dB_c}{dt}\right|_{Z_c^{(k)}}^{prd} \tag{3.35}$$

$$B1_n: \quad \left.\frac{dB_n}{dt}\right|_{bio} = \sum_{j=1,6} \frac{R_n(j)}{R_c(j)} \left.\frac{dB_c}{dt}\right|_{R_c^{(j)}}^{upt} + f_B^n \left.\frac{dB_n}{dt}\right|_{N(4)}^{upt,rel} - \frac{B_n}{B_c} \sum_{k=3}^{6} \left.\frac{dB_c}{dt}\right|_{Z_c^{(k)}}^{prd} \tag{3.36}$$

$$B1_p: \quad \left.\frac{dB_p}{dt}\right|_{bio} = \sum_{j=1,6} \frac{R_p(j)}{R_c(j)} \left.\frac{dB_c}{dt}\right|_{R_c^{(j)}}^{upt} + f_B^p \left.\frac{dB_p}{dt}\right|_{N(1)}^{upt,rel} - \frac{B_p}{B_c} \sum_{k=3}^{6} \left.\frac{dB_c}{dt}\right|_{Z_c^{(k)}}^{prd} \tag{3.37}$$

Table 3.6: Governing equations of bacteria Functional Family. For the processes notation see see Table 3.3

The pelagic cycle of inorganic nutrients affects and is affected by phytoplankton and bacteria activities of uptake and release and by zooplankton excretion. Phytoplankton and bacteria production can be limited by inorganic nutrients concentration. In BFM, nutrients limitation is treated following Baretta-Bekker et al. [45] i.e. in which nutrients limiting factors are partitioned in internal or external, based on an internal nutrient quota or the external dissolved inorganic concentrations. BFM accounts for the limiting nutrient using the following co–limitation approach:

$$f_p^{nut} = min(f_p^{n,p}, f_p^f, f_p^s)$$

The equations governing the dynamics of the pelagic inorganic nutrients are listed in Table 3.7:

N1p:
$$\left.\frac{dN^{(1)}}{dt}\right|_{bio} = -\sum_{j=1}^{4} \left.\frac{dP_p^{(j)}}{dt}\right|_{N^{(1)}}^{upt} + f_B^p \left.\frac{dB_p^{(j)}}{dt}\right|_{N^{(1)}}^{upt,rel} + \sum_{j=3}^{6} \left.\frac{dZ_p^{(k)}}{dt}\right|_{N^{(1)}}^{rsp} \tag{3.38}$$

N3n
$$\left.\frac{dN^{(3)}}{dt}\right|_{bio} = -\sum_{j=1}^{4} \left.\frac{dP_n^{(j)}}{dt}\right|_{N^{(3)}}^{upt} + \left.\frac{dN^{(3)}}{dt}\right|_{N^{(4)}}^{nit} - \left.\frac{dN^{(3)}}{dt}\right|_{sink_n}^{denit} \tag{3.39}$$

N4n:
$$\left.\frac{dN^{(4)}}{dt}\right|_{bio} = -\sum_{j=1}^{4} \left.\frac{dP_n^{(j)}}{dt}\right|_{N^{(4)}}^{upt} + f_B^p \left.\frac{dB_n^{(j)}}{dt}\right|_{N^{(4)}}^{upt,rel} + \sum_{j=3}^{6} \left.\frac{dZ_n^{(k)}}{dt}\right|_{N^{(4)}}^{rsp} - \left.\frac{dN^{(4)}}{dt}\right|_{N^{(3)}}^{nit} \tag{3.40}$$

N5s:
$$\left.\frac{dN^{(5)}}{dt}\right|_{bio} = -\left.\frac{dP_s^{(1)}}{dt}\right|_{N^{(5)}}^{upt} + \left.\frac{dR_s^{(6)}}{dt}\right|_{N^{(5)}}^{rmn} \tag{3.41}$$

N5f:
$$\left.\frac{dN^{(7)}}{dt}\right|_{bio} = -\left.\frac{dP_f}{dt}\right|_{N^{(7)}}^{upt} + \left.\frac{dR_f^{(6)}}{dt}\right|_{N^{(7)}}^{rmn} + \left.\frac{dN^{(7)}}{dt}\right|_{sink_n}^{scv} \tag{3.42}$$

Table 3.7: Governing equations of nutrients. For the processes notation see Table 3.3

Dissolved organic matter (DOM) dynamics is strongly linked with the biota activity. DOM is produced by phytoplankton, microzooplankton and bacteria. In the BFM configuration used in this work, DOM has all the different degrees of lability/refractivity provided by the model (see Table 3.2), which differ from each others for the turn-over time scale. Only bacteria are able to degrade the different types of DOM.

Pelagic particulate organic matter (POM) is produced by all the members of the plankton community except bacteria which use this matter as substrate. The biogenic silica production depends exclusively on the release of frustules by diatoms while losses are linked to the micro/mesozooplankton predation. Once produced, particulate organic matter (POM) can be degraded by bacteria and deposited in the sediment-water interface with a proper sinking velocity. The governing equations for DOM and POM are listed in Table 3.8.

$$R_c^{(1)}: \qquad \left.\frac{dR_c^{(1)}}{dt}\right|_{bio} = \sum_{j=1}^{4} \left.\frac{dP_c^{(j)}}{dt}\right|_{R_c^{(1)}}^{exu} - \left.\frac{dB_c}{dt}\right|_{R_c^{(1)}}^{upt} + \sum_{j=3}^{6} \left.\frac{dZ_c^{(k)}}{dt}\right|_{R_c^{(1)}}^{rel} \tag{3.43}$$

$$R_i^{(1)} \qquad \left.\frac{dR_i^{(1)}}{dt}\right|_{bio} = \sum_{j=1}^{4} \left.\frac{dP_c^{(j)}}{dt}\right|_{R_c^{(1)}}^{exu} - \frac{R_i^{(i)}}{R_c^{(1)}} \left.\frac{dB_c}{dt}\right|_{R_c^{(1)}}^{upt} + \sum_{j=3}^{6} \frac{Z_i^{(k)}}{Z_c^{(c)}} \left.\frac{dZ_c^{(k)}}{dt}\right|_{R_c^{(1)}}^{rel} \quad i = n, p \tag{3.44}$$

$$R_i^{(2)} \qquad \left.\frac{dR_c^{(2)}}{dt}\right|_{bio} = \left.\frac{dP_c^{(j)}}{dt}\right|_{R_c^{(2)}}^{exu} - \left.\frac{dB_c}{dt}\right|_{R_c^{(2)}}^{upt} + \left.\frac{dB_c}{dt}\right|_{R_c^{(2)}}^{rel} \tag{3.45}$$

$$R_i^{(6)} \qquad \left.\frac{dR_c^{(6)}}{dt}\right|_{bio} = \sum_{j=1}^{4} \left.\frac{dP_c^{(j)}}{dt}\right|_{R_c^{(6)}}^{lys} - \left.\frac{dB_c}{dt}\right|_{R_c^{(6)}}^{upt} + \sum_{j=3}^{6} \left.\frac{dZ_c^{(k)}}{dt}\right|_{R_c^{(6)}}^{rel} \tag{3.46}$$

$$R_i^{(6)} \qquad \left.\frac{dR_i^{(6)}}{dt}\right|_{bio} = \sum_{j=1}^{4} \left.\frac{dP_i^{(j)}}{dt}\right|_{R_c^{(6)}}^{lys} - \frac{R_i^{(6)}}{R_c^{(6)}} \left.\frac{dB_c}{dt}\right|_{R_c^{(6)}}^{upt} + \sum_{j=3}^{6} \frac{Z_i^{(k)}}{Z_c^{(c)}} \left.\frac{dZ_c^{(k)}}{dt}\right|_{R_c^{(6)}}^{rel} \quad i = n, p \tag{3.47}$$

$$R_s^{(6)} \qquad \left.\frac{dR_s^{(6)}}{dt}\right|_{bio} = \left.\frac{dP_s^{(1)}}{dt}\right|_{R_s^{(6)}}^{lys} + \frac{P_s^{(1)}}{P_c^{(1)}} \sum_{j=3}^{6} \left.\frac{dP_c^{(1)}}{dt}\right|_{Z_c^{(j)}}^{prd} - \left.\frac{dR_s^{(6)}}{dt}\right|_{N_s^{(5)}}^{rmn} \tag{3.48}$$

Table 3.8: Governing equations of dissolved and particulate organic matter. For the processes notation see Table 3.3

3.2 The Benthic Submodel

3.2.1 Background

Marine biogeochemical cycles incorporate both the pelagic and benthic habitats and thus integrate processes and interactions in both environments. Here, the focus is on how low trophic levels processes such as cycling of nitrogen (N), phosphorus (P), carbon (C), silicon (Si), carbon dioxide (CO2), oxygen (O2), primary production, bacteria production, animal nutrient excretion, and decomposition, link benthic and pelagic habitats.

The general scheme of BPC used in this thesis is the same described in [49]. The particulate pelagic organic matter produced via lysis, excretion and egestion, not consumed or remineralized in the water column sinks to the seafloor with a specific sedimentation velocity. Once it reaches the seawater-sediment interface, the pelagic organic matter is buried into the sediments and, with a certain rates, remineralized by bacteria. It is estimated [50], that a quarter of all organic material that exits the photic zone reaches the seafloor without being remineralized and 90% of that remaining material is remineralized in sediments, consuming oxygen and producing carbon dioxide. The benthic nutrient pool is further enriched by the products of the benthic fauna excretion.

In the sediments, the remineralized inorganic nutrients diffuses into the lower levels of the water column, and vertical dynamics injects them into the photic zone. This source of nutrients feeds the lower trophic levels activity, (bacteria and phytoplankton) that, in turns, stimulates the zooplankton growth [51, 52] (see Figure 2.2).

3.2.2 Benthic and Pelagic Coupling submodel structure

As previously mentioned and as depicted in Figure 2.2 the benthic-pelagic submodel structure, implemented in the 1D modelling system, is considerably simplified with respect to the model structure fully resolving the benthic biology. In fact the benthic compartment is defined by only the following state variables:

- the labile organic matter in the sediments surface ($Q_j^{(1)}$ with j= carbon, nitrate, ammonium and phosphate)
- the particulate organic matter in the sediments surface ($Q_j^{(6)}$ with j= carbon, nitrate, ammonium, phosphate and silicate).

These C,P,N,Si pools are enriched by the phytoplankton diatoms and large phytoplankton ($P^{(1)}$ and $P^{(4)}$ respectively) and organic detritus ($R^{(6)}$). Sinking phytoplankton and organic detritus are buried into the sediments at a specific constant rate (the 'burial velocity' ω_{bur}, expressed in m/d).

Adopting the formalism of Vichi et al. [37], the temporal rate of change of the benthic organic matter (Q) is:

$$\left.\frac{dQ_j^{(1)}}{dt}\right|^{sed}_{P_j^{(1,4)},R_j^{(1)}} = -\omega_{bur}\left[R_j^{(1)} + \xi_j \sum_{i=1,4} P_{(j)}\right]_{z=z_b} \tag{3.49}$$

$$\left.\frac{dQ_j^{(6)}}{dt}\right|^{sed}_{P_j^{(1,4)},R_j^{(6)}} = -\omega_{bur}\left[R_j^{(6)} + (1-\xi_j) \sum_{i=1,4} P_{(j)}\right]_{z=z_b} \tag{3.50}$$

$$\left.\frac{dQ_s^{(6)}}{dt}\right|^{sed}_{P_j^{(1)}R_s^{(6)}} = -\omega_{bur}\left[R_s^{(6)} + P_{(s)}\right]_{z=z_b} \tag{3.51}$$

where z_b is the depth of the bottom-most gridpoint. The settling phytoplankton is partitioned in particulate and dissolved matter, according to

the ξ_j partitioning coefficient. Comparing Figure 2.1 with 2.2 it is apparent that the ω_{bur} parameter resolves also the particulate organic matter sediment embedding due not only to sinking but also to the benthic filters feeders activity.

The remineralization flux (inorganic matter flowing from the sediment to the water) is parametrized by assuming that a constant portion of organic matter in the organic sediments is remineralized and released in the pelagic compartment as follows:

$$\left.\frac{dQ_j^{(1)}}{dt}\right|^{rmn/diff} = \mu_{Q_j^{(1)}}\ Q_j^{(1)}\Big|_{z=zb} \tag{3.52}$$

$$\left.\frac{dQ_j^{(6)}}{dt}\right|^{rmn/diff} = \mu_{Q_j^{(6)}}\ Q_j^{(6)}\Big|_{z=zb} \tag{3.53}$$

$$\left.\frac{dQ_s^{(6)}}{dt}\right|^{rmn/diff} = \mu_{Q_s^{(6)}}\ Q_s^{(6)}\Big|_{z=zb} \tag{3.54}$$

where $\mu(1,6)$ are the recycling time scales operating the conversion of the benthic organic matter into pelagic dissolved nutrients.

The oxygen consumption, associated to remineralization process, is stoichiometrically associated to the carbon remineralization rates. Nitrogen remineralization is partitioned into ammonium and nitrate fluxes with a constant ratio.

Lastly, the general equation describing the rate of change of organic matter in the sediments is defined by:

$$\frac{dQ_j^{(1,6)}}{dt} = -\left.\frac{dQ_j^{(1,6)}}{dt}\right|^{rmn} + \left.\frac{dQ_j^{(1,6)}}{dt}\right|^{sed} \tag{3.55}$$

3.2.3 Boundary conditions

Forcing an Ocean General Circulation Model (OGCM) amounts to specifying surface and bottom boundary conditions for the vertical dynamics of a model's prognostic equations for potential temperature, salinity, and the momentum components [42].

Surface boundary conditions

In NEMO-1D the surface boundary conditions are applied at the surface-most grid point $z = 0$. The physical model requires the following fields as surface boundary conditions with a frequency at which the forcing fields have to be updated:

- the zonal and meridional components of the wind stress (τ_x, τ_y, respectively).
- the surface heat flux partitioned in longwave radiation (Qns) and shortwave radiation (Qsr). The former is the non penetrative part of the radiation flux.
- the surface freshwater flux (evaporation - precipitation- runoff)
- the surface salt flux associated with freezing/melting of seawater (sfx)

For the BFM the surface boundary conditions are:

$$\left.\frac{dC_i}{dz}\right|_{z=0} = 0 \tag{3.56a}$$

$$\left.\frac{dC_i}{dz}\right|_{z=0} = F_j \tag{3.56b}$$

$$\left.\frac{dC_i}{dz}\right|_{z=0} = \gamma(C_j - C_{jref}) \tag{3.56c}$$

where Equation 3.56a is valid for all the living organic and non living organic state variables type, while Equation 3.56b is valid for those state variables interacting at the air-sea or land-sea interface. Finally, Equation 3.56c expresses the surface boundary condition obtained by relaxing (Section 3.1.1) a surface state variable value (e.g. for the inorganic nutrients) to a prescribed time-varying value.

Bottom boundary conditions

At the water-sediment interface, the bottom boundary conditions are applied at the bottom-most vertical level (z=z_b).

In NEMO the momentum, the tracers, the heat and the velocity derivatives are set to zero.

The BFM benthic submodel provides the bottom boundary conditions for the pelagic nutrients computation as follows:

$$\frac{dC_i}{dz} = 0 \tag{3.57a}$$

$$\frac{dC_i}{dz} = \left.\frac{dC_i}{\delta t}\right|^{rmn/diff} \tag{3.57b}$$

$$w = w_b \tag{3.57c}$$

where Equation 3.57a is valid for all the Living Organic and Non Living Organic state variables and Equation 3.57b is valid for the inorganic nutrients considered in the BPC.

3.2.4 BFM-NEMO Coupling scheme

In describing the NEMO-BFM coupled configuration scheme, we use to the same conceptual formalism used to express the equations of biogeochemical dynamics.

The conservation equation for an infinitesimal volume of fluid, containing a certain concentration of a passively transported tracer C, is obtained applying the continuum hypothesis:

$$\frac{\delta C}{\delta t} = -\vec{\nabla} \cdot \vec{F} \tag{3.58}$$

where $\vec{F}$ is the generalized flux of C.

Equation 3.58 can be rewritten expressing separately the physical (handled by the NEMO 1D) and the biogeochemical (handled by BFM) contributions:

$$\frac{\delta C}{\delta t} = -\vec{\nabla} \cdot \vec{F}_{phys} - \vec{\nabla} \cdot \vec{F}_{bio} \tag{3.59}$$

The biological reaction term, is approximated as:

$$\vec{\nabla} \cdot \vec{F}_{bio} = -w_B \frac{\delta C}{\delta z} + \left.\frac{\delta C}{\delta t}\right|_{bio} \tag{3.60}$$

where w_B refers to the sinking vertical velocity for those variables having a mass related vertical velocity other than the fluid velocity (e.g. the detritus).

From equations 3.59 and 3.60 is derived the advection-diffusion-reaction equation for an incompressible fluid:

$$\frac{\delta C}{\delta t} = -\mathbf{u} \cdot \nabla C + \nabla_H \cdot (A_H \nabla_H C) + \frac{\delta}{\delta z} A_V \frac{\delta C}{\delta z} - w_B \frac{\delta C}{\delta z} + \left.\frac{\delta C}{\delta t}\right|_{bio} \tag{3.61}$$

where $\mathbf{u} \equiv (u, v, w)$ is the three-dimensional velocity, A_H, A_V horizontal and vertical turbulent diffusivity coefficient for tracers.

Equation 3.61 can be rewritten indicating the ocean variables solved by the ocean general circulation model and needed for the biological reaction term R computation:

$$\frac{\delta C}{\delta t}+u\frac{\delta C}{\delta x}+v\frac{\delta C}{\delta y}+w\frac{\delta C}{\delta z} = \nabla_H\cdot(A_H\nabla_H C)+\frac{\delta}{\delta z}A_V\frac{\delta C}{\delta z}-w_B\frac{\delta C}{\delta z}+R(T,S,W,E) \tag{3.62}$$

where T is the temperature, S is salinity, W is the intensity of the wind, and E is the shortwave radiation.

In the 1D configuration the horizontal derivatives are not considered and equation 3.62 became:

$$\frac{\delta C}{\delta t} = -w\frac{\delta C}{\delta z} + \frac{\delta}{\delta z}A_V\frac{\delta C}{\delta z} - w_B\frac{\delta C}{\delta z} + R(T,S,W,E) \tag{3.63}$$

The NEMO-BFM coupling equation 3.61 requires knowledge of some ocean physical dynamics, solved by the OGCM and transferred to the BFM. The conceptual framework of the coupling functioning is schematized in Figure 3.3. The OGCM model compute and transfer environmental information to the BFM which, in turn, compute the biological rates using the environmental information passed by the OGCM.

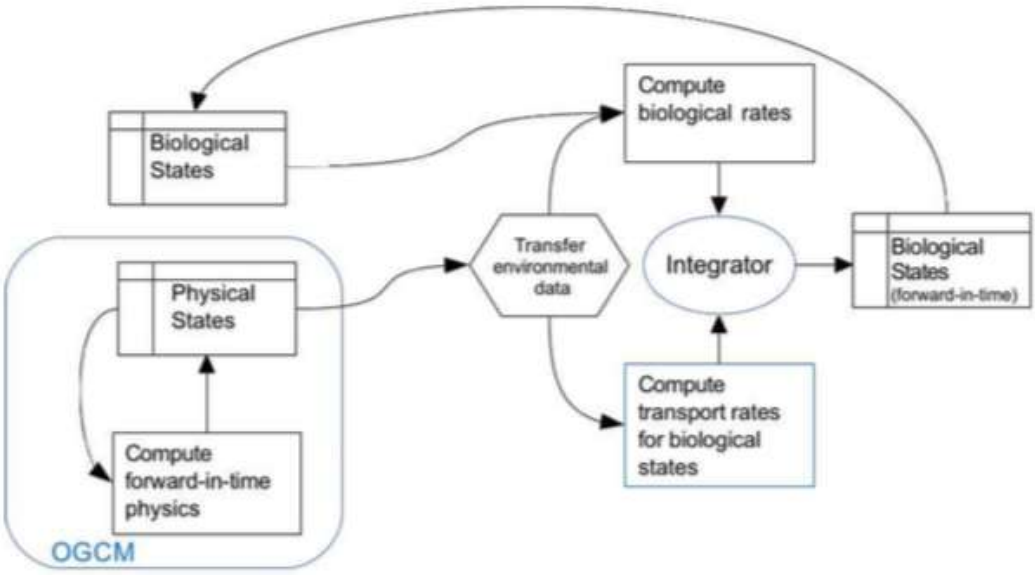

Figure 3.3: Scheme of the information flow between the ocean physical model and the biogeochemical state variables. The blue boxes indicate that the computation is carried out directly by the OGCM or using modified routines belonging to the OGCM. Integrator is a generic name for the solver used to advance in time the solution of the coupled physical-biogeochemical system. Scheme from Vichi et al. [38]

Chapter 4

Implementation sites and experiments design

4.1 The choice of the implementation sites

In order to achieve the objectives of this work, the 1D NEMO-BFM BPC sub-model has been implemented in three different sites. The choice of the implementation sites has been constrained by two factors: the coastal character with contrasting environmental features and the availability of the in-situ observations, which are necessary to assess the model skill with respect to the BPC dynamics.

Three different locations were selected to investigate the BPC processes using the coupled model (Figure XX):

1. Gulf of Trieste, MA21 area (North Adriatic Sea, Italy),
2. St. Helena Bay Monitoring Line, SHB (Atlantic Ocean, South Africa),
3. Svinøy Fyr, SFyr (Norwegian Sea, Norway).

The numerical experiments performed in the MA21 area in the Gulf of Trieste served as initial test benchmark, because of the large scientific literature dealing with observational and numerical modelling studies [53, 54, 55, 56, 57, 41, 23]. This gave an adequate observational basis to be compared with the output of the coupled model.

As second site, the station number 3 of the BENEFIT (Benguela Environment and Fisheries Interactions and Training) monitoring program in St. Helena Bay has been chosen to simulate the dynamics of an ecosystem embedded in a complex upwelling area [58, 59].

The third case study corresponds to the first station of the Svinøy Fyr Section in the Norwegian Sea. The dataset was compiled using the data publicly distributed by the Institute of Marine Research - Norwegian Marine Data Centre (INR-NMD) (https://www.nmdc.no and http://www.imr.no). It is the deepest site implemented in this work and it has been chosen to asses the skill of the model in reproducing the biogeochemical cycles in a cold water system and the deep BPC dynamics.

A description of the hydrographical and ecological characteristics of each site is given in the following dedicated chapters.

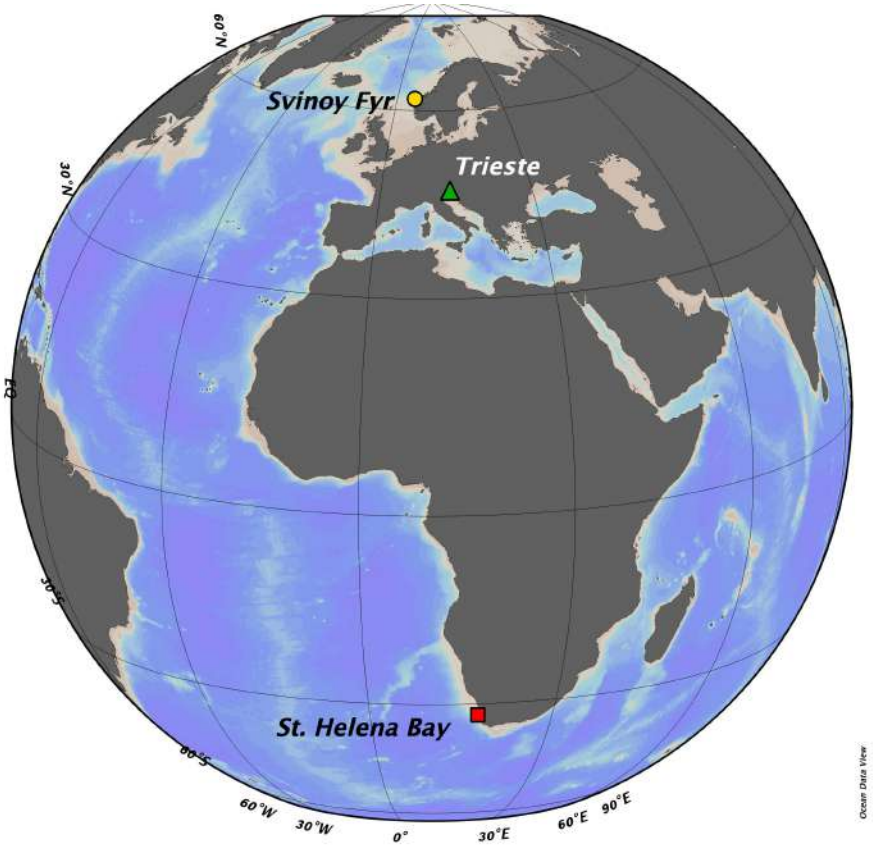

Figure 4.1: Map of the implemented sites.

4.2 Numerical experiments and model setup

At each site, a reference numerical experiment was performed by accounting for the coupled pelagic physical and biogeochemical processes with the integration of the benthic remineralization and diffusion processes of the BPC sub-model, which is hereinafter named **BPC-RETURN**.

A companion experiment was carried out by neglecting the benthic processing of organic matter that reaches the bottom sediments, here referred

to as **NO-RM**.

The comparison of the results produced by this twin set of experiments enables for the immediate evaluation of the benthic activity, e.g. oxygen consumption, nutrients regeneration toward the pelagic environment, in order to strength the relevance of including the BPC within the coupled NEMO-BFM model.

The numerical experiments performed at the three contrasting study sites share a common physical and biogeochemical setup, although specific choices were made to deal with the representation of local environmental conditions (detailed in the dedicated chapters). The shared set of parameters was derived from the NEMO-BFM global model configuration (see Appendix Table A.1, A.2, A.3 and A.4), while site-specific changes were done accounting also for previous literature findings [41, 54, 60].

The overall description of the common model features, atmospheric forcings, and available biogeochemical observational data for each site is provided in Table 4.1.

The use of a 1D water-column model may lead to potential drifts in simulated temperature and/or salinity profiles due to "non zero" surface heat and/or mass surface fluxes or to missing lateral advective fluxes that are by necessity not contained in the one-dimensional implementation [61, 41]. Thus, the simulated vertical profiles of temperature and salinity were constrained toward the climatological time dependent (monthly varying) profiles obtained from data using the restoring method described in Section 3.1.1. At all sites the relaxation time scale toward observation derived climatological fields was set to 5 days.

The atmospheric forcing used to drive the NEMO-BFM model were selected to deal with specific requirements for a site implementation or the

availability of alternative datasets with increasing spatiotemporal resolution.

Being the test benchmark, MA21 site has been forced in accordance to previous works [41, 18] using the ERA-Interim reanalysis dataset produced by the European Center for Medium-Range Weather Forecasts [62], with a nominal resolution of ∼80 km. The SHB station was forced with the higher resolution dataset (∼3km) obtained from the WRF-ROMS atmospheric-ocean coupled model simulations provided by the Climate Systems Analysis Group (CSAG) at University of Cape Town by G.Fearon. In the case of SFyr site, the fifth generation of ECMWF atmospheric reanalysis for the global climate, named ERA5, was preferred to the ERA-Interim reanalysis because of the higher spatial resolution (∼30 km) [63].

In all experiments, the atmospheric forcing was applied using the NEMO module of CORE bulk formulae [36] that requires the following input fields: zonal and meridional wind speed components, air temperature at 2 meters, specific humidity, snowfall and precipitation, and both downwards solar and thermal radiation.

The difference in the temporal extension of the experiments performed for MA21, with respect to SHB and SFyr, was determined by the need to compare the outcomes of this work also with the results obtained in previous scientific works ([41, 18]).

As data availability represented a primary constrain in the choice of the study sites, a significant effort was devoted at the beginning of this work to determine an appropriate set of criteria for the data selection to ensure the space-time coherence and continuity of measurements.

Temperature and salinity (T,S) data resulted in general easily available and abundant. On the contrary, biogeochemical data availability was largely

lower and this strongly limited the selection of suitable case study areas. In fact, the majority of the biogeochemical datasets have incomplete time series, as in many cases researches are focused on reproducing specific events or seasons.

The selection of biogeochemical data was done by choosing in situ measurements with metadata containing information about the quality control and the sampling techniques. In those cases where the time series were not available or were incomplete, we resorted to derived measurements like, e.g., the optical properties measurements to retrieve chlorophyll concentration. Additional observational datasets were selected from climatology data atlases of seasonal properties, when both in situ data or derived measurements were not available.

The biogeochemical observational variables available for the model initialization and validation are listed in Table 4.1. A homogeneous initial condition was set for the other state variables of the model in terms of carbon content and, where required, the chemical constituents of specific compartments were initialised through the Redfield ratio [64].

	MA21	**SHB**	**SF**
Damping frequency (T,S)	5 days	5 days	5 days
Atmospheric forcing	ERA-interim [62]	WRF model	ERA5 [65]
Experiment length	10 years	20 years	20 years
Observational data	PO4, NO3, NH4, SiO4, SPM	PO4, NO3, DOX, SiO4,	PO4, NO3, SiO4

Table 4.1: Summary of the model set up features, forcing and available biogeochemical observations for the three study sites. The following abbreviations are used: T=Temperature; S=Salinity; PO4=Phosphate; NO3=Nitrate; NH4=Ammonium; SiO4=Silicate; SPM=Suspended Particulate Matter; DOX=Dissolved Oxygen.

Chapter 5

Gulf of Trieste

5.1 Site characterization

The Gulf of Trieste is a very shallow bay located in the northern Adriatic Sea, shared by Italy, Slovenia and Croatia. This area, where the MA21 station is located (45.7°N and 13.65°E, in Figure 5.1), is a semi-enclosed basin with a surface of about 600 km^2 and a maximum depth of 26 meters [54]. Hydrography in the Gulf of Trieste is mainly influenced by the seawaters exchanges through its open Adriatic western boundary, by the meteorological conditions and by the discharge coming from the Isonzo River that contributes to about 90% of the freshwater inputs [66]. This area is strongly influenced by the katabatic northeasterly winds of Bora, occurring frequently in fall and winter seasons with a 'jet-like structure' over the gulf, which determine the cooling and mixing of the water column, and shape the circulation patterns and dense water formation [67, 68, 69]. Conversely, weaker meteorological conditions observed between May and August lead to the stratification of the water column [70, 53]. The combination of ex-

treme meteorological conditions with the specific morphological features of this site leads to significant sediment transport and resuspension rates of both organic and inorganic matter. This could have relevant impact on the dissolved inorganic nutrient budget [69], by increasing the nutrients concentrations in the sediment pore waters and in the overlying water, thus affecting the remineralization in the sediment surface layers [51]. The average distance of MA21 area from the coast is about 15 kilometers, which makes the influence of land dynamics fundamental to understand its hydrography. The Isonzo River fresh water pulses are the main driver of the surface salinity dynamic [41], while in depth, salinity is mainly influenced by the intrusion of deeper and salty waters entering form the Adriatic western boundary. The year-long discharges of this river represent also the major source of land-borne nutrients, in particular of nitrate, which largely induces seasonal fluctuations in the pelagic community structure and the occurrence of hypoxia/anoxia events [41, 71, 72, 73, 74, 23].

The seasonal evolution of the phytoplankton community in the Gulf of Trieste is strongly affected by the fresh water and nutrients input [74, 75]. In particular, the spring bloom primarily depends on the river flow variability, while the summer-early autumn deep biomass peak appears to be under the influence of the nutrients recycling [76, 77].

According to [78], the seasonal inorganic nutrients profiles are generally characterized by higher surface concentrations decreasing along the depth. Nitrate is higher in winter and it decreases toward summer period in the whole water column, while phosphate shows the maximum concentrations during autumn and then it progressively decrease. Silicate instead presents high concentration values in the deepest part of the water column during the whole year, due to the exchanges occurring at the sediment water inter-

face, and lower concentrations occurs in summer when the phytoplankton community is well established. The vertical profiles of dissolved oxygen are rather homogeneous during the entire year, with minimum values in the layers above the sediments. The highest values of oxygen were observed in winter and the lowest one in summer thus reflecting the seasonal temperature cycle.

During winter, the maximum values of ISM can be observed close to the sea floor, even if the strong vertical mixing causes the homogenization of the water column enhancing the water turbidity at the surface (Figure 5.2D). The ISM isolines become deeper in late spring and summer and the strong stratification prevent the ISM homogenization in the water column encouraging the deep vertical light propagation (also eventually stimulating primary production at deeper conditions).

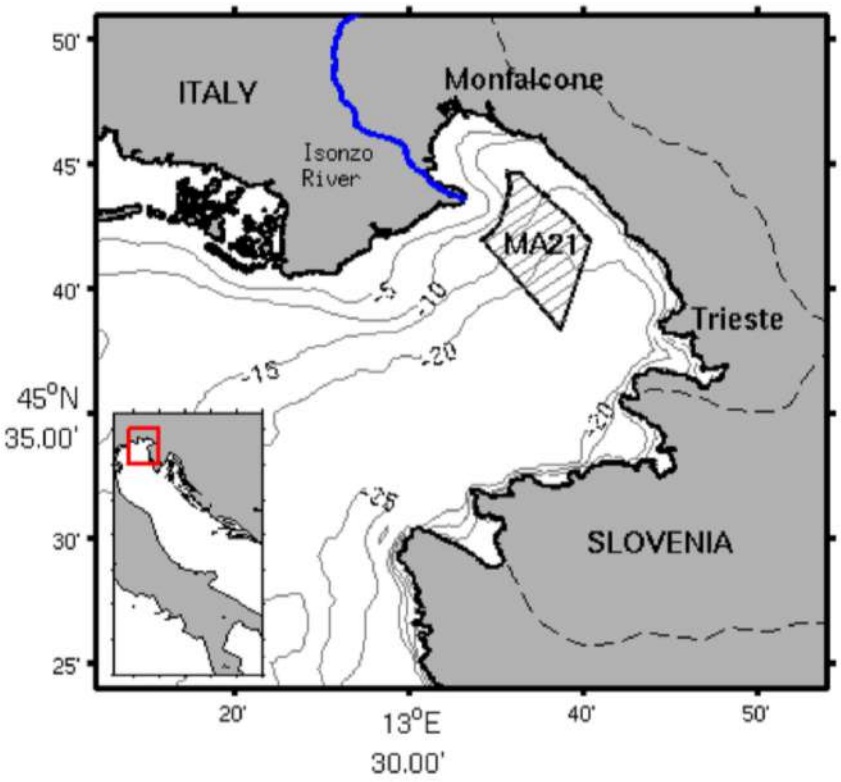

Figure 5.1: Geographical location and bathymetry of the MA21 monitoring area in the Gulf of Trieste. Figure from [41]

5.2 Model implementation

The 1D BFM-NEMO implementation was made with the aim to produce results comparable with the reference work of Mussap et al. [41] in simulating the benthic and pelagic interactions, and to assess the model robustness against available observational data.

The water column was represented through 31 logarithmically distributed vertical layers down to a maximum depth of 16 meters, with minimum resolution at both surface and bottom boundary layers of about 20cm. Numerical experiments were performed for a period of ten years and the last five simulated years were used to compute climatological fields in the evaluation of model's performance. The reference experiment **BPC-RETURN** and its companion **NO-RM** were forced with the same monthly climatologies from the ERA-interim dataset [62] with 6-hourly wind stress and daily solar radiation fields (see Table 5.1). The monthly climatologies of temperature and salinity were used for the initial conditions and to perform the restoring procedure computed using the data coming from the monitoring campaign carried out by ARPA-FVG (Agenzia Regionale per la Protezione dell'Ambiente) and OGS (Istituto Nazionale di Oceanografia e di Geofisica Sperimentale) (Table 5.1). All the biogeochemical components were initialized using the vertically profiles consistent with observed nutrients concentrations (see Table 5.1).

As the riverine influence is particularly prominent at this site, numerical experiments were performed by applying a surface restoring of nutrients (see 3.20) in order to mimic the effect of riverine loads. The restoring was done with a time frequency of 5 hours acting exclusively in the uppermost level of the grid and the evolution of nutrients data here applied is illustrated in

Figure 5.2 C. To further account for the influence of land-borne discharge of suspended solids, the model was forced with a background seasonal climatology of Inorganic Suspended Matter (ISM) as in [54]. Together with the shortwave radiation, the ISM vertical profiles are used by the BFM to compute the Photosynthetic Available Radiation E_{PAR} as described in Equation 3.22 to better constrain the way in which the light propagates throughout the water column.

The initialization of particulate and dissolved organic matter within the sediments in the performed numerical experiments was done using the reference values reported in Mussap et al. [41] and are also reported in Table 5.2. All the biogeochemical variables involved in the BPC sub-model (carbon, nitrogen, phosphate and silicate) share the same rate of remineralization, as well as the benthic burial rate applied to the sinking pelagic particulate organic matter (Table 5.2).

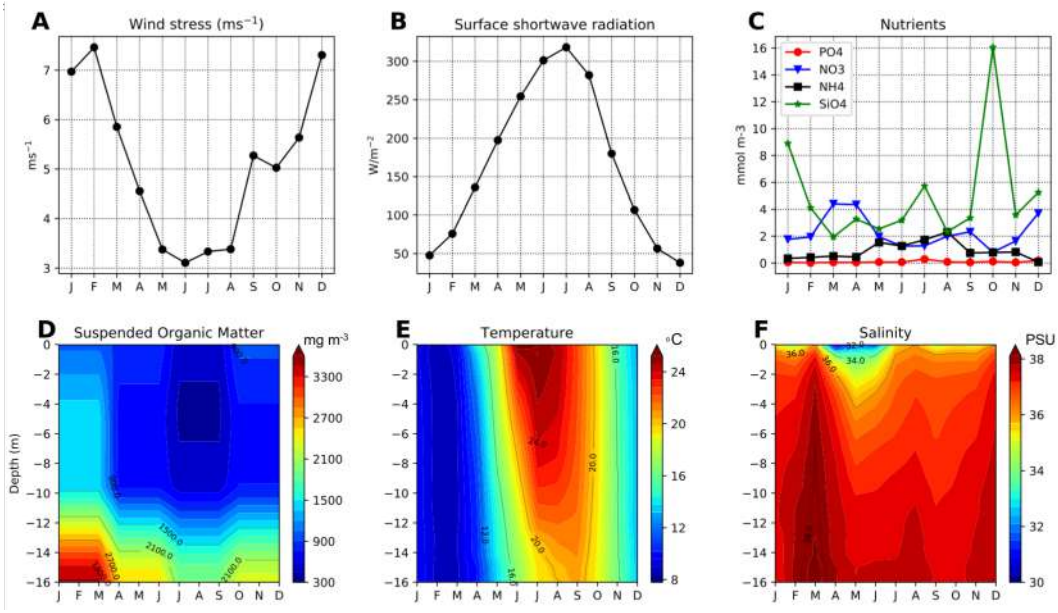

Figure 5.2: Monthly Climatologies (for the period see Table 5.1) of the atmospheric forcing: (A) Wind stress and (B) Solar radiation. Monthly data for the model initialization: (C) Nutrients, (D) Inorganic Suspended Matter (ISM), (E) Temperature and (F) Salinity.

Variable	Units	Time Period	Frequency
Atmospheric Forcings (ERA-Interim)			
Wind speed components	m s^{-1}	2000-2013	6 hours
Air temperature at 2m	°C	2000-2013	6 hours
Specific humidity	kg kg^{-1}	2000-2013	6 hours
Snowfall and Precipitation	kg m^{-2} s^{-1}	2000-2013	Daily
Long and Shortwave radiation	W m^{-2}	2000-2013	Daily
Observations (ARPA-FVG, OGS)			
Temperature	°C	2000-2011,2013	Monthly
Salinity	psu	2000-2011,2013	Monthly
Phosphate	mmol PO_3 m^{-3}	1998-2001	Seasonal
Nitrate	mmol NO_3 m^{-3}	1998-2001	Seasonal
Ammonium	mmol NH_4 m^{-3}	2000-2001	Seasonal
Oxygen	mmol O_2 m^{-3}	2000,2002-2011,2012	Seasonal
Chlorophyll-a	mg Chla m^{-3}	2000-2011,2013	Seasonal
Inorganic Suspended Matter	mg C m^{-3}	1997-2000	Seasonal

Table 5.1: Summary of atmospheric forcing fields and observational datasets, reporting reference units, temporal coverage and frequency of data.

Benthic variables initialisation and Parameters			
Variable	**Value**	**Units**	**Description**
Q6c0	520.0	mg C m^{-2}	Particulate organic Carbon in Sediment
Q6n0	220.0	mmol N m^{-2}	Particulate organic Nitrate in Sediment
Q6p0	1.4	mmol P m^{-2}	Particulate organic Phosphate in Sediment
Q6s0	150.0	mmol Si m^{-2}	Particulate organic Silicate in Sediment
Q1c0	10.4988	mg C m^{-2}	Labile organic Matter in Sediment
burvel R6	0.5	m d^{-1}	Burial Velocity for detritus
burvel PI	0.1	m d^{-1}	Burial Velocity for plankton
Remin Q1	0.01	d^{-1}	Remineralization rate of DOM
Remin Q6	0.0025	d^{-1}	Remineralization rate of POM

Table 5.2: Summary of data and parameters used in the BPC sub-model

5.3 Results

BPC-RETURN and NO-RM experiments comparison

The outcomes of the reference BPC-RETURN experiment are compared to those of the NO-RM one by considering the seasonal vertical profiles of Phosphate, Nitrate, Chlorophyll-a, Oxygen, and Ammonium, along with observational data, as shown in 5.3. A detailed analysis of the biogeochemical cycles simulated in the reference experiment is provided in the next section. Overall, the inclusion of the benthic sub-model significantly contributes to the improvement in the simulations of the here considered biogeochemical variables. The seasonal variability of nitrate and phosphate (Figure 5.3A-B) is poorly reproduced by the NO-RM experiment, with values that are rather flattened and straight along the vertical direction. In particular, the lack of the BPC process prevents the correct simulation of the seasonally nutrients-rich bottom water masses, while the two experiments have a comparable deep dynamic during summer when low nutrients concentrations are observed. The low nutrient concentrations obtained in the NO-RM test also lead to a significant underestimation of chlorophyll profiles that are always rather flatten, especially at the bottom levels, and lower than observations throughout the water column (Figure 5.3C). Conversely, the chlorophyll profiles of BPC-RETURN area characterized by a clear seasonality and the annual deep chlorophyll dynamics is also well reproduced. In both experiments, the oxygen seasonal profiles results to be very similar that is a direct consequence of air-sea reareation dynamics that are dominant in this very shallow site. In the BPC-RETURN experiment, a slightly higher oxygen consumption occurs in the last few meters of the water column as a consequence of the respiration process associated to the organic matter

degradation within the benthic compartment.

The only difference arise form the comparison of the ammonium seasonal cycle that appears to be slightly better simulated in the NO-RM experiment (5.3E). This directly points to the nitrogen remineralization dynamic in the sediments as the fluxes toward the water columns are partitioned between nitrate and ammonium through a rather simplistic parameterization (3.2.2).

A more quantitative assessment is offered by the comparison of the seasonal normalized mean bias (NMB) calculated over the entire water column for both the experiments and for all the biogeochemical variables discussed so far (Figure 5.4). The NMB metric was here selected to give an insight of the model skills in reproducing the variability along the year and better constrain critical deviations from observed data.

With the exception of ammonium, the NBM computed from the BPC-RETURN simulation is generally lower than the NO-RM one. In particular, it can be observed that the model error appears to be unevenly distributed along the different seasons, thus indicating that it is not necessarily related to any periodic physical and/or biogeochemical process (e.g, stratification, mixing, algal blooms). Moreover, dissolved inorganic nutrients show the highest error during the strong mixing periods (autumn or winter), while for chlorophyll during the stratification seasons (spring and summer).

A more in depth investigation about the relationships between the BPC sub-model parameterizations and the main biogeochemical pelagic state variables is treated in the sensitivity analysis Chapter 8.1

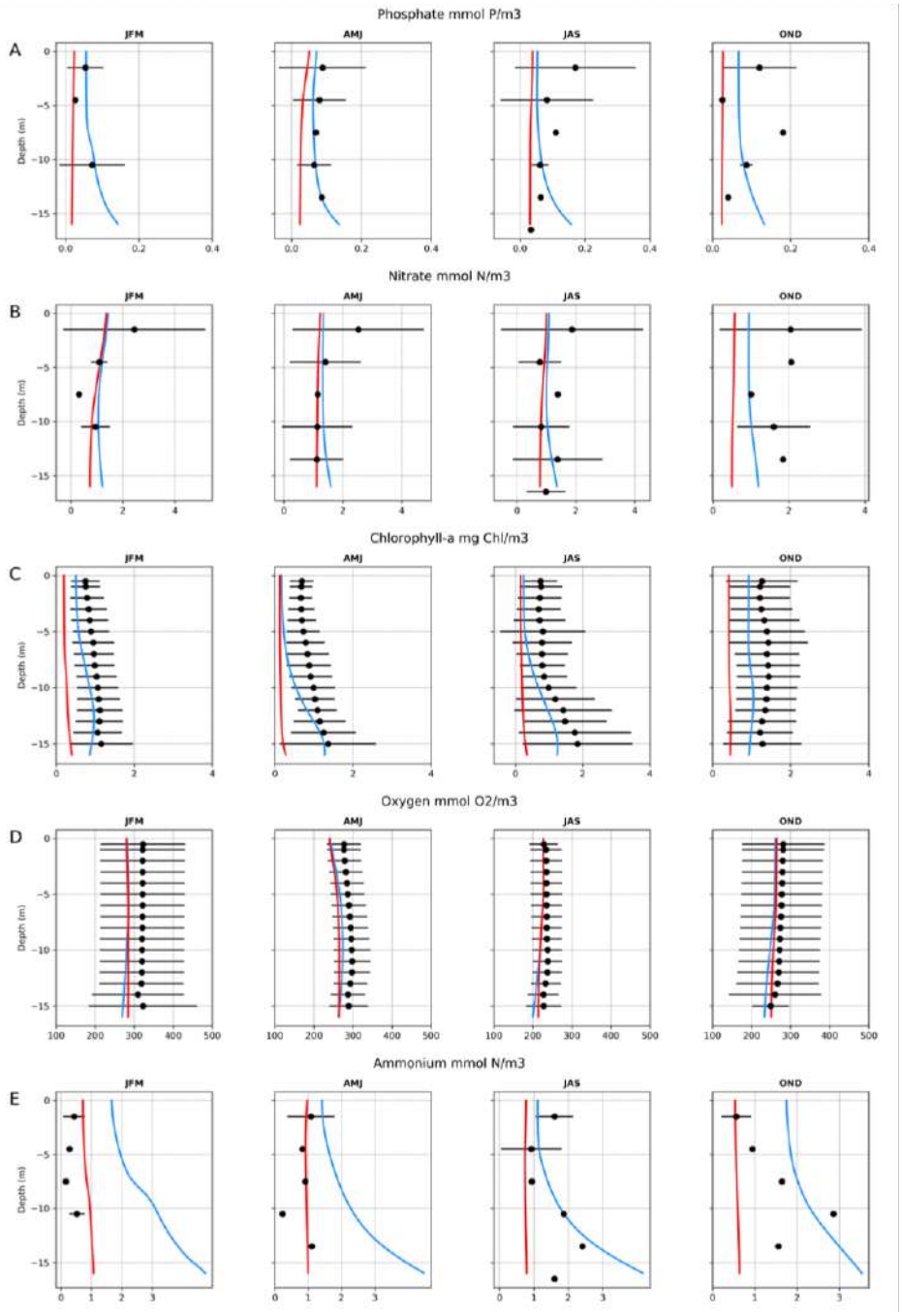

Figure 5.3: Comparison between NO-RM (red) and BPC-RETURN (blue) simulated seasonal mean climatological profiles for (A) Phosphate, (B) Nitrate, (C) Chlorophyll, (D) Oxygen and (E) Ammonium. Black dots indicate observations seasonal average and the horizontal bars their standard deviation. Abbreviations: JFM=winter, AMJ=spring, JAS=summer, OND=autumn.

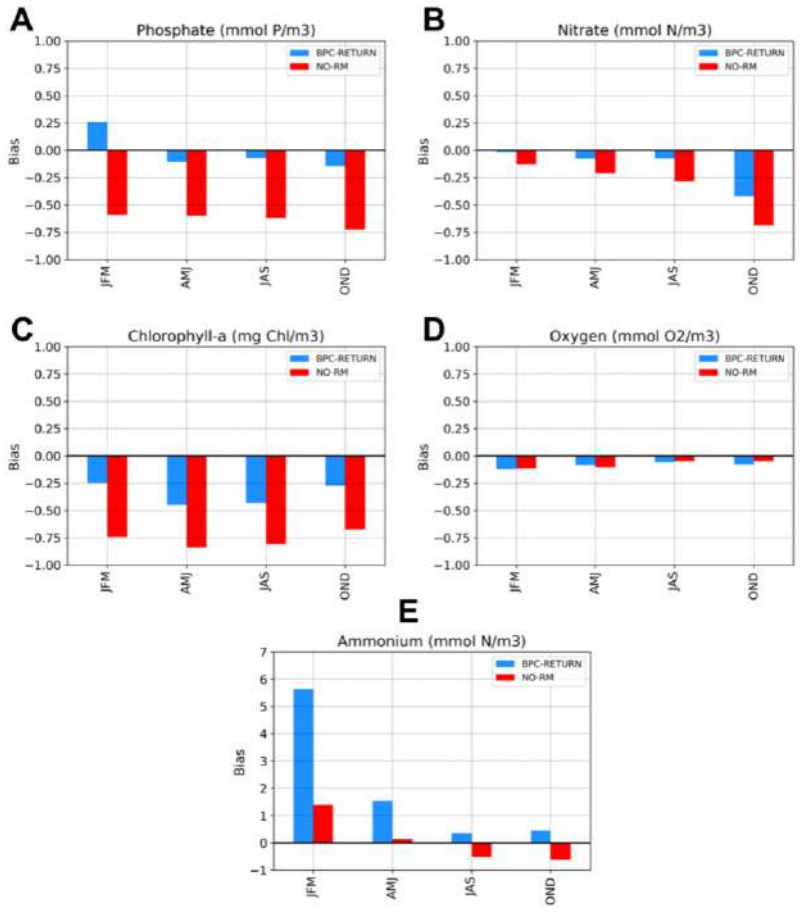

Figure 5.4: Seasonal normalized mean bias comparison between the the NO-RM (red) and the BPC-RETURN (blue) experiments for (A) Phosphate, (B) Nitrate, (C) Chlorophyll, (D) Oxygen and (E) Ammonium. Abbreviations: JFM=winter, AMJ=spring, JAS=summer, OND=autumn.

Assessment of simulated ecosystem dynamics

Outcomes of the reference BPC-RETURN experiment show a satisfactory representation of the observed seasonal variability for both inorganic nutrients and chlorophyll concentrations (Figure 5.3, blue line), by also catching the occurrence of a summer phytoplankton maximum near the bottom lev-

els. The rather low surface chlorophyll values are mainly constrained by the underestimation of nutrients, especially in summer and autumn for phosphate. Despite of the relaxation applied at the surface layer to mimic the influence of the Isonzo river loads, the dynamics of nutrient appears to be still poorly constrained and mainly driven by the consumption of primary producers. A possible solution would be to increase this riverine effect by extending the relaxation to more surface layers, but it was here neglected to avoid an excessive and potentially detrimental over-parameterization of this shallow system.

A broad view of the Nutrients-Phytoplankton-Zooplankton food chain evolution can be retrieved from the BPC-RETURN experiment, as represented in Figure (5.3) for nutrients and in the Hovmøller diagrams of the monthly climatological fields computed over last 5 simulated years (Figure 5.5 and 5.6). The spatial and temporal distribution of nutrients and the inherent response of phytoplankton and zooplankton are clearly reproduced by the model, also in relation to the seasonal evolution of the thermohaline vertical structure (see Figure 5.2 E,F). In fact, during autumn and winter, the high ventilation produces mixing that affects the entire water column leading the nutrients to rise toward the surface from October to January and to be uptaken by phytoplankton. Besides the nutrients limitation, chlorophyll also depends on other environmental factors such as solar radiation and temperature. The rather high concentrations of chlorophyll (Figure 5.5A) simulated at deeper layers during spring and early autumn are induced by the optimal environmental conditions of both seawater temperature and solar radiation (with respect to winter conditions) and nutrients availability. During late autumn and winter, the model water column is largely mixed as a consequence of the strong wind forcing and quite homogeneous trophic

conditions establish along the water column. The seasonal distribution of phytoplankton groups (Figure 5.5B-E) is characterized by the spring and summer blooms of diatoms that remain abundant over the whole year, while small-sized phytoplankton persist in the system but their abundance is far lower.

As direct measurements of zooplankton biomass or abundance were not available, the model offered a basis to evaluate their role within this ecosystem. The seasonal and vertical distribution of microzooplankton (Figure 5.6) are directly linked to that of phytoplankton that represents its main feeding pool, while the omnivorous zooplankton, being at the top of the model food chain, is characterized by a combined dynamic that follows both its preys throughout the year. The parameterized food matrix is summarized in Appendix A.5.

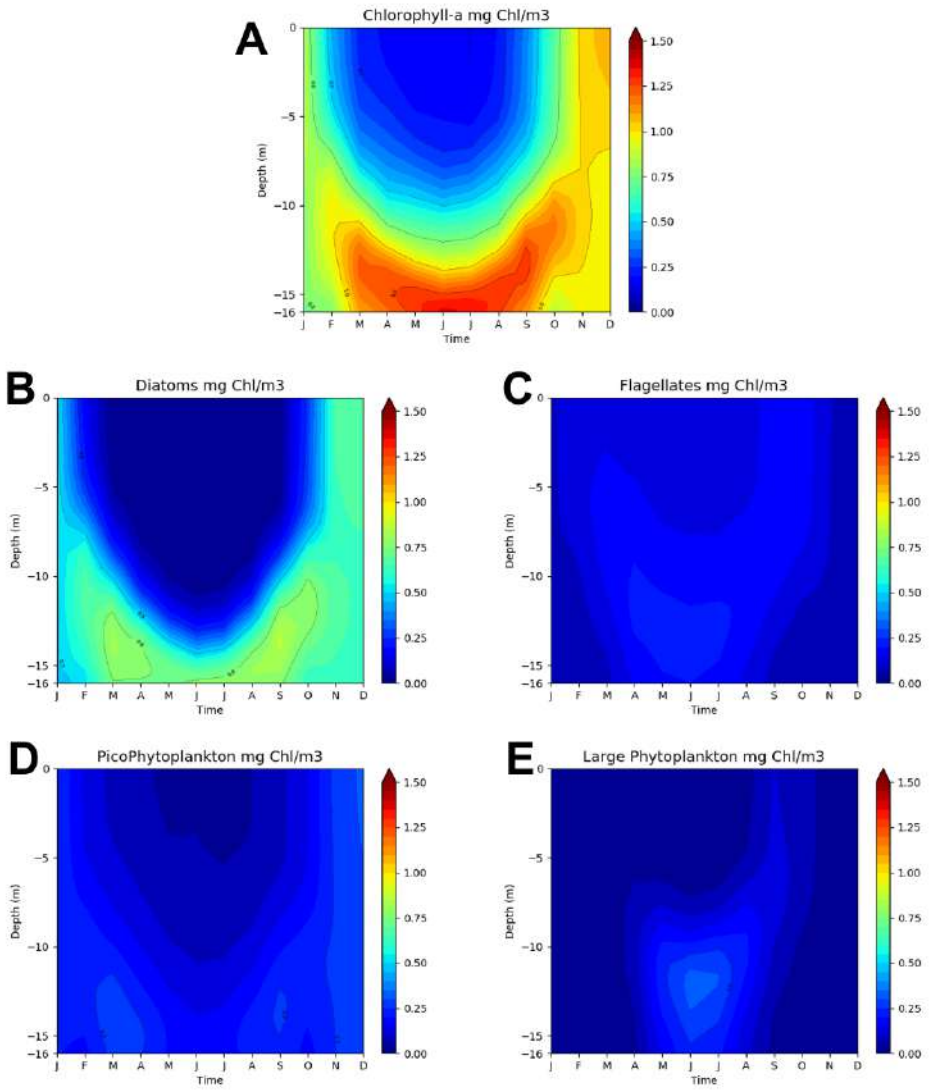

Figure 5.5: Monthly climatologies of the BPC-RETURN test for (A) Chlorophyll, (B) Diatoms, (C) Flagellates (D) Picophytoplankton and (E) Large Phytoplankton. Depth on the Y-axis, months on the X-axis.

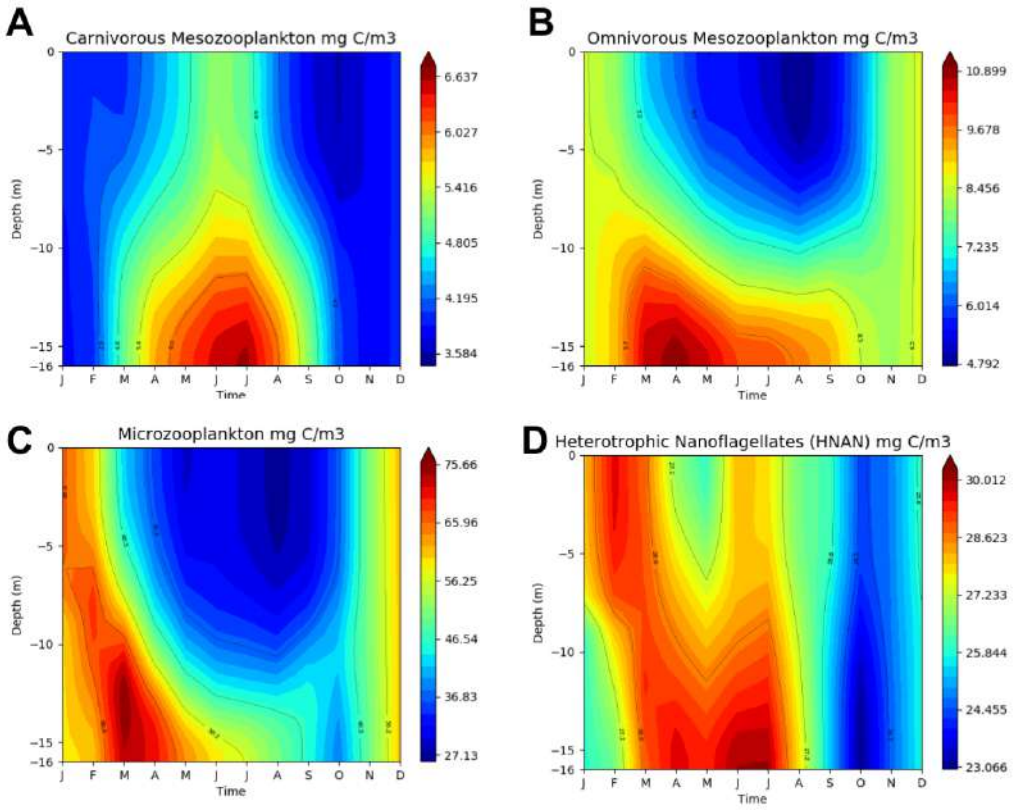

Figure 5.6: Monthly climatologies of BPC-RETURN experiment results for the Zooplankton component: (A) Carnivorous Mesozooplankton, (B) Omnivorous Mesozooplankton, (C) Microzooplankton and (D) Heterotrophic nanoflagellates. Depth on the Y-axis, months on the X-axis.

Chapter 6

Saint Helena Bay

6.1 Site characterization

St. Helena Bay (SHB) is the largest bay on the west coast of South Africa and it lies within the Benguela Current Large Marine Ecosystem (BCLME, Figure 6.1A). The BCLME is considered an eastern open boundary system [79, 58], being characterized by two warm currents at both its extremities: the Angola current system in the north and the warm Agulhas current system in the south. The SHB area is part of the Cape Province region (southernmost area of BCLME) and it is affected by the cold coastal branch of the Benguela current that, together with the wind stress, is the main driver of the coastal upwelling. This upwelling systems is more intense during the austral spring-summer period, when south-easterly trade winds reach their maxima, and it slows down in winter as the westerly continental winds start to prevail over the trade winds [58].

Besides the Benguela Current, this region is also characterized by strong coastal edge jets (Figure 6.1A) and by a poleward undercurrent acting along

the shelf slope [80], which transports land-borne sediments and organic nutrients from the mouth of the Berg River to the St. Helena Bay retention area.

The general circulation of St. Helena Bay is primarily governed by the interaction of four factors:

1. Large scale atmospheric circulation patterns determined by the perennial South Atlantic subtropical anticyclone, whose stable atmospheric high pressure center is opposed to the low pressure field over the subcontinent, with the consequent enhancement of the wind stress along the coast [81, 82, 83];

2. Mesoscale atmospheric perturbations, such as the eastward traveling mid-latitude cyclones (south of the African continent), periodically weaken or abate the south-easterly winds along the coast [81, 59] leading to a local weakening of the upwelling process [84];

3. Coastal topography shapes the local circulation system as the narrow shelves are more affected by the uplift of cold water with respect to wider ones [58];

4. The retroflection of the Agulhas Current generates a north westerly migration of warm rings and filaments that occasionally interact with the coastal upwelling [85, 86, 58, 59], especially when a more pronounced offshore-inshore thermal gradient occurs (with lower sea surface temperature values inshore and warmer offshore ones).

The interplay of the above factors leads to the peculiar seasonal cycle of seawater temperatures in St. Helena Bay [58, 59] with surface values that typically range between 12-15 °C and increase toward the offshore zone to

more than 17°C. The rise of cold and deep waters during spring and summer prevents the vertical propagation of the heating along the water column.

St. Helena Bay is characterized by an annually persistent phytoplankton community that supports a complex food web, thus being an elective spawning and larvae nursery area for a wide range of zooplankton and fishes species. Nutrients distribution is closely associated to the upwelling system [87, 88], with high rates of advected nutrients from the bottom levels toward the sea surface from September to April and lower concentrations during the 'no-upwelling' period between May and August. The intensity of the upwelling event drives nutrients variability that in turn influence the rates of primary productivity [87, 88]. As stated by Pitcher et al. [89], the weaker stratification conditions and nutrients injection are frequently responsible of episodic harmful red tides that lead to mass mortality events for zooplankton and in particular for rock lobster. The interplay of local physical, hydrodynamical and biological processes leads St. Helena Bay to be periodically characterized by low oxygen water [90]. During late summer-early autumn the stratification intensifies and phytoplankton become nutrients limited, so the biomass concentrations decrease occurs at the expense of excessive consumption of oxygen. Despite the ecosystemic relevance of retention areas such as St. Helena Bay [91, 92], their role in the development and maintenance of organic rich sediments and coupled elemental cycling is less understood [93] due to the lack of systematic monitoring activities.

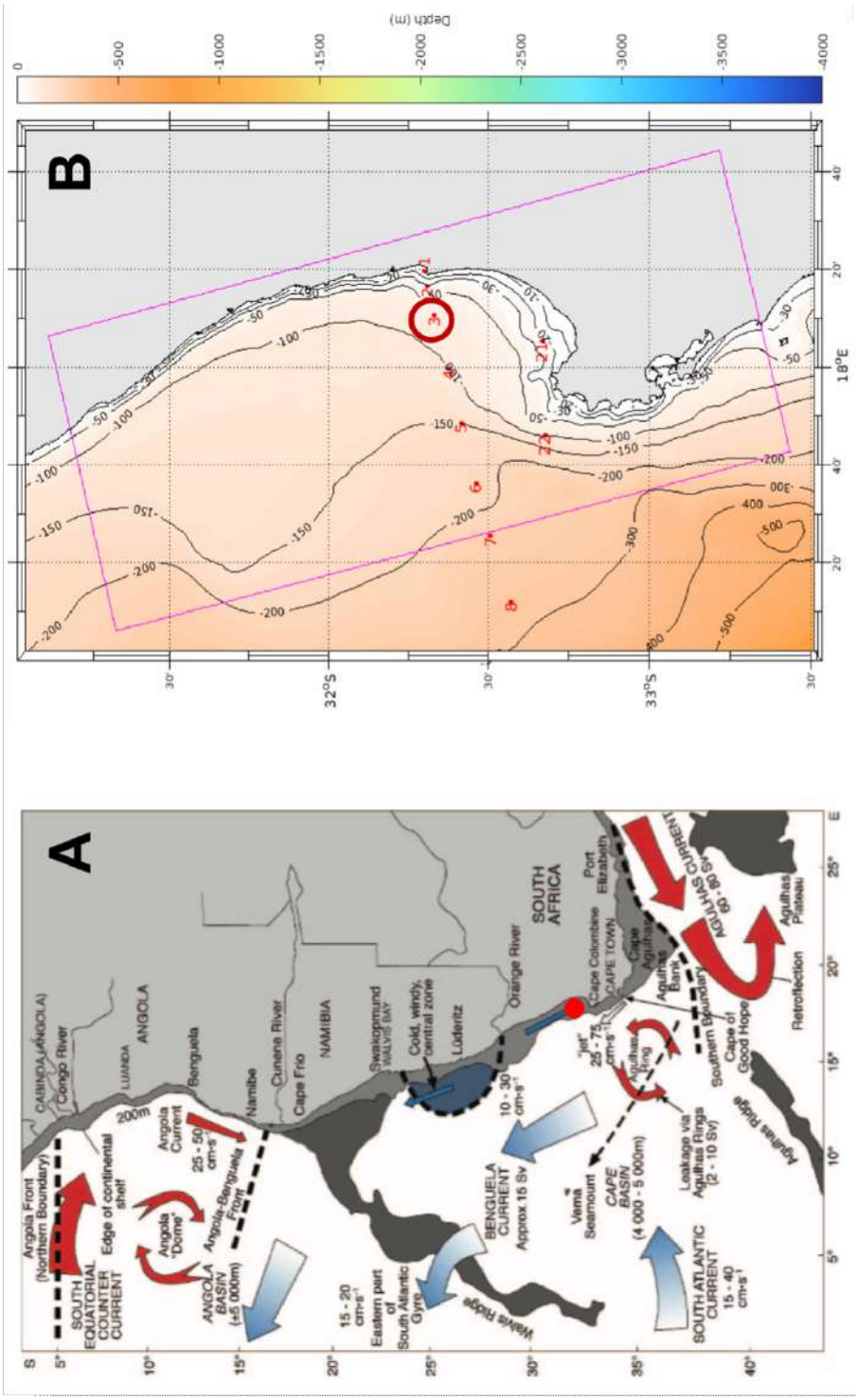

Figure 6.1: Area of Study. Figure A: Map of the BCLME adapted from Shannon et al. [58], Figure B: Zoom of the area of interest: SHB Station 3 red circle. Figure by G. Fearon (University of Cape Town).

6.2 Model implementation

The 1D NEMO-BFM configuration implemented in St. Helena Bay aims to reproduce the BPC climatology of the station 3 of the St. Helena Bay monitoring line (SHB, Figure 6.1 B). The station is positioned at a latitude of 32.16°S and a longitude of 17.50°E and has a maximum depth of 78m. A staggered grid composed by 50 logarithmically distributed vertical levels was implemented, with a maximum spacing of ∼3m in the bottom-most level. The model was used to perform 20 years-long simulations (starting from year 2006) and results from the last 10 years are presented in the following analyses. This choice was done to exclude the initial adjustment phases of the model often characterized by drifts in both benthic and pelagic components.

The atmospheric forcing used in both BPC-RETURN and NO-RM experiments were extracted from the high-resolution (∼ 3km) simulation over the period 2006-2012 of the atmospheric-ocean coupled regional model WRF-ROMS provided by the Climate Systems Analysis Group at the University of Cape Town (courtesy of G. Faeron). Table 6.1 shows the main characteristics of the atmospheric forcings. Monthly climatology of wind speed and solar radiation were computed from the high-resolution atmospheric dataset (Figure 6.2) to provide an overview of the forcing features, similarly to the other case studies.

Seawater temperature and salinity data come from the hydrographic sampling along the SHB in the framework of the BENEFIT (Benguela Environment and Fisheries Interactions and Training) program carried out by the Department of Environmental Affairs of South Africa. Observations are made of Conductivity-Temperature-Depth (CTD) casts from sea surface to

within 5-10 m of seafloor and were performed from April 2000 to December 2017 with a monthly frequency (Table 6.1).

To reproduce a correct density structure and a non drifting annual cycle of the water column, a relaxation of 5 days was adopted using the above temperature and salinity monthly climatological fields. From the computed monthly climatologies (Figure 6.2 C,D) it is clear how the stability of the water column is mainly driven by temperature and to a lesser extent by salinity, which is also shows a certain degree of seasonality.

The temperature restoring method ensures that the model is constrained to maintain the thermocline seasonality, but this condition may not be sufficient to realistically reproduce the vertical distribution of pelagic state variables induced by the upwelling. A brief characterization of the upwelling seasonality it is here proposed to highlight the specific hydrodynamic features of SHB station, by considering the climatological distribution of three proxies: seawater temperature, chlorophyll-a and vertical velocities (see Figure 6.3 A and Table 6.1). The first step for the detection of the upwelling duration was based on the annual trend of the 11°C isotherm, which indicates that vertical water mass motions lasts from September until April. According to literature, peaks of chlorophyll occur during the upwelling periods [94, 89] with two maxima in late summer and early spring, as in the case of the SHB area where the phytoplankton activity onset (September) and offset (April) coherently with the upwelling dynamics. Note that, chlorophyll-a data used here have been extrapolated from the fluorometer measurements under the rather crude assumption that in-situ concentrations corresponded to the original data scaled by one order of magnitude. This appeared to us a conservative approach, as the determination of chlorophyll-a concentration by fluorescence depends on the optical properties of the ocean water and

the factors for converting units of fluorescence varies up to 50% [95]. Lastly, the vertical velocity obtained from the WRF-ROMS model simulations show that the period of inactivity begins in May and ends in August ($w < 0$ in all the vertical levels in a range between 10-78m).

As the explicit prescription of vertical velocities would lead to un-reaslistic features in the one-dimensional model, the vertical motions due to the upwelling dynamics were here approximated by adjusting the vertical eddy diffusivity coefficient of tracer transport. This coefficient refers to the vertical turbulent contribution to oceanic properties transport and it was set to $1.0e^4$ m^2/s, namely the double with respect to the other implemented sites.

Observations for nitrate, phosphate, silicate and oxygen were obtained from the monthly profiles of the CSIRO digital Atlas of Regional Seas (CARS) [96]. The silicate and chlorophyll-a monthly climatological profiles were derived from the SHB in-situ samples, with the latter scaled according to procedure described in the above paragraphs. These data were used to initialize the corresponding BFM pelagic state variables.

No observational data on the benthic organic matter were found for the SHB area. However, Monteiro et al. [97] estimate that St Helena Bay is characterized by high sedimentary flux toward the bottom, thus supporting the hypothesis that to well reproduce the SHB dynamic a rather active BPC parametrization should be used. The set of parameters adopted for the BPC are listed in Table 6.2.

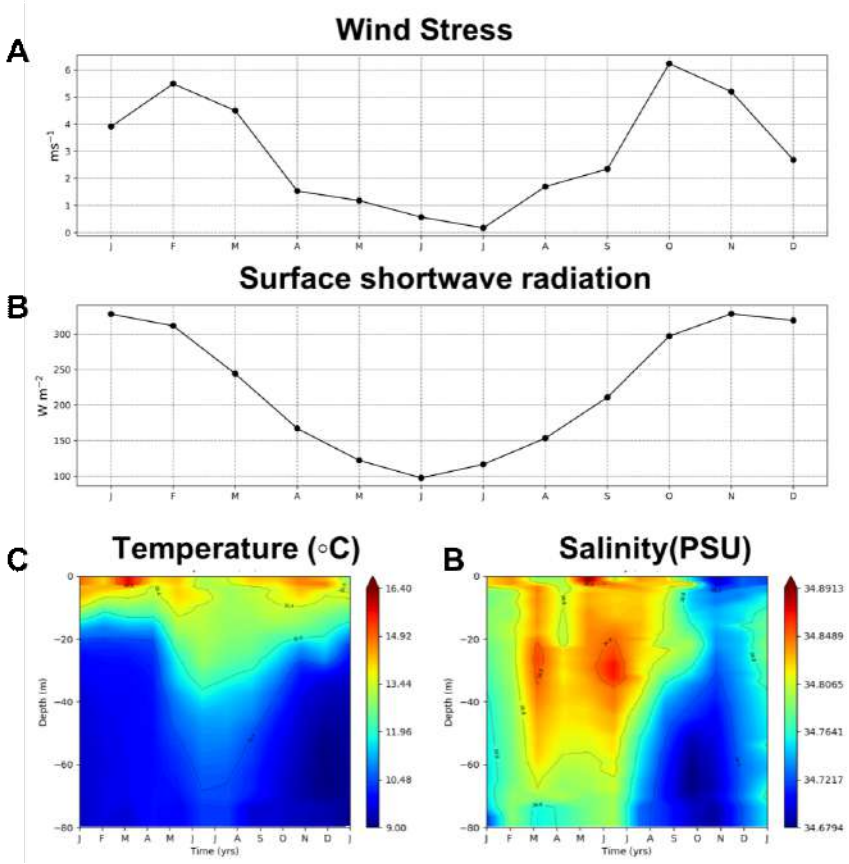

Figure 6.2: Atmospheric forcing climatological timeseries for (A) Wind speed (B) and Shortwave solar radiation; monthly climatological Hovmøller representation of (C) Temperature and (D) Salinity (dataset details are provided in Table 6.1)

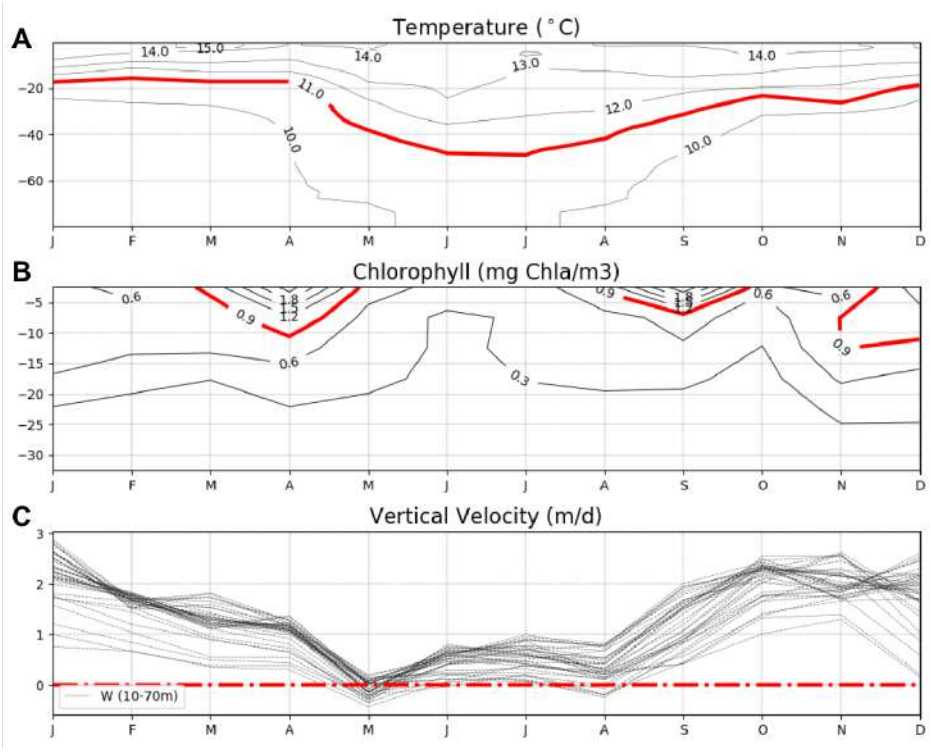

Figure 6.3: Monthly climatological Hovmøller representation of (A) Temperature, (B) Chlorophyll-a (C), and vertical velocity used to characterize the upwelling dynamics at SHB (data details in Table 6.1). The red line individuates the selected threshold values used as proxies for upwelling detection.

Variable	Units	Period	Frequency
Atmospheric Forcings (WRF-ROMS)			
Wind speed components	m s^{-1}	2006-2012	1 hour
Air temperature at 2m	°C	2006-2012	1 hour
Specific humidity	kg kg^{-1}	2006-2012	1 hour
Snowfall and Precipitation	kg m^{-2} s^{-1}	2006-2012	1 hour
Long and Shortwave radiation	W m^{-2}	2006-2012	1 hour
Observations (SHB)			
Temperature	°C	2000-2017	Monthly
Salinity	psu	2000-2017	Monthly
Chlorophyll-a	mg Chla m^{-3}	2001-2011,2013	Monthly
Observations (CARS Atlas)			
Phosphate	mmol PO_3 m^{-3}	1960-2009	Monthly Climatology
Nitrate	mmol NO_3 m^{-3}	1960-2009	Monthly Climatology
Silicate	mmol Si_3 m^{-3}	1960-2009	Monthly Climatology
Oxygen	mmol O_2 m^{-3}	1960-2009	Monthly Climatology

Table 6.1: Summary of atmospheric forcing fields and observational datasets, reporting reference units, temporal coverage and frequency of data.

Benthic initialisation of standard variables and parameters			
Variable	**Value**	**Units**	**Description**
Q6c0	520.0	mg C m^{-2}	Particulate organic Carbon in Sediment
Q6n0	220.0	mmol N m^{-2}	Particulate organic Nitrate in Sediment
Q6p0	1.4	mmol P m^{-2}	Particulate organic Phosphate in Sediment
Q6s0	150.0	mmol Si m^{-2}	Particulate organic Silicate in Sediment
Q1c0	10.4988	mg C m^{-2}	Labile organic Matter in Sediment
burvel R6	1.0	m d^{-1}	Burial Velocity for detritus
burvel PI	0.1	m d^{-1}	Burial Velocity for plankton
Remin Q1	0.01	d^{-1}	Remineralization rate of DOM
Remin Q6	0.0025	d^{-1}	Remineralization rate of POM

Table 6.2: Summary of data and parameters used in the BPC sub-model. Organic nutrients has been initialised according to the Redfield ratio [64]

6.3 Results

BPC-RETURN and NO-RM experiments comparison

As stated in 4.2, the seasonally averaged vertical profiles obtained from the twin set of numerical experiments, namely **BPC-RETURN** and **NO-RM**, have been compared along with observations for phosphate, nitrate, silicate, chlorophyll-a, and oxygen (Figure 6.4). The NO-RM experiment is characterized by rather flat vertical profiles for all the variables considered, while the main observational data seasonal features are satisfactorily reproduced in the BPC-RETURN one. In particular, the chlorophyll simulated in the NO-RM experiment shows a slight seasonal cycle with two main peaks around April and September (in agreement with the chlorophyll climatology shown in Figure 6.3). Clearly, the low content of inorganic nu-

trients in the water column at the beginning of the year (JFM) relates to the absence of benthic remineralization processes. Although the slight deep underestimation, the inorganic vertical profiles are well reproduced together with the chlorophyll dynamics. The seasonal dynamic of the oxygen is well reproduced in the BPC-RETURN simulation, contrarily to the NO-RM experiment, as a consequence of the enhanced pelagic production-consumption cycle under higher nutrient concentrations and the respiration associated to the benthic remineralization processes.

A more objective comparison was here carried out by computing the seasonal normalized mean bias (NMB) over the entire water column for both the experiments (Figure 6.5). As one can see, the NO-RM experiment has significantly high NMB values throughout the year for all the considered variables with respect to the BPC-RETURN one. The latter has a rather uniform error in the simulation of silicate, while deviations from the observed data of the other variables are more evident in austral autumn and winter when the upwelling is assumed to be weaker. Such a mismatch is partly attributable to the enhanced mixing introduced by the high vertical eddy diffusivity that was used to mimic the upwelling dynamics, as it was not modulated in time to avoid an over-parameterization of the system.

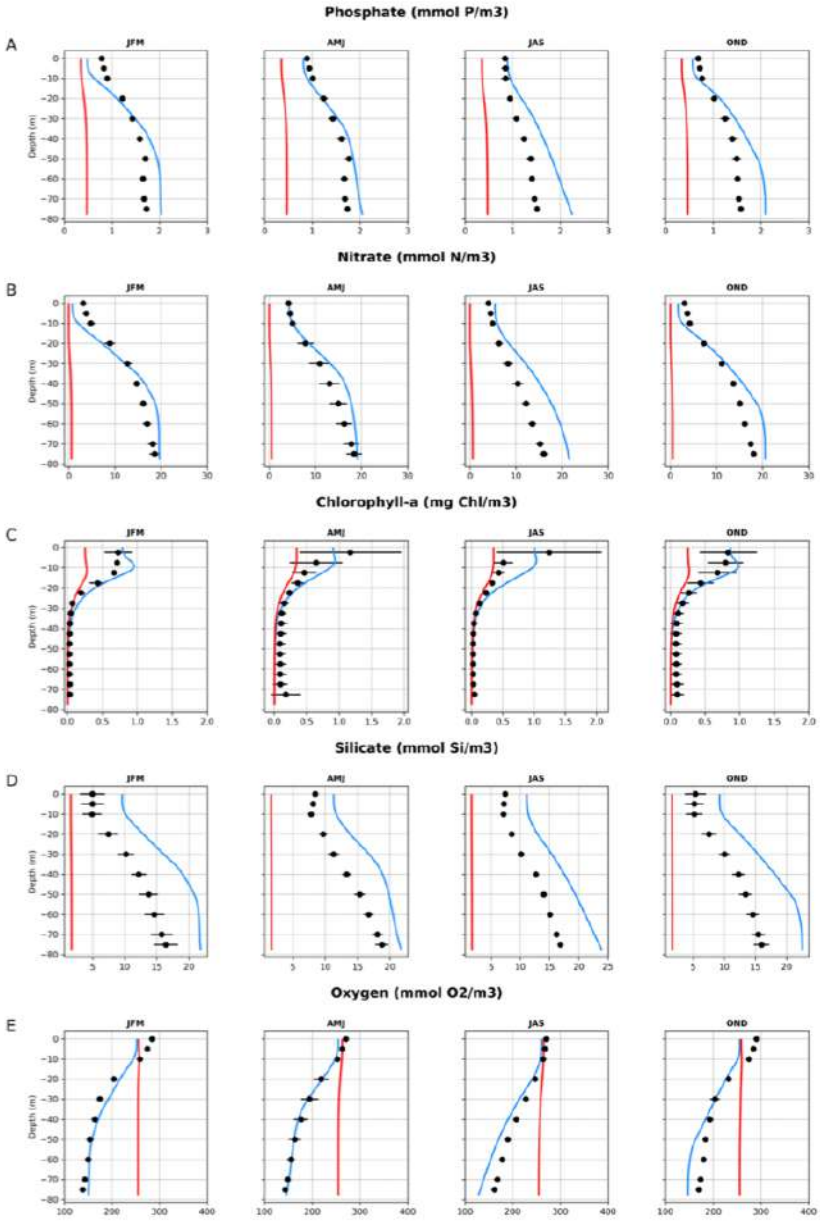

Figure 6.4: Comparison between NO-RM (red) and BPC-RETURN (blue) simulated seasonal mean climatological profiles for (A) Phosphate, (B) Nitrate, (C) Chlorophyll, (D) Silicate and (E) Oxygen climatological seasonal profiles. Black dots indicate observations seasonal average and the horizontal bars their standard deviation. Abbreviations: JFM=winter, AMJ=spring, JAS=summer, OND=autumn.

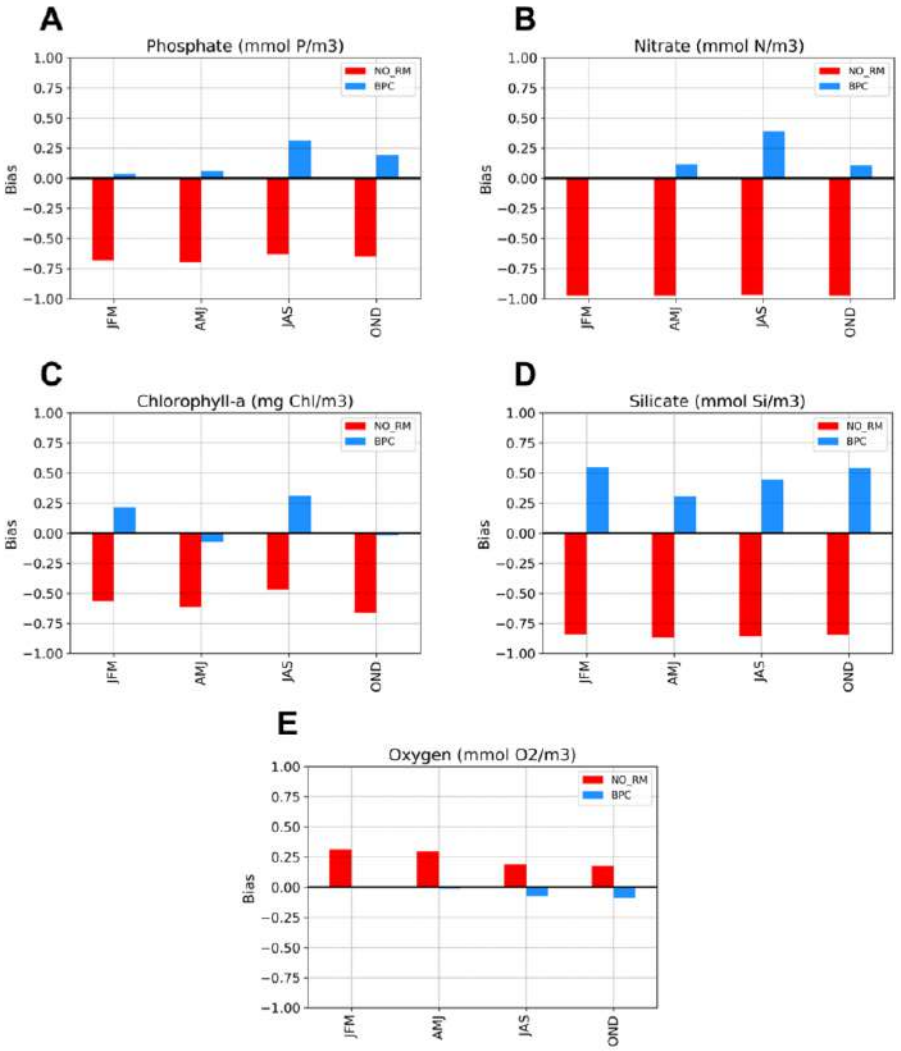

Figure 6.5: Seasonal normalized mean bias comparison between the the NO-RM (red) and the BPC-RETURN (blue) experiments for: (A) Phosphate, (B) Nitrate, (C) Chlorophyll, (D) Silicate and (E) Oxygen. Abbreviations: JFM=winter, AMJ=spring, JAS=summer, OND=autumn.

Assessment of simulated ecosystem dynamics

Overall, the outcomes of the reference BPC-RETURN experiment were in

a good spatiotemporal agreement with the available observations, particularly for the bottom inorganic nutrients (Figure 6.4). The seasonal variability of chlorophyll was coherently reproduced, although the model slightly overestimate the subsurface values and it exhibits a rapid decrease of concentrations near the bottom with respect to the observed data. Nevertheless, it is conceivable that the overestimation in the upper 20 meters may be related to the simulated density structure of the water column. Even making a strong restoring of temperature and salinity, a small source of errors can affect the mixed layer features simulated by the model.

In Figure 6.6 the monthly climatologies of the main state variables for the reference experiment are shown along with the observational data (Table 6.1). In particular, the model well reproduces the evolution of chlorophyll-a within the first 20 meters and a marked peak takes place around September. During the austral summer (JFM) a strong stratification setup at about 20 meters and it prevents the penetration of nutrients above the thermocline, thus determining the low nutrient conditions at the surface. At the end of the austral summer the stratification lessens as the thermocline is broken up by upwelled waters and nutrients concentrations at the surface are remarkably high. Nevertheless, the model does not properly reproduce the depth of the nutricline between June and Juky, which results to be very sharp in the CARS data and rather flattened in BPC-RETURN simulation. Both nutricline and thermocline simulated error propagates in the next level of the food chain causing a phytoplankton blooms with a certain delay with respect to the observed data. The oxygen dynamic is fairly reproduced as low and deep oxygen conditions persist from June until October when the vertical mixing makes deep waters slightly more oxygenated, whereas low oxygen conditions occurring between February an April at the bottom layers were not caught

by the model. The evolution of the benthic carbon pools represented in Figure 6.7 shows an initial accumulation phase of organic matter and a near equilibrium state between pelagic sedimentation and benthic remineralization fluxes is achieved after 5 years. This makes hypothesize that there is a pronounced link between the pelagic inorganic nutrients overestimation of the BPC-RETURN experiment and the simulated benthic realm. A more in depth investigation and discussion about the degree of coupling between the pelagic and benthic realms will be treated in Chapter 8.1.

The seasonal succession of phytoplankton reproduced by the model (Figure 6.8) appears to be quite consistent with previous literature evidences [98]. A first diatoms shallow bloom occurs during austral winter (JAS) followed by a stable diatoms production at about 10m of depth during austral spring, while flagellates are present during the entire upwelling period (OND-JFM) and picophytoplankton dominates during the austral summer period (JFM). Large phytoplankton (not shown) suddenly disappears at the beginning of the numerical experiment and never recovers.

Although observations of zooplankton biomass were not available, the analysis of its spatial and temporal distribution is worthy of some considerations (Figure 6.9). The spatio-temporal distribution of all the zooplankton groups considered by the model is in agreement with the distribution of the relatives preys. In particular, the diminished herbivorous zooplankton biomass observed in the first 20 meters during JJA (see Figure 6.9 C-D) is likely related to the corresponding diatoms bloom visible in Figure 6.8 A. The parametrized food matrix is summarized in Appendix A.5

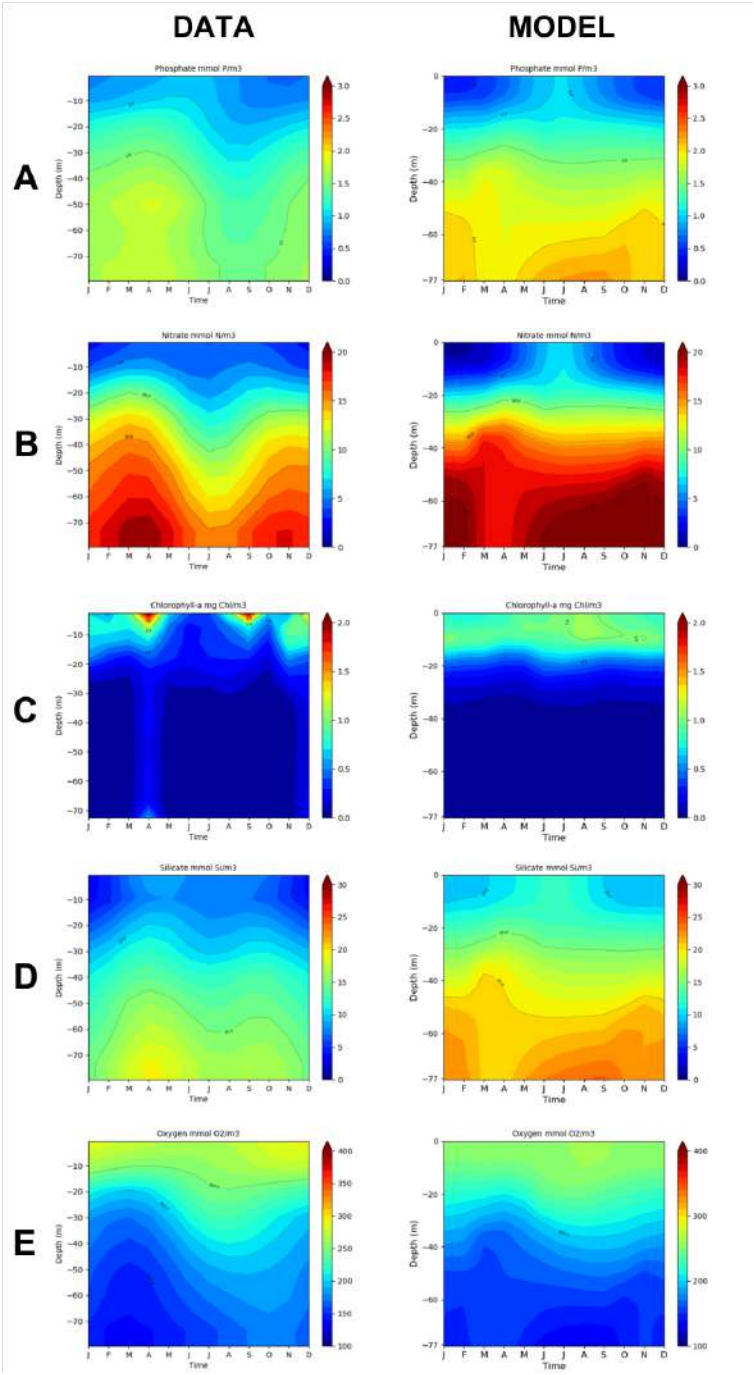

Figure 6.6: Monthly climatological Howmøller plots of observed data (left panel) and BPC-RETURN experiment outcomes for (A) Phosphate, (B) Nitrate, (C) Chlorophyll, (D) Silicate and (E) Oxygen. For the observational data see Table 6.1. Depth on the Y-axis, months on the X-axis.

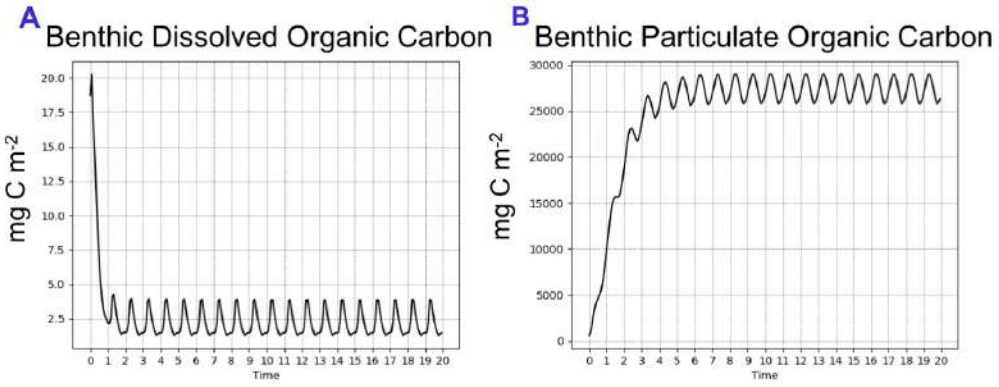

Figure 6.7: Time series of the simulated benthic (A) Dissolved and (B) Particulate Organic Carbon.

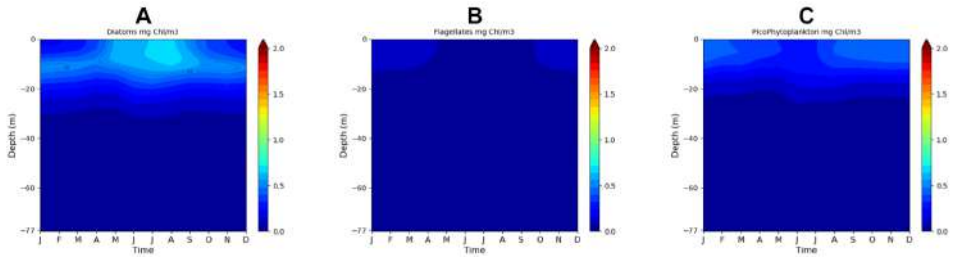

Figure 6.8: Monthly climatologies of BPC-RETURN experiment results for the Phytoplankton component: (A) Diatoms, (B) Flagellates and (C) Picophytoplankton. Depth on the Y-axis, months on the X-axis.

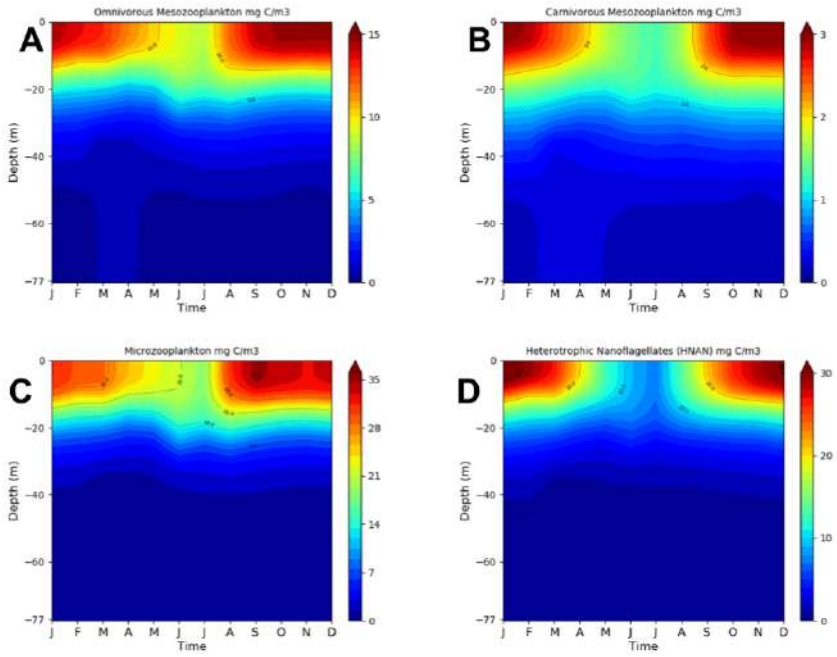

Figure 6.9: Monthly climatologies of BPC-RETURN experiment results for the Zooplankton component: (A) Omnivorous Mesozooplankton,(B) Carnivorous Mesozooplantkon,(C) Microzooplankton, and (D) Heterotrophic Nanoflagellates. Depth on the Y-axis, months on the X-axis.

Chapter 7

Svinøy Fyr

7.1 Site characterization

The Svinøy Fyr station (hereafter SFyr) is located in the South-West coast of Norway (∼62.27°N and ∼5.10°E in Figure 7.1), over the shelf break along the Svinøy Fyr hydrographic section.

This monitoring section has been investigated since the beginning of the last century [99] with major interest on the Atlantic inflow features and its interannual variability [100], but only few studies dealt with the characterization of the Norwegian South-Western continental shelf dynamics.

The area is subject to strong winds mainly coming from south south-west [101] that makes it fall within the category of the sub-polar regions [102, 103]. Its hydrological regime is determined by the interplay between (i) the poleward extension of the Gulf Stream that serves as a conduit of warm and saline waters from the North Atlantic to the Arctic Ocean [104] and (ii) the topography trapped Norwegian Atlantic Current that is considered the warm barotropic and inner branch of the North Atlantic current (see 7.1).

The latter prevents the formation of sea ice at these latitudes, conversely to what happen at the opposite coast in Greenland.

During winter the downward mixing occurs by the convection of cooled surface waters in addition to the wind-driven turbulence that deepens the mixed layer [103], persisting until late spring, while warmer and shallow stratified conditions are established in summer. The Norwegian continental shelf is a very high productive marine ecosystem [103]. Low temperature and high nutrients concentrations in SFyr station stay stable during winter, when the strong winds favour the formation of a deep mixed layer, by setting up favourable trophic conditions to fuel the early spring phytoplankton bloom. The summer stratification prevents the nutrients regeneration at the surface making the post-bloom period to last around three months. The weakening of stratification and the convective vertical motions occurring in autumn allow the injection of nutrients to the surface determining a weak second peak of phytoplankton. According to Loeng et al. [105], this site is characterized by a phytoplankton-zooplankton-fish short food chain that generates a high content of sunk organic detritus escaping from the euphotic zone. Moreover, observations on biogenic sedimentation indicate how a large portion of the carbon fixed annually by phytoplankton falls ungrazed to the sediments [106, 107], thus leading a great proportion of the primary productivity to be recycled through the benthic activity [108].

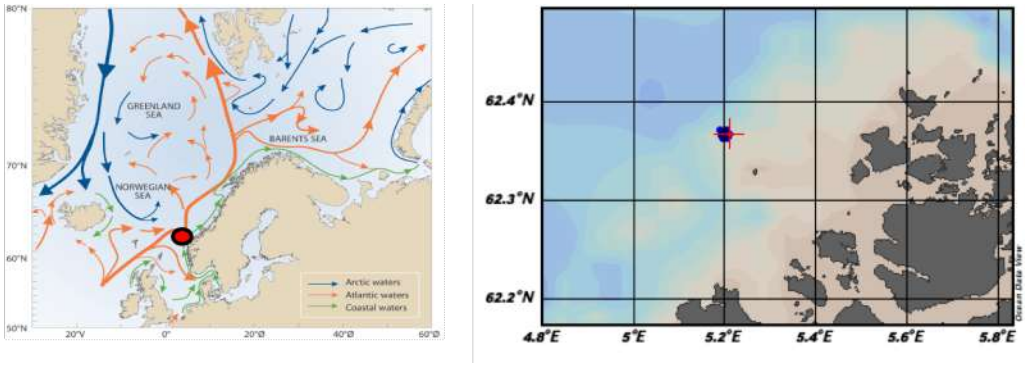

Figure 7.1: General circulation structures of the Norwegian Sea (Left panel). The orange line is the Norwegian Atlantic Current, the green line refers to the Coastal waters current and the blue line refers to the Arctic waters. Zoom on the Svinøy Fyr station location (Right panel).

7.2 Model implementation

The station here considered is the first and shallowest one of the Svinøy Fyr hydrographic section, located at the edge of the continental shelf with an average depth of ∼150m.

A vertical grid composed by 50 vertical levels with the maximum spacing of around 8 meters in the bottom-most level was used to discretize the water column.

In this implementation, the 1D NEMO-BFM model simulations were carried out for a 20 years time period (2000-2019) and the results presented in the next section refer to the monthly and seasonal climatology of the last 10 years. This choice was made to exclude from the analysis the initial drift that occurs in the biogeochemical dynamics.

Table 7.1 summarizes the main characteristics of the atmospheric data used in this study, obtained from the ERA5 climate reanalysis produced by the ECMWF for the period 2000-2019 [65]. As observable in Figure 7.2, strong winds occur from September to March enhancing convective vertical motion and the deepening of the thermocline. Similarly total precipitation (snow and rain) presents maximum values between September and January.

Data used to initialize the model come from the publicly distributed data of the Institute of Marine Research - Norwegian Marine Data Centre (INR-NMD) for the period 1995-2015 (see Table 7.1). Seawater temperature and salinity CTD measurements were carried out with a monthly frequency, with the exception of the month of December. To overcame this lack of data, a mean profile was created for December month by considering the data available from mid November to mid January over the entire dataset and then the monthly climatology was generated for both variables. As for previous case

studies, temperature and salinity have been restored with a time frequency of 5 days. As for physical quantities, the nutrient profiles data were produced by the INR-NMD and are freely downloadable on the public catalogue of the SeaDataNet infrastructure (www.seadatanet.org). This dataset was used to generate the monthly climatological fields for phosphate, nitrate, silicate and chlorophyll-a, as described in Table 7.1.

No site-specific observational data were found for the organic matter carbon content in the sediments. Thus, the benthic organic matter at this station was initialised using the average organic carbon values from the last 10 years (out of 20) obtained from a preliminary simulation with the model. The other organic matter constituents, namely nitrates, phosphates and silicates, were set using the respective Redfield ratios [64] (see Table 7.2).

The remineralization rates have been doubled with respect to the other study areas to make the sediment more active, in agreement with literature findings [60, 103].

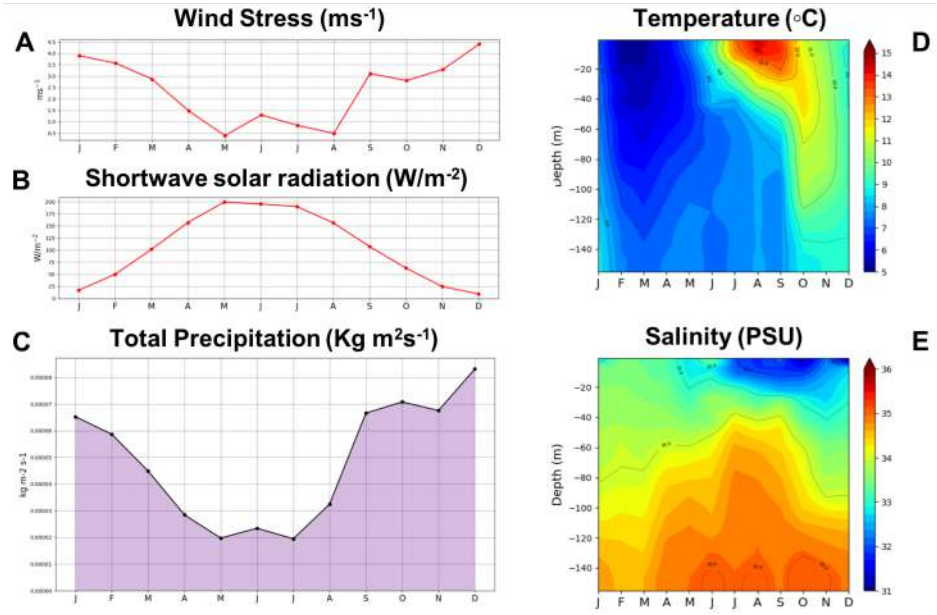

Figure 7.2: Monthly mean timeseries of climatological atmospheric forcing for: (A) wind speed, (B) shortwave solar radiation and (C) total precipitation (snow and rain). Monthly mean climatological profiles constructed from the available observations of seawater (D) temperature and salinity (E). Additional details are provided in Table 7.1

Variable	Units	Period	Frequency
Atmospheric Forcings (ERA5)			
Wind speed components	m s^{-1}	2000-2019	6 hours
Air temperature at 2m	°C	2000-2019	6 hours
Specific humidity	kg kg^{-1}	2000-2019	6 hours
Snowfall and Precipitation	kg m^{-2} s^{-1}	2000-2019	Daily
Long and Shortwave radiation	W m^{-2}	2000-2019	Daily
Observations (INR-NMD)			
Temperature	°C	1995-2015	Monthly
Salinity	psu	1995-2015	Monthly
Phosphate	mmol PO_3 m^{-3}	1995-2015	Monthly
Nitrate	mmol NO_3 m^{-3}	1995-2015	Monthly
Silicate	mmol SiOH m^{-3}	1995-2015	Monthly
Chlorophyll-a	mg Chla m^{-3}	1995-2015	Monthly

Table 7.1: Summary of atmospheric forcing fields and observational datasets, reporting reference units, temporal coverage and frequency of data.

7.3 Results

BPC-RETURN and NO-RM experiments comparison

The cross comparison of the seasonal vertical profiles obtained in BPC-RETURN and NO-BPC experiments with the observational data for phosphate, nitrate, silicate, and chlorophyll-a (Figure 7.3) highlights the substantial improvement achieved by the inclusion of BPC processes in the model. The seasonal variability of the inorganic nutrients is well reproduced by the BPC-RETURN experiment, while in the NO-BPC experiment the nutrients content has very small values at all seasons (Figure 7.3 A-B-D). Regard-

Benthic initialisation of standard variables and Parameters			
Variable	**Value**	**Units**	**Description**
Q6c0	4800.0	mg C m^{-2}	Particulate organic Carbon in Sediment
Q1c0	20.9976	mg C m^{-2}	Labile organic Matter in Sediment
burvel R6	0.5	m d^{-1}	Burial Velocity for detritus
burvel PI	0.1	m d^{-1}	Burial Velocity for plankton
Remin Q1	0.01	d^{-1}	Remineralization rate of DOM
Remin Q6	0.005	d^{-1}	Remineralization rate of POM

Table 7.2: Summary of data and parameters used in the BPC sub-model. Note that the other constituents of sediment organic matter (Q6, Q1) were initialized from the carbon content using Redfield ratios.

ing chlorophyll, the winter profiles of the two experiments (Figure 7.3C) coincide despite of the simulated differences in the nutrients supply. This fact demonstrates that the winter chlorophyll dynamic is mainly driven by physical conditions and the model error for the chlorophyll remains fairly unaltered.

As for the previous test cases, the seasonal normalized mean bias (NMB) was computed for each variables with the purpose to objectively compare the two numerical experiments (Figure 7.4).

Overall, both experiments show nagative biases for all variables (with the exception of nutrients in autumn), but using the BPC sub-model a huge improvement in simulating biogeochemical dynamics is achieved. The comparison of silicate autumn profiles (Figure 7.3D) and the relative NMB plot (Figure 7.4D) shows that the NMB is affected by the compensation between the shallow underestimation and the deep layers overestimation. Besides the useful insights on model skill in reproducing the seasonal vertical

profiles provided by the bias analysis, a more in-depth evaluation of the pelagic response to the selected parameterization was carried out in Chapter 8.1 to better evaluate the consistence of the adopted remineralization and burial parameters and their potential influence on the positive bias obtained in deeper layers.

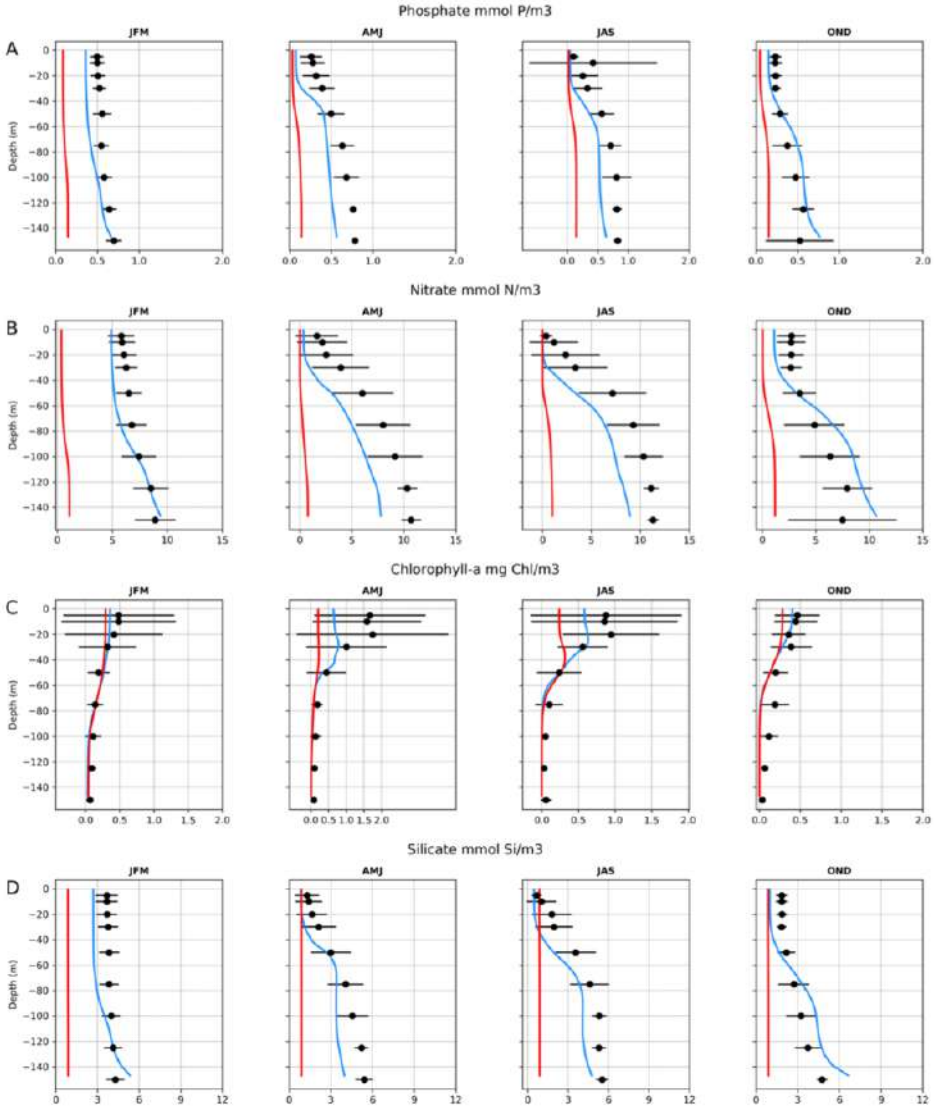

Figure 7.3: Comparison between NO-RM (red) and BPC-RETURN (blue) simulated seasonal mean climatological profiles for (A) Phosphate, (B) Nitrate, (C) Chlorophyll-a, and (D) Silicate climatological seasonal profiles. Black dots indicate observations seasonal average and the horizontal bars their standard deviation. Abbreviations: JFM=winter, AMJ=spring, JAS=summer, OND=autumn.

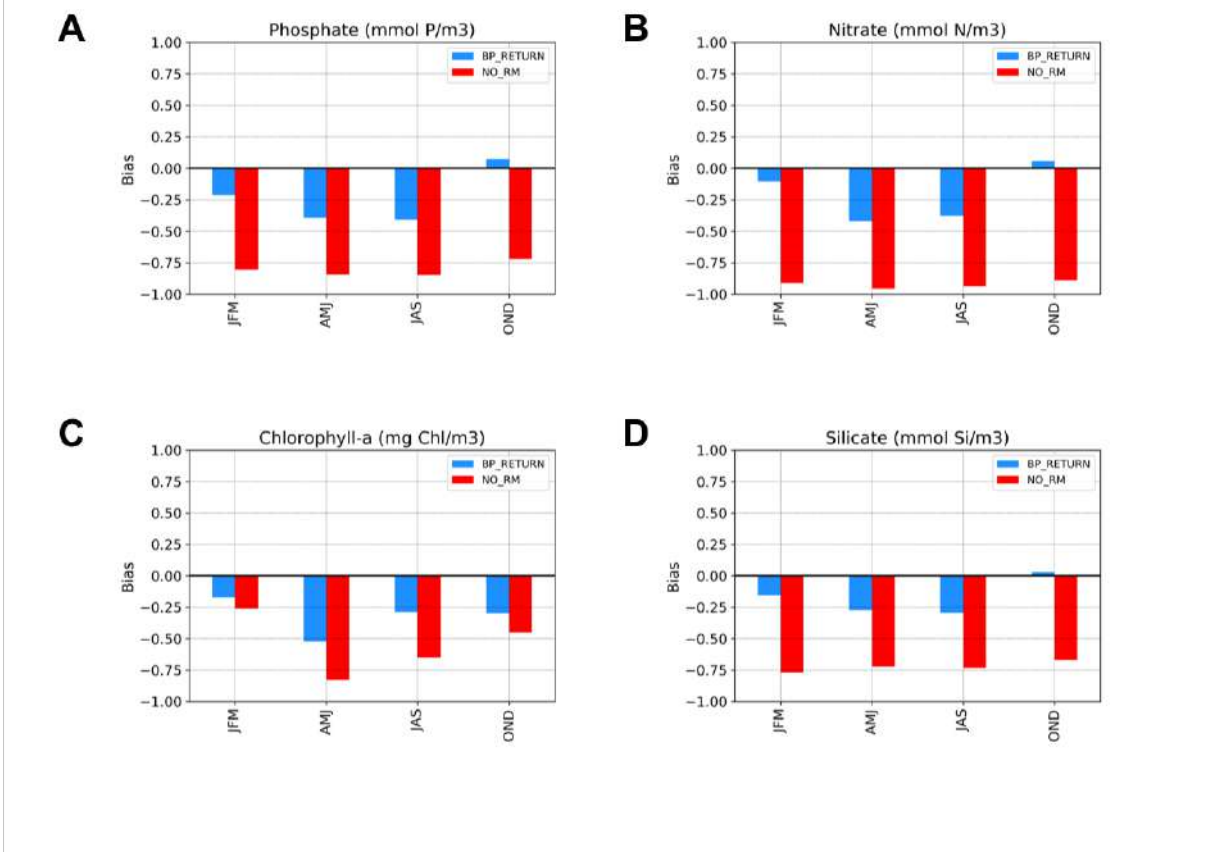

Figure 7.4: Seasonal normalized mean bias comparison between the the NO-RM (red) and the BPC-RETURN (blue) experiments for (A) Phosphate, (B) Nitrate, (C) Chlorophyll, and (D) Silicate. Abbreviations: JFM=winter, AMJ=spring, JAS=summer, OND=autumn.

Assessment of simulated ecosystem dynamics

The seasonal vertical profiles simulated in the reference BPC-RETURN experiment were in a rather good agreement with available observations (Figure 7.3). In particular, the vertical distribution of inorganic nutrients tightly reflects the observed data and in most of the cases lies within the

data standard deviations, although slightly higher values were obtained at the bottom layers.

Figure 7.5 shows the comparison between the observed monthly climatologies of nutrients and chlorophyll-a and those obtained in the BPC-RETURN experiment. The shallow (0-40m) nutrients climatologies is always well reproduced, with a nutrient depletion slightly accentuated in the experiment compared to the observations. Conversely, the nutrients regeneration occurring from October to December likely determines the less satisfactory agreement. The overestimation occurring in autumn between 40 and 150m may be attributable to (a) higher remineralization rates and (b) the uncertainty in the density structure imposed through the restore procedure of temperature and salinity, since December fields were inferred to fill the gaps in monitoring data. In winter and autumn seasons, the phytoplankton dynamics are clearly constrained by the limited availability of solar radiation rather than inorganic nutrients. Conversely, phytoplankton bloom occurring in April is well represented, reflecting the temperature increase and the high nutrient content capable of sustaining the primary production. This allows to argue that the benthic submodel signal is still affecting the surface, regardless of the high bottom depth. From Figure 7.6 it can be noticed that after only ~ 2 years the organic matter in the sediments, even showing a certain degree of seasonality, remains stable around an averaged concentration of 7000 mg C m^{-2}.

In Figure 7.7 is represented the spatio-temporal evolution for three phytoplankton species, namely diatoms, flagellates and picophytoplankton, while large phytoplankton (not shown) suddenly disappears at the beginning of the experiment without recovering. Diatoms activity is the main responsible for the first peak in the chlorophyll occurring at the surface levels around

April, with a deeper chlorophyll signal that is due to the presence of both diatoms and picophytoplankton. The September bloom is instead dominated by flagellates and picophytoplankton.

Similarly to previous sites, direct observations on mesozooplankton and microzooplankton were not found. Nevertheless, from Figure 7.8 a presumably correct representation of zooplankton dynamics can be qualitatively inferred as the temporal and spatial distribution of the predators is in agreement with their preys (following the imposed predator–prey food matrix summarized in Appendix A.5).

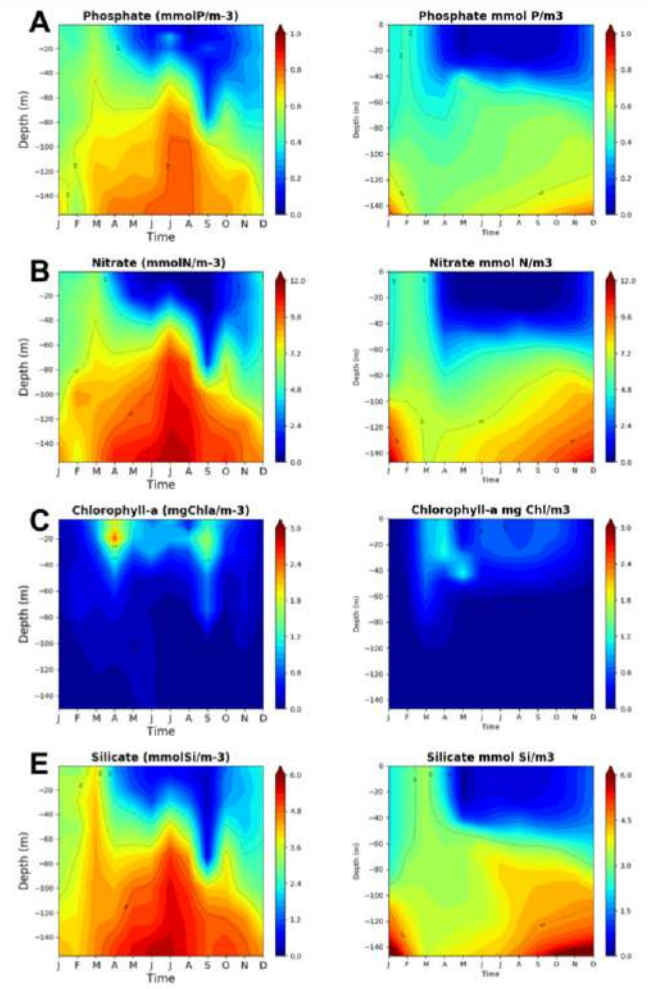

Figure 7.5: Monthly climatological Howmøller plots of observed data (left panel) and BPC-RETURN experiment outcomes (right panel) for (A) Phosphate, (B) Nitrate, (C) Chlorophyll and (D) Silicate. Depth on the Y-axis, months on the X-axis.

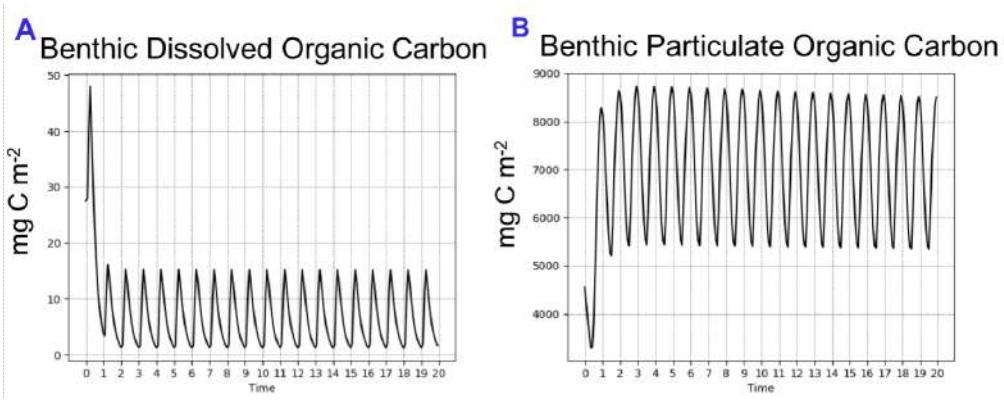

Figure 7.6: Time series of the simulated benthic (A) Dissolved and (B) Particulate Organic Carbon.

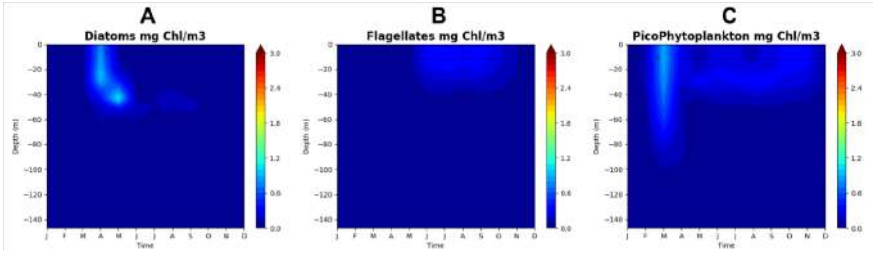

Figure 7.7: Monthly climatologies of BPC-RETURN experiment results for the Phytoplankton component: (A) Diatoms, (B) Flagellates and (C) Picophytoplankton. Depth on the Y-axis, months on the X-axis.

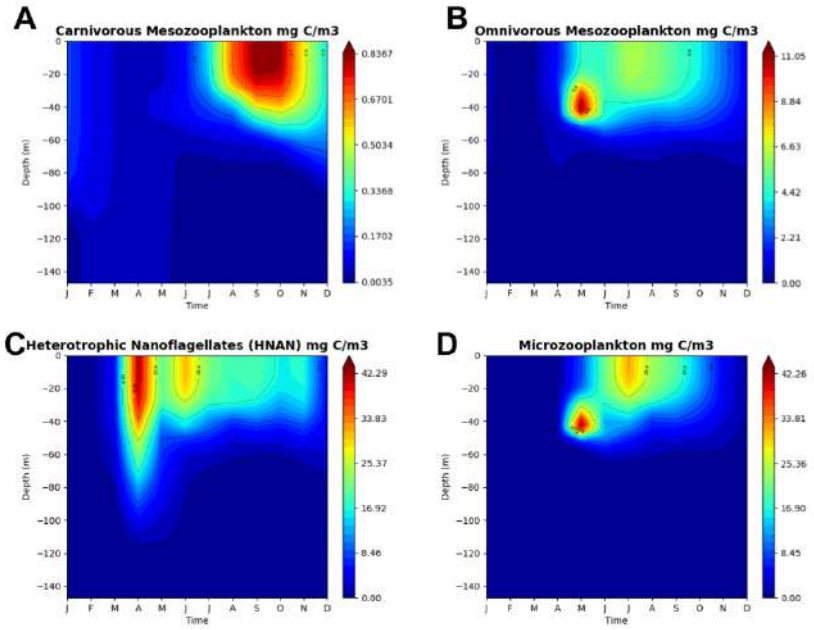

Figure 7.8: Monthly climatologies of BPC-RETURN experiment results for the Zooplankton component: (A) Carnivorous Mesozooplankton, (B) Omnivorous Mesozooplankton, (C) Heterotrophic nanoflagellates and (D) Microzooplankton. Depth on the Y-axis, months on the X-axis.

Chapter 8

Sensitivity analysis

8.1 Background

Sensitivity analysis (hereafter SA) is a procedure used in numerical modelling to investigate the variation in the output of a numerical model depending on the variations of the input [109].

It allows to achieve the second objective of this thesis (Section 2.3), namely to evaluate the skill of the model in BPC fluxes reproduction as function of the parameterization adopted.

Here the statistical information obtained from the SA is used to (a) identify the 'best experiment' starting from the first guess experiment described in Chapters 5.1, 6.1 and 7.1 (b) investigate the role of benthic remineralization and organic matter deposition in determining the nutrient seasonal cycles and the chlorophyll dynamic in each site, (c) carry out a comparative analysis between the best BPC configurations found in each site and their relative environmental (e.g. water column depth) and ecological (e.g. net primary production) characteristics.

In fact as emphasized in literature [110, 111, 112, 113], the SA is a powerful procedure to investigate the skill of the models (in this case the BPC sub-model) and to identify the best (BP) parameter configuration.

According to [114], *parameters in marine ecosystem models are generally poorly known quantities. This is mainly due to the fact that the model state variables are highly integrated pools that comprise different species, which are affected differently by biotic and abiotic changes in their environment. The model parameters should represent the integrated behavior of this heterogenic mixture of species. Furthermore, the proportions of the different species contributing to the species pool may change in time as ecosystems respond to changes in environmental conditions.*

In this framework, benthic nutrient remineralization and release (representing the integrated response of the sediment to water physical and biogeochemical fluxes) and organic matter deposition (enclosing the integrated behavior of the biotic and abiotic exchanges between the bottom water column and the sediment interface) should be considered as the poorly known quantities strongly affected by the changes in the seasonal and environmental conditions.

Finally, *the marine ecosystem models should be capable of describing all different regions of the oceans. In this framework, to be considered robust a model should be equally reliable in different biogeochemical provinces and at different environmental dynamics* [114].

The robustness of the BPC sub-model has been measured assessing the model reliability in reproducing different ecological and physical dynamics and evaluating the relationships between the three chosen regions as a good example of the various conditions found in the global coastal ocean.

8.2 Methods

The SA has been carried out applying the same procedure for all the three sites described in the previous chapters. The starting point is the BPC-RETURN experiment (described Section 4.2), that was identified as the SA first guess. From the first guess, a set of numerical experiments has been performed by varying the remineralization rate and the burial velocity parameters. These varied quantities are expressed in percentage with respect to the 'first guess experiment'. Table 8.1 summarizes the BPC- submodel parameterization adopted for the first guess, and in Table 8.2 the burial and remineralization ranges of sensitivity analysis for each station.

Site	Burvel $[m/d]$	Remin Q6[cnp] $[d^{-1}]$	Remin Q6[s] $[d^{-1}]$
St Helena Bay	1.0	0.0025	0.0015
Svinøy Fyr	1.0	0.005	0.005
MA21	0.5	0.0025	0.0025

Table 8.1: Summary of the First Guess (BPC-RETURN) experiments parameterization for the three sites. Q6 cnps refers to benthic particulate matter of carbon, nitrate, phosphate and silicate.

Site	Burvel min	Burvel max	Remin min	Remin max
St Helena Bay	-40%	+20%	-30%	+30%
Svinoy Fyr	-100%	+50%	-30%	+60%
MA21	-30%	+30%	-30%	+30%

Table 8.2: Sensitivity test ranges for the three sites. Maximum and Minimum value of burial velocity and remineralization rate expressed as percentage with respect to the first guess (BPC-RETURN) experiment.

The initial parameters and the percentage ranges are not equal in all the stations (see Tables 8.1 and 8.2) . The benthic first guess parameters have been chosen with the few (qualitative) information available from literature as described in the Chapters 5.1, 6.1 and 7.1. The SA ranges have been chosen centering the percentages on the control experiment, varying both the burial velocity and the remineralization parameters ranges between -20% and$+20\%$. Finally, these ranges have been modified after some a posteriori considerations. Assuming that the skill of the model, evaluated in terms of Root Mean Square Error, has a Gaussian distribution centered on the best experiment, the burial/remineralization ranges have been extended until reaching the Gaussian apex.

In order to define the 'best experiment' with respect to the first guess, a statistical analysis has been performed comparing the simulated mean annual profiles (obtained averaging the second half of the simulated period) with in situ observations.

To evaluate the model behaviour in reproducing the BPC fluxes at contrasting sites, *qualitative graphical analysis* [111] and statistical analysis have been combined.

In Particular, for all the sites, was performed:

1. Normalized Root-Mean-Square Deviation Analysis
2. Taylor summary diagrams analysis
3. Target summary diagrams analysis

The Graphical analysis (by means the averaged seasonal vertical profiles) was finally chosen to interpret the results obtained from the applied statistical procedure and to highlight the related eventual limitations.

Normalized Root-Mean-Square Deviation Analysis

The Normalized Root-Mean-Square Deviation analysis (NRMSE or NRMSD) was carried out in order to get general information about the behaviour of the model with respect to the benthic parameters (burial velocity and remineralization rate). The NRMSE has been computed normalizing the Root Mean Square Error (RMSE) with respect to the mean value of the observations and reporting the model error as percentage, where low NRMSE values indicate less residual error [115, 116]. NMRSE is defined as:

$$NMRSE = \sqrt{\frac{\sum_{n=1}^{N}(m_n - r_n)^2}{\sum_{n=1}^{N}(r^2)}} \tag{8.1}$$

where m_n is the nth simulated (model) data, r_n is the nth observation and N the number of data (references data). Although different metrics have been proposed in literature [117] for numerical model skill assessment, the NRMSE remains the dominant metric in order to investigate statistical results concerning the parameter space [116].

Taylor Analysis and Target Analysis

The Taylor and Target diagrams statistically summarize the degree of correspondence between the simulated and reference fields, accounting for more than one statistical operator at a time.

The normalized Taylor diagram is displayed in polar coordinates for pattern comparison between reference and experiment(s) in terms of standard deviation, correlation, and unbiased Root Mean Square Difference [110].

This *statistical metrics* [110] at the basis of the Taylor diagrams are:

$$\sigma* = \frac{\sigma_m}{\sigma_r} = \frac{\sqrt{\frac{1}{N}\sum_{n=1}^{N}(m_n - \overline{m})^2}}{\sqrt{\frac{1}{N}\sum_{n=1}^{N}(r_n - \overline{r})^2}} \tag{8.2}$$

$$R = \frac{\frac{1}{N}\sum_{n=1}^{N}(m_n - \overline{m}) - (r_n - \overline{r})^2}{\sigma_m \sigma_r} \tag{8.3}$$

$$RMSD' = \left(\frac{1}{N}\sum_{n=1}^{N}[(m_n - \overline{m}) - (r_n - \overline{r})]^2\right)^{0.5} \tag{8.4}$$

where $\sigma*$ is the normalized standard deviation, that provides information about the relation of amplitudes between the model (m) and the reference data (r), R is the correlation that gives information on the potential shift (phase) between the vertical profiles of m and r and $RMSD$' is the unbiased Root Mean Square Difference that may be conceptualized as an overall measure of the agreement between the amplitude and phase of the two temporal patterns [110]. The overbar indicates the mean of the considered field.

Standardizing the $RMSD$' (also considered in the Target diagrams) and defining the relationships between the above mentioned pattern statistics (as in [110]), the $RMSD$' can be rewritten as:

$$RMSD' = \sqrt{1 + \sigma *^2 - 2\sigma * R} \tag{8.5}$$

where it is clear that even containing amplitude and phase information, it is not possible to determine how much the error is due to the amplitude or phase error [112]. The Taylor diagram does not provide information on the bias.

In the Target diagram proposed by [110] the analysis is performed decomposing the RMSD in its orthogonal Bias (B) and $RMSD$' components:

$$RMSD^2 = B^2 + RMSD'^2 \tag{8.6}$$

where B is:

$$B = \frac{\overline{m} - \overline{r}}{\sigma_r} \tag{8.7}$$

The model skill is here evaluated in a simple Cartesian coordinate system, gauging the distance between the origin and the experiment(s) (which is the total RMSD). The main strength of the Target diagrams is that the represented pattern statistics yield an information about their individual contribution to the total RMSE, also accounting for the amplitude and phase of the error (embedded in Eq. 8.4).

Given the high number of the experiments shown in the Taylor and Target diagrams for the three implemented sites, the summary diagrams results were shown by grouping the sensitivity experiments in remineralization or burial percentage groups. Thus, for this analysis, the identification of the best experiment is done at the burial/remineralization group level.

Graphical Analysis

A discussion and analysis of the behaviour of the statistical procedure employed for the evaluation of the model's skill is finally presented to evaluate the improvements obtained (if any) in terms of error from the first guess to the best guess experiment on the base of line plots comparisons that can be easily used to qualitatively interpret the results obtained from all the adopted statistical metrics [111].

8.3 Sensitivity Analysis Results and Discussion

To pursue the aforementioned purpose of determining the best experiment, statistical operators were applied to all the variables listed in Table

4.1 and shown in Appendix A.2. Moreover the intercomparison between the best BPC parameterization found in the three implemented sites and their environmental and ecological characteristics has been executed considering phosphate, nitrate and chlorophyll. Indeed, these are the variables which are common to all the test cases.

Experimental SA scheme

The SA matrix of the experiment for SHB and SFyr test cases has been enlarged in order to reach the minimum NRMSE condition.

St Helena Bay has been the first test of the sensitivity analysis, because of the richness of the dataset with respect to the SFyr and the MA21 implemented sites. 91 simulations have been performed following the scheme of parameter variations schematized in Figure 8.1.

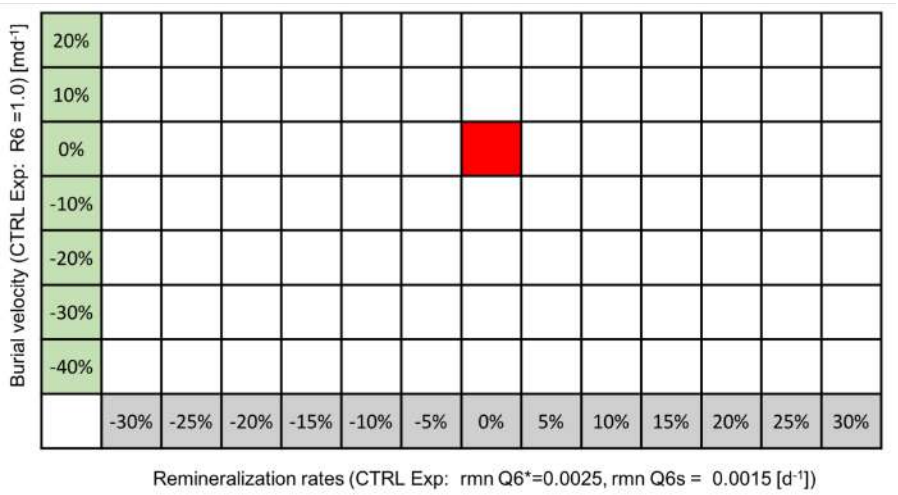

Figure 8.1: **St. Helena Bay** site sensitivity test scheme. The experiments are expressed as varied burial and remineralization parameters percentages with respect to the first guest experiment (Red square).

The experiment matrix shown in Figure 8.2 refers to the 160 experiments

carried out for the **Svinøy Fyr** site. Here, the percentage step (10%) has been changed with respect to the SHB station (5%) on the light of the fact that small variations of the benthic parameters does not excessively affect the model behaviour (not shown). The extension of both the BPC parameters ranges was performed based on the NRMSE analysis.

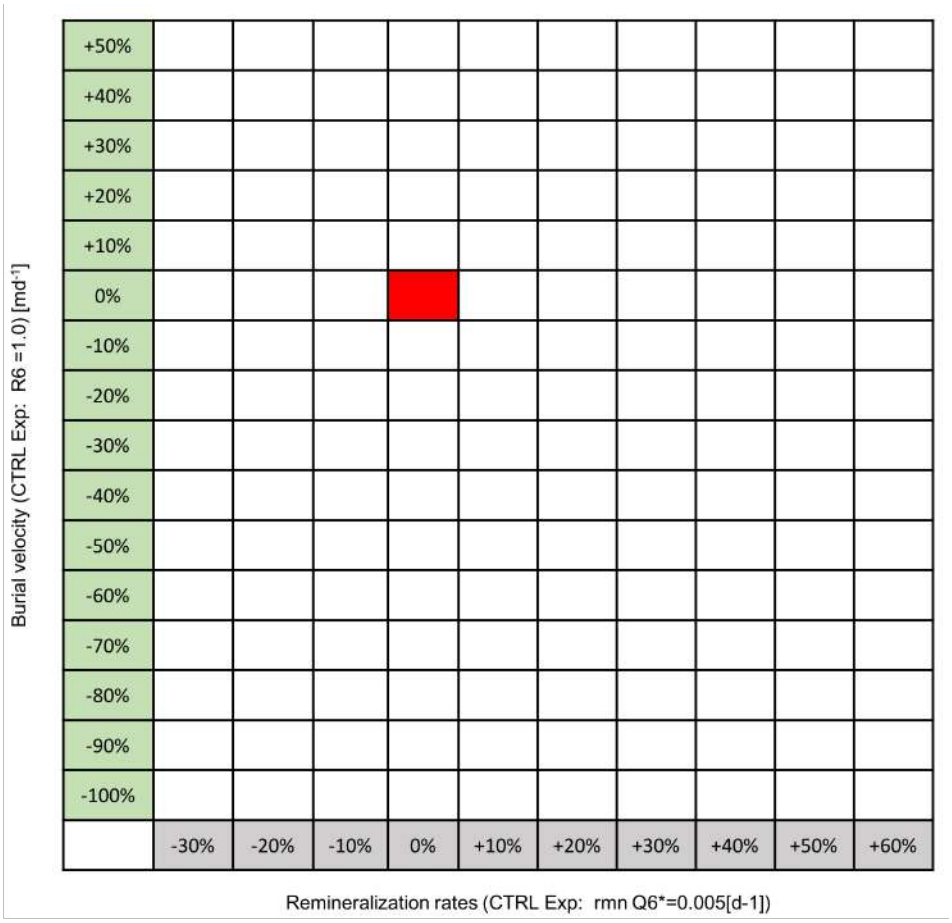

Figure 8.2: **Svinøy Fyr** site sensitivity test scheme. The experiments are expressed in varied burial and remineralization parameters percentage with respect to the first guest experiment (Red square).

In the **MA21** station the original matrix of the experiment has been maintained, limiting the sensitivity analysis to few experiments with respect to the SHB and SFyr sites. Indeed, the validation dataset has been considered not particularly suitable for statistical analysis, having a seasonal resolution (see Table 5.1) and being rather low in number (2-4 nutrient observation for season). The 49 experiments matrix is shown in Figure 8.3.

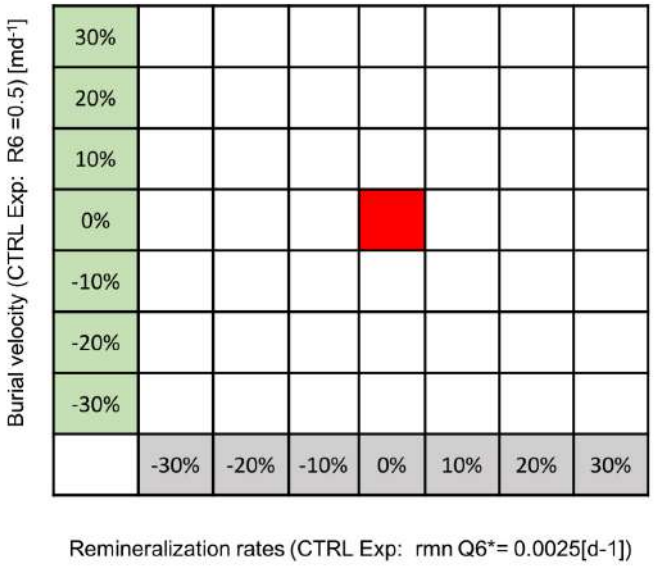

Figure 8.3: **MA21** site sensitivity test scheme. The experiments are expressed in varied burial and remineralization parameters percentage with respect to the first guest experiment (Red square).

Normalized Root-Mean-Square Deviation

The comparison between the NRMSE computed with respect to the validation data gives a flavour about the behaviour of the model with respect to decreasing/increasing burial and remineralization parameters. The results of the NRMSE analysis for each variable and site are shown in Appendix

A.2. The intercomparison between the three contrasting sites is carried out with respect to the phosphate, nitrate and chlorophyll in situ observations.

The total NRMSE, obtained averaging the contribution of the three SA variables (phosphate, nitrate and chlorophyll), has been computed and analyzed. Despite the simplicity of the analysis this *pattern statistic* [110] allows some useful considerations.

Table 8.3 lists the maximum and minimum averaged total NRMSE and the error difference between them. The 'minimum error experiment' is here considered the 'Best Experiment' with respect to the NRMSE analysis, while the 'worst experiment' is the experiment characterized by the highest NRMSE.

In spite of its reduced number of experiments, the shallowest implemented site, the MA21, appears the most sensitive site to the BPC submodel parameterization, while the deepest station, the SFyr one, is less affected by the BPC parameters variations. It is recalled that the maximum spread of the NRMSE obtained in the SFyr station (2.57%) is resulting from a wider SA matrix.

Test Case	Name Worst Exp.	Error	Name Best Exp.	Error	ErrorDiff
MA21	B +30% R -30%	49.78%	B -30% R +30%	44.68%	5.10%
SHB	B -40% R +30%	36.66%	B -40% R -30%	31.90%	4.76%
SFyr	B +50% R -30%	49.38%	B -90% R +60%	46.81%	2.57%

Table 8.3: Summary of the averaged total RMSE computed over the phosphate, nitrate and chlorophyll. Name of the worst and best experiments (%), their relative errors in percentage, and difference in error between the worst and best test. Site Abbreviation: MA21= Gulf of Trieste, SHB = St. Helena Bay and SFyr = Svinøy Fyr.

For each test case, the 'Best Experiment' has the following remineralization and burial values:

- SHB, remineralization: 0.00175 d^{-1}, Burial: 0.60 m/d
- MA21, remineralization: 0.00325 d^{-1}, Burial: 0.35 m/d
- SFyr, remineralization: 0.008 d^{-1}, Burial: 0.10 m/d

In terms of remineralization rate ($days^{-1}$), the SFyr station is better represented by higher parameter values indicating a more active benthic activity, while the MA21 and SHB have less active BPC conditions. Concerning the burial velocity, the MA21 and SHB best experiments show higher values with respect to SFyr station.

As shown in equation 3.52, the temporal rate of change of the benthic organic matter depends on the BPC parameters and on the concentration of particulate organic matter in the sediment and at the sediment-water interface. Table 8.4 lists the averaged benthic (in column 1-2) and pelagic (in column 3) fluxes expressed in terms of carbon for the burial processes representative of the biomass sequestered by the sediments, while the remineralization processes are given in nitrogen and phosphorus in order to highlight the regeneration of limiting nutrients by the sediments. Regardless of the chosen BPC parameter values, the remineralization flow is higher in the SHB and MA21 sites, simulating a richer sediment, with respect to the deeper station of SFyr. Moreover, the sediment inflow is larger in MA21 and SFyr. As mentioned in Chapter 5.1, the prolonged cooling and mixing of the entire water column occurring in the Gulf of Trieste in winter and autumn can reasonably increase the sinking of the particulate organic matter. The spring and summer deep biomass peak can also enhance the burial flux

(see Chapter 5.1). Despite the higher burial velocity parameter (0.6 m/d), SHB exhibits the minimal burial flux (Table 8.4). This clearly indicates the lower sedimentation flux of particulate detritus and phytoplankton. SHB is a site characterized by upwelling conditions here idealised as described in Chapter 6.1. The minimal burial flux can be likely be attributed to pelagic remineralization.

Test Case	Remin * Q6n	Remin * Q6p	R6c Buried
SHB	1.027	0.068	-0.0021
MA21	0.910	0.050	-0.1344
SFyr	0.336	0.016	-0.0636

Table 8.4: Summary of the averaged total Benthic (column Remin * Q6n and column Remin * Q6p) and Pelagic (column R6c Buried) fluxes. The benthic fluxes are expressed in mmol N-P/m^2day and the pelagic fluxes in mg C/m^2 day. Site Abbreviation: MA21= Gulf of Trieste, SHB = St. Helena Bay and SFyr = Svinøy Fyr.

The intercomparison between the maximum and minimum NRMSE differences (8.3, column ErrorDiff) has been evaluated with respect to the depth of the three sites. As indicated by Figure 8.4, a certain degree of dependency between the station depth and the benthic pelagic intensity of the fluxes can be observed suggesting a decreasing sensitivity to the benthic-pelagic interface parametrization with depth in agreement with [19].

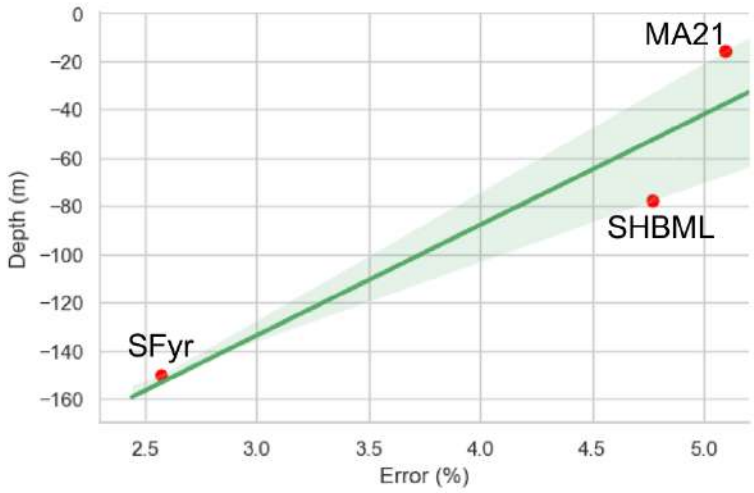

Figure 8.4: Intercomparison between the Depth (Y-axes) and the error differences between the maximum and the minimum NRMSE (X-axes) for the three implemented stations see Table 8.3. Green line refers to the regression line, the shaded area to the confidence interval (0.5) for the regression estimate.

Tables 8.5, 8.6 and 8.7 list the phosphate, nitrate and chlorophyll NRMSE. As previously observed, the effect of upwelling and the subsequent temporal extension of the thermocline does not allow to obtain chlorophyll improvements (in terms of NRMSE) even if phosphate and nitrate errors are considerably reduced. Contrarily in the the MA21 and SFyr sites, prolonged mixed and homogeneous water column conditions allow chlorophyll to be more affected by the BPC parameterization.

SHB	Name Worst Exp.	Error	Name Best Exp.	Error	ErrorDiff
Phosphate	B -40% R +30%	22.53%	B -30% R -30%	17.97%	4.56%
Nitrate	B -40% R +30%	30.29%	B -10% R -25%	21.0%	9.29%
Chlorophyll	B -40% R +30%	57.18%	B +20% R -30%	56.48%	0.70%

Table 8.5: Summary of the RMSE for the all the variables. The name of the worst and best experiments and relative errors in percentage, and difference in error between the two experiments.

SFyr	Name Worst Exp.	Error	Name Best Exp.	Error	ErrorDiff
Phosphate	B +50% R -30%	36.88%	B -90% R +60%	35.31%	1.57%
Nitrate	B +50% R -30%	36.34%	B -90% R +60%	34.09%	2.25%
Chlorophyll	B +50% R -30%	74.93%	B -90% R +60%	71.03%	3.90%

Table 8.6: Summary of the NRMSE for the all the variables. The name of the worst and best experiments and relative errors in percentage, and difference in error between the two experiments.

MA21	Name Worst Exp.	Error	Name Best Exp.	Error	ErrorDiff
Phosphate	B -30% R +30%	59.72%	B -30% R -10%	58.0%	1.72%
Nitrate	B +30% R -30%	45.49%	B -30% R +30%	43.43%	2.06%
Chlorophyll	B +30% R -30%	44.26%	B -30% R +30%	30.09%	14.17%

Table 8.7: Summary of the RRMSE for the all the variables. The name of the worst and best experiments and relative errors in percentage, and difference in error between the two experiments.

Summary diagrams analysis

As for the NRMSE analysis, the summary diagrams contribute to identify the 'Best Experiment'. It assess the skill of the model and the sensibility of the pelagic variables to the adopted BPC parameterization. In this section,

diagrams for the variables phosphate, nitrate and chlorophyll are shown since data for the variables were available for all sites. While, supplementary comparisons to additional data available at individual sites are provided in Appendix A.2. To make the diagrams clearer, the experiments were grouped into remineralization groups that had same remineralization values and different burial values. This grouping scheme was chosen on the basis that the error is more sensitive to remineralization than to the burial term.

Figures 8.5, 8.6 and 8.7 show the Taylor (left panels) and Target (right panels) diagrams performed in SHB, SFyr and MA21 sites respectively.

From the Taylor analysis less information can be retrieved, since in the three sites the cloud of the experiments is condensed for all the test cases. Nevertheless, it can be noticed that in each site, correlation is generally constant and high (with the exception of phosphate and nitrate for the MA21 test case).

In the three Taylor diagrams of **SHB** (Figure 8.5 left panel), the '−30% remineralization' group (in blue) is characterized by the lowest unbiased RMSD, providing the closest fit to the data. For chlorophyll and phosphate, the results are in agreement with the 'Best experiment' defined in the previous NRMSE analysis while it is slightly different (5%) for the nitrate. The nearly constant values of correlation and a higher standard deviation suggest that the sensitivity analysis averaged vertical profiles share similar phase and varying amplitude, returning an unbiased RMSE mainly amplitude-driven, for the phosphate and, even if to a lesser extent, for the nitrate. Contrarily, the chlorophyll cloud of experiments has a better amplitude agreement.

Investigating the relationship between the bias and the unbiased RMSE, the Target diagrams in Figure 8.5 (right panel) confirm the results obtained in the NRMSD and Taylor analysis. From the Target diagram it can be

observed how the inorganic nutrient total NRMSE is mainly determined by the bias, while in the chlorophyll the bias and unbiased NRMSE equally contribute to the total NRMSE. The comparison among the results, in terms of Best Experiment, obtained using the three statistical operators is shown in the devoted SHB Section of Table 8.8.

In the **SFyr** test case, the cluster of the model points are extremely grouped in all the summary diagrams (Figure 8.6). From the Taylor diagram of the chlorophyll (Figure 8.6 bottom-left panel) it can be noticed that the best experiment belong to the 'remineralization +60%' group, confirming the previous analysis. The same results can be observed from the Target (right panel) diagram where the total RMSE is equally determined by bias and unbiased RMSE variations. Instead, the Taylor diagrams of the inorganic nutrients were characterized by a good amplitude ($\sigma \sim 1$). This makes the unbiased NRMSD mainly phase-driven (Figure 8.6 top and middle-left panel). In both cases the best experiment group is not enough clear, being in between the SA percentage ranges. The enlargement of these two diagrams is not shown because with this qualitative analysis the results of the NRMSE are already not confirmed. In the nutrients Target diagrams (right panel) the unbiased RMSD is constant for the nitrate and fairly constant for the phosphate cloud of experiments, determining a bias-driven total RMSD. The comparison among the results, in terms of Best Experiment, obtained using the three statistical operators is shown in the devoted SFyr Section of Table 8.8.

In the **MA21**, chlorophyll is the only variable correlated with the reference field. This is likely due to the already described dataset limitations (nutrients profiles have 2-3 averaged measurement for season). The chlorophyll Taylor diagram (Figure 8.7 bottom left) shows that the lower reminer-

alization groups (around -20%) are characterized by the lowest unbiased RMSD, while the Target diagram (right panel) demonstrates that the cloud of experiments is highly biased (> 1). Phosphate and nitrate Taylor diagram model points (Figure 8.7 top and middle left) have respectively negative and weakly positive correlation and extremely low values of standard deviation. This statistical features indicate a remarkable difference in phase and amplitude of the SA mean vertical profiles with respect to the few observations. Having highest but low varying values of unbiased RMSE (with respect to the bias), the phosphate total RMSD is particularly affected by bias, because the simulations span over a more large range (right panel). The comparison among the results, in terms of Best Experiment, obtained using the three statistical operators is shown in the devoted MA21 Section of Table 8.8.

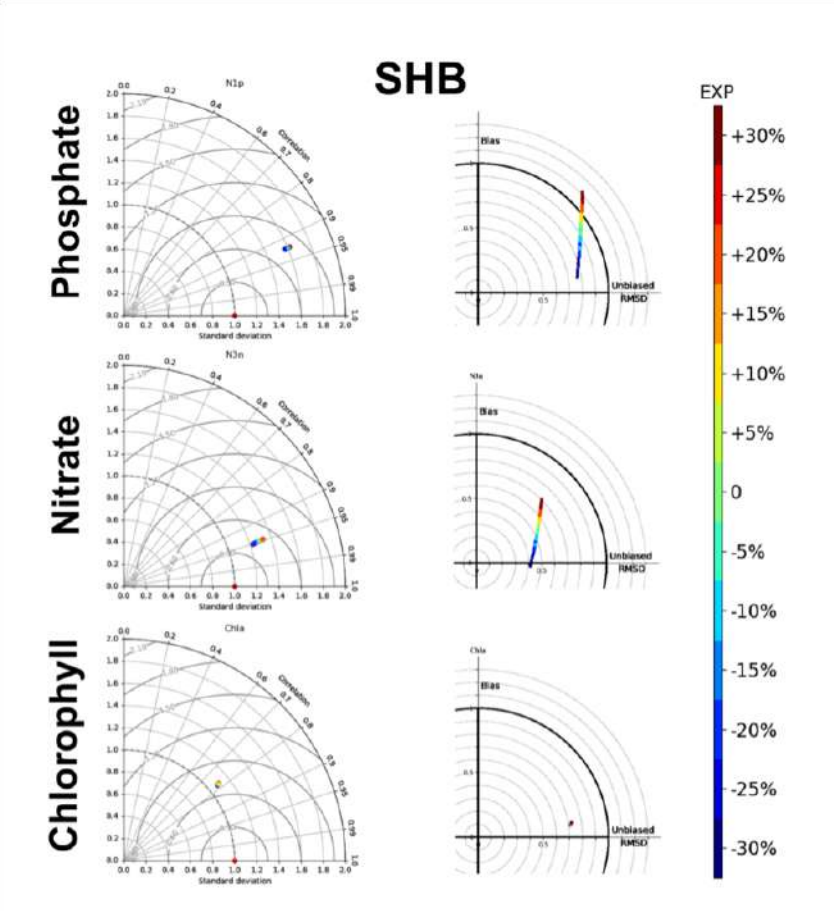

Figure 8.5: Taylor (left panel) and target diagram (right panel) of the SA for phosphate, nitrate and chlorophyll (top, middle and bottom respectively). Taylor diagram rendering of the SA tests with respect to the data (ideal match represented by a red dot). The radial distance to the origin is proportional to the normalized standard deviation (σ^*), and the angular position corresponds to the linear correlation (R). The distance between the reference field and the test point is proportional to the unbiased RMSD.

Normalized target diagram for test and reference comparison (bottom panel). The Y-axis corresponds to the bias, the X-axis corresponds to the unbiased RMSD. The distance of each point to the origin is the RMSE.

Experiments were grouped in remineralization groups.

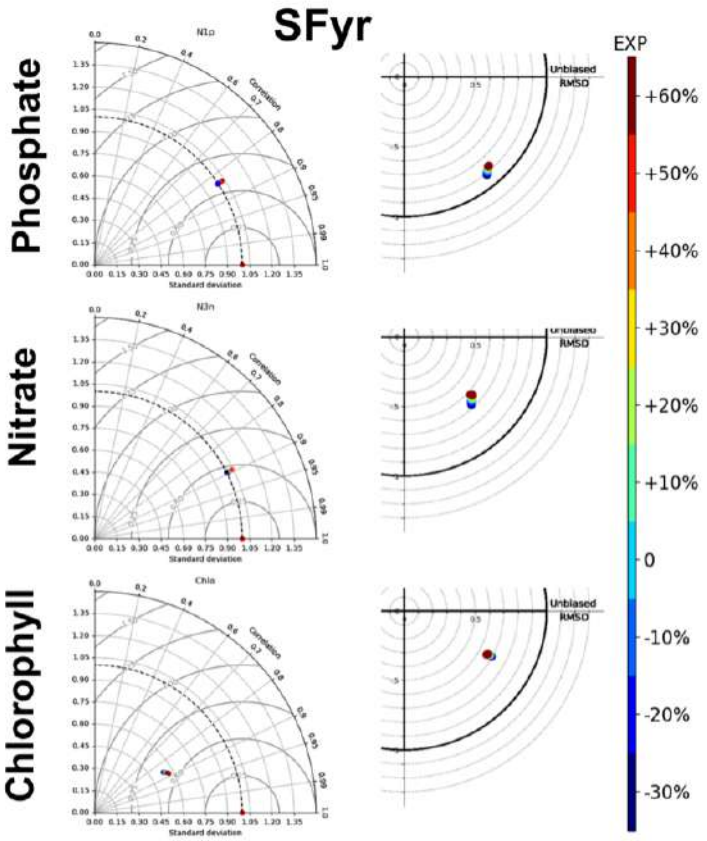

Figure 8.6: Taylor (left panel) and target diagram (right panel) of the SA for phosphate, nitrate and chlorophyll (top, middle and bottom respectively). Taylor diagram rendering of the SA tests with respect to the data (ideal match represented by a red dot). The radial distance to the origin is proportional to the normalized standard deviation (σ^*), and the angular position corresponds to the linear correlation (R). The distance between the reference field and the test point is proportional to the unbiased RMSD.

Normalized target diagram for test and reference comparison (bottom panel). The Y-axis corresponds to the bias, the X-axis corresponds to the unbiased RMSD. The distance of each point to the origin is the RMSE.

Experiments were grouped in remineralization groups.

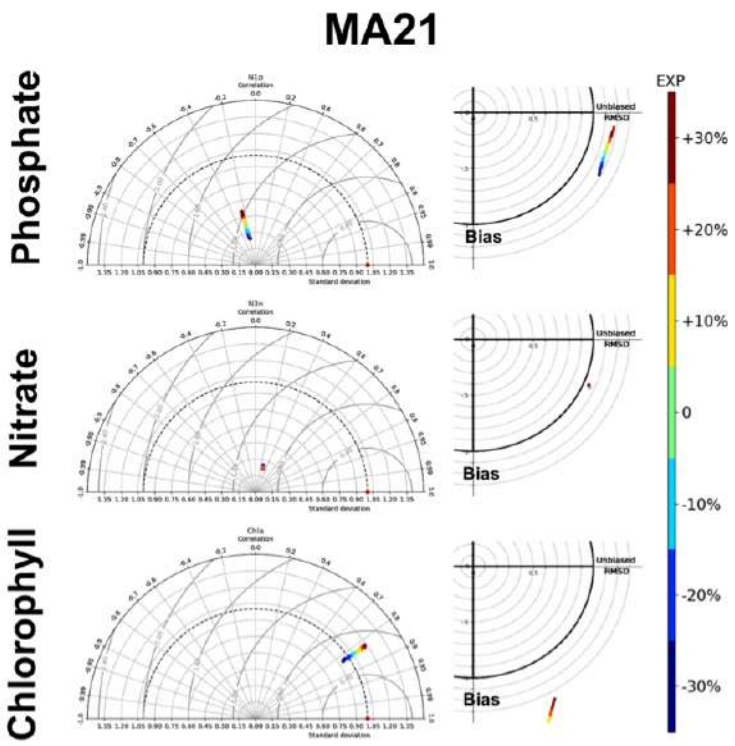

Figure 8.7: Taylor (left panel) and target diagram (right panel) of the SA for phosphate, nitrate and chlorophyll (top, middle and bottom respectively). Taylor diagram rendering of the SA tests with respect to the data (ideal match represented by a red dot). The radial distance to the origin is proportional to the normalized standard deviation (σ^*), and the angular position corresponds to the linear correlation (R). The distance between the reference field and the test point is proportional to the unbiased RMSD.

Normalized target diagram for test and reference comparison (bottom panel). The Y-axis corresponds to the bias, the X-axis corresponds to the unbiased RMSD. The distance of each point to the origin is the RMSE.

Experiments were grouped in remineralization groups.

SHB			
Variable	RMSD	Taylor diagram	Target diagram
Phosphate	B -30% R -30%	R -30%	R -30%
Nitrate	B -10% R -25%	R -30%	R -30%/ R -25%
Chlorophyll	B +20% R -30%	R -30%	R -30%
Avg RMSD	B -40% R -30%	—	—
SFyr			
Variable	RMSD	Taylor diagram	Target diagram
Phosphate	B -90% R +60%	not clear	R +60%
Nitrate	B -90% R +60%	not clear	R +60%
Chlorophyll	B -90% R +60%	R +60%	R +60%
Avg RMSD	B -90% R +60%	—	—
MA21			
Variable	NRMSD	Taylor diagram	Target diagram
Phosphate	B -30% R -10%	R -30%	R -10%
Nitrate	B -30% R +30%	R +30%	R +30%
Chlorophyll	B -30% R +30%	R -30%/R -20%	R +30%
Avg RMSD	B -30% R +30%	—	—

Table 8.8: Summary of the 'Best Experiment' Remineralization and Burial values (in %) characteristic obtained using the Normalized Root-Mean-Square Deviation Analysis (NRMSD), The Taylor and the Target Diagrams. The total averaged NRMSE has been computed only in the NRMSD analysis.

Graphical Analysis

On the basis of what was observed in the three different sites, as regards the statistical analysis performed, the graphical analysis is finally done to qualitatively reject or confirm what the best experiment is.

The need to use qualitative analysis mainly arises from the quality of the observational datasets used to carry out the statistical procedure. In particular, the implemented sites of SHB and SFyr were characterized by a high number of measurements, temporal coverage and data frequency (see Table 6.1 and 7.1) making the SA more reliable with respect to that of the MA21 test case (Table 5.1).

Figure 8.8, 8.9 and 8.10 show the comparison between the best experiment (in red), the first guess (in blue) and the reference field (in black) seasonal climatological profiles for the three test cases.

St. Helena Bay

Going from the first guess to the SA Best test, the inorganic nutrients profiles (Figure 8.8 A-B-D) show a general and slight improvement, especially in the deeper levels of the water column (30-80m), while chlorophyll and oxygen can be considered not sensible to the adopted variations of the remineralization and burial BPC parameters.

Svinøy Fyr

In Svinøy Fyr station the error difference between the best experiment and the first guess is not perceived. Indeed, considering all the variables, the error difference between the first guess and the best experiment in terms of NRMSD is $\sim 1\%$.

MA21

In the shallower implemented station, the MA21, improvements can be observed for the chlorophyll dynamics, while the ammonium seasonal pro-

files match better the observation using the First guess parameters benthic conditions.

Finally, from the graphical analysis of the seasonal vertical profiles, the Best Experiment results obtained with the different pattern statistics (NRMSE and summary diagrams analyses) are successfully confirmed with the exception of the inorganic nutrients of the MA21 area where the mentioned limitations of the used dataset make the improvements not at all clear.

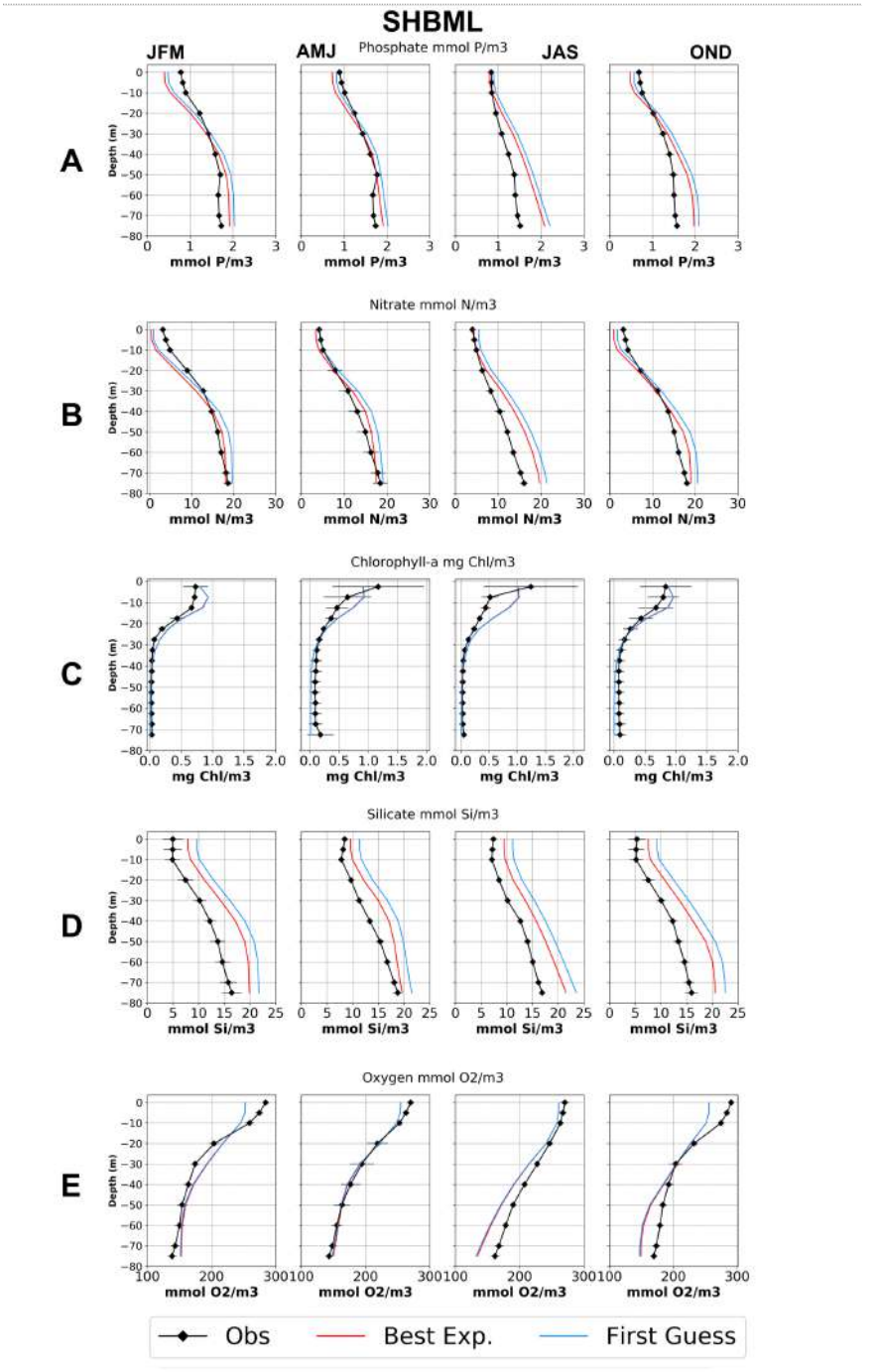

Figure 8.8: St. Helena Bay Seasonal profiles comparison between the first guess (blue), the SA best result (red) and the averaged data (dots) and standard deviation (horizontal bars) (black) for: (A) Phosphate, (B) Nitrate, (C) Chlorophyll, (D) Silicate and (E) Oxygen. Abbreviations: JFM = winter, AMJ=spring, JAS=summer and OND=autumns.

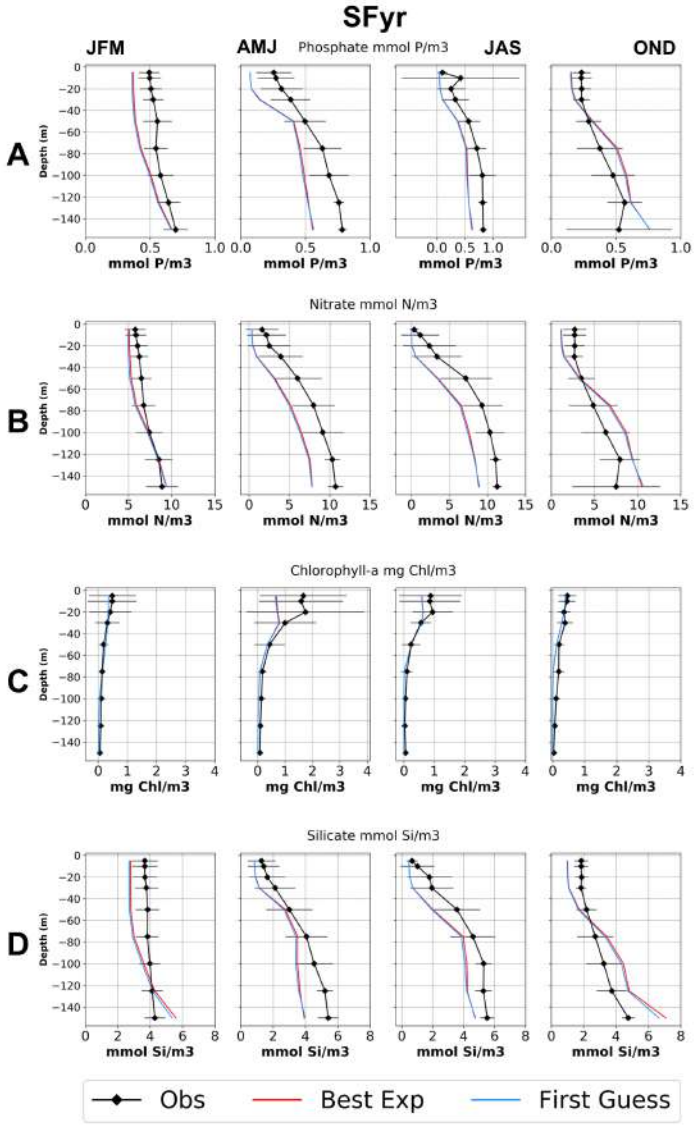

Figure 8.9: Svinøy Fyr seasonal profiles comparison between the first guess (blue), the SA best result (red) and the averaged data (dots) and standard deviation (horizontal bars) (black) for: (A) Phosphate, (B) Nitrate, (C) Chlorophyll and (D) Silicate. Abbreviations: JFM = winter, AMJ=spring, JAS=summer and OND=autumns.

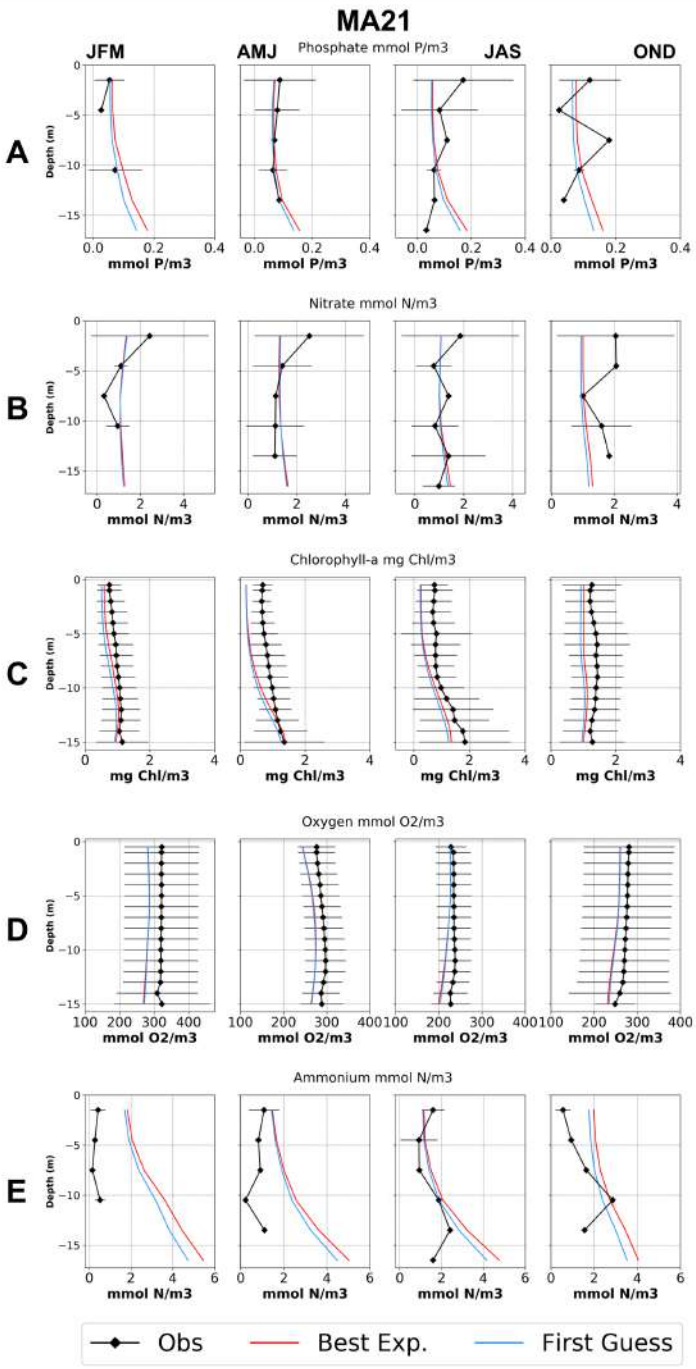

Figure 8.10: Gulf of Trieste seasonal profiles comparison between the first guess (blue), the SA best result (red) and the averaged data (dots) and standard deviation (horizontal bars) (black) for: (A) Phosphate, (B) Nitrate, (C) Chlorophyll, (D) Oxygen and (E) Ammonium. Abbreviations: JFM = winter, AMJ=spring, JAS=summer and OND=autumns.

Chapter 9

Conclusions

The benthic-pelagic dynamic processes were successfully implemented in the coupled physical-biogeochemical NEMO-BFM model and were verified in a one-dimensional modelling framework for three marine coastal areas with contrasting climatic and ecological characteristics.

A reference configuration of the model including the benthic component was setup for each case study seeking for practical parameterizations able to describe the specific oceanic and biogeochemical regimes. The skill assessment of simulated environmental and ecological dynamics (BPC-RETURN experiment) was performed against available observational data at both annual and seasonal scales. A companion experiment neglecting the benthic feedback (NO-BPC experiment) was carried out to further evaluate the importance of both the sedimentation and remineralization processes in coastal systems.

Overall, the outcomes of the one-dimensional reference simulation allowed to adequately reproduce the spatio-temporal evolution of key biogeochemical variables, although some peculiarities emerged from each site. In the MA21

area (Gulf of Trieste) the introduction of the BPC sub-model led to an amelioration of the model skill in reproducing the vertical distribution of dissolved inorganic nutrients (with the exception of ammonium) and, to a lesser extent, of the chlorophyll-a concentrations.

In spite of the complex physical regime that characterizes St. Helena Bay, the achieved setup of the coupled 1D model allowed to reproduce the seasonal upwelling variability. In particular, the inclusion of benthic dynamics had a remarkable role in shaping the vertical distribution of key biogeochemical variables. The model application to the Svinøy Fyr site led to a satisfactory representation of the ecosystem dynamics in a deeper continental shelf system, by showing the role of BPC feedback on the evolution of the pelagic biogeochemical quantities during both the deep mixing period (autumn and winter) and the strongly stratified one (spring and summer).

An extensive sensitivity analysis was finally performed to investigate the response of the pelagic system with respect to different sedimentation-remineralization rates, by focusing on the changes of inorganic nutrients and chlorophyll-a distribution within the water column.

From the Normalized Root-Mean-Square Deviation analysis it was shown that the shallowest implemented site, the MA21, was the most sensitive site to BPC parameters variations, while the deepest station, the SFyr one, revealed the highest degree of resilience to the different BPC scenarios. Moreover, the analysis of the diffusive inorganic nutrients (Nitrate and Phosphate) fluxes from the sediment to the pelagic environment demonstrated that the MA21 and SHB areas are characterized by a more active benthic nutrients regeneration with respect to the deepest station of SFyr. The evolution of the pelagic organic carbon sedimentary flux was found to be not linearly dependent on the station depth, as it emerged from the comparison

of results obtained for the modelled sites.

The reasons for this have been identified in the physical conditions of the three sites where the mid-latitude MA21 and SFyr site were characterized by prolonged cooling and mixing periods and in MA21 by a deep biomass peak both enhancing the sinking flux. Contrarily, in SHB the shallowest Nutrient-Phytoplankton-Zooplankton food chain reproduced by the model and the prolonged upwelling period enhances the pelagic remineralization likely reducing the sedimentation flux.

The Taylor and Target summary diagrams showed and confirmed the statistical agreement in defining the Best Experiment in all the variables in the SHB site (the richest dataset used in this study). In Svinøy Fyr, the Best experiment was identified on the basis of the Target and RMSE analysis with the total RMSE mainly characterized by a more varying bias, with the exception of the chlorophyll that was well represented using all the statistical metrics. Some limitation, mainly due to dataset characteristics in terms of nutrients measurements availability, has been encountered in the MA21 area, while Taylor and Target analysis was considered reliable in describing chlorophyll dynamic. Here, beyond the applied sensitivity statistical procedure, the graphical analysis has been considered particularly important.

The graphical analysis generally confirmed the Best Experiments found using all the statistical patterns.

Moreover, the reproduced BPC fluxes in the MA21 area are qualitatively in agreement with previous works [41, 18, 118, 119, 120].

The best experiment found for the station implemented in St.Helena Bay denotes active benthic nutrients diffusive fluxes in agreement with what described by literature [90, 93].

Although site-specific information were not available for the Svinøy Fyr site, the reproduced not particularly active BPC conditions allowed to confirm previous hypotheses [19] regarding the relationships between the BPC fluxes and depth. Moreover, the Best Experiment BPC conditions of burial flux qualitatively represent the dynamic described by [106, 107] where a large portion of the carbon fixed annually by phytoplankton falls ungrazed to the sediments.

The future continuation of this study should aim (i) to further extend the set of study sites to include additional ecosystems and (ii) to validate BPC sub-models parameterization by means of experimental data.

Although significant results were achieved in this study, the limited extension of observational datasets hindered a more detailed representation of the benthic-pelagic coupling processes and experimental evidences are urgently needed to adequately support the development of benthic system modelling.

In the light of the presented analyses, the proposed BPC sub-model can be profitably implemented on the wider global ocean scale to complement the investigation of biogeochemical cycles and improve the assessment of carbon dynamics.

Finally, aiming to obtain a more robust numerical description of the sediment-water exchanges in coastal waters, it is strongly recommended to increase the number of benthic processes numerically described by the BPC sub-model.

Appendix A

Appendix

A.1 Model Parameterization

Table A.1: List of the parameters in the BFM pelagic equations for phytoplankton.

Parameter	Symbol	$P^{(1)}$	$P^{(2)}$	$P^{(3)}$	$P^{(4)}$
Q10 coefficient	p _q10	2.0	2.0	2.0	2.0
Cut-off threshold for temperature factor	p_qtemp	0.0	0.0	0.0	0.0
Maximal productivity at 10°C (day^{-1})	p_sum	1.3	1.02	1.6	0.83
Respiration rate at 10°C (day^{-1})	p_srs	0.05	0.05	0.05	0.1
Max.specific nutrient-stress lysis rate (day^{-1})	p_sdmo	0.01	0.01	0.01	0.2.
Half saturation constant for nutrient stress lysis (–)	p_thdo	0.1	0.1	0.1	0.5
Extra lysis rate (biomass density-dependent) (day^{-1})	p_seo	0.0	0.0	0.0	0.5
Half saturation constant for extra lysis ($mgC\ m^{-3}$)	p_sheo	0.0	0.0	0.0	100.0
Excreted fraction of primary production (–)	p_pu_ea	0.01	0.1	0.1	0.15
Activity respiration fraction (–)	p_pu_ra	0.1	0.1	0.2	0.1
Membrane affinity for N (m^3/mgC/day)	p_qun	0.025	0.025	0.025	0.025.
Half saturation constant for NH_4 uptake preference over NO_3 ($mmolN/m^3$)	p_lN4	1.0	0.5	0.1	1.0
Minimum quotum N:C (mmolN/mgC)	p_qnlc	$6.87x10^{-3}$	$6.87x10^{-3}$	$6.87x10^{-3}$	$6.87x10^{-3}$
Reference quotum N:C (mmolN/mgC)	p_qncPPY	$1.26x10^{-2}$	$1.266x10^{-2}$	$1.266x10^{-2}$	$1.26x10^{-2}$
Multiplication factor for luxury storage (–)	p_xqn	2.0	2.0	2.0	2.0
Membrane affinity for P (m3 /mgC/day)	p_qup	0.0025	0.0025	0.0025	0.0025
Minimum quotum P:C (mmolP/mgC)	p_qplc	$4.29x10^{-4}$	$4.29x10^{-4}$	$4.29x10^{-4}$	$4.29x10^{-4}$
Reference quotum P:C (mmolP/mgC)	p_qpcPPY	$7.86x10^{-4}$	$7.86x10^{-4}$	$7.86x10^{-4}$	$7.86x10^{-4}$
Multiplication factor for luxury storage (–)	p_xqp	2.0	2.0	2.0	2.0
Half saturation conc. for dissolved Si limitation ($mmolSi\ m^{-3}$))	p_chPs	1.0	0.0	0.0	0.0
Membrane affinity for Si (m^3/mgC/day)	p_qus	0.0025	0.0	0.0	0.0
Minimum quotum Si:C (mmolSi/mgC)	p_qslc	0.007	0.0	0.0	0.0
Reference quotum Si:C (mmolSi/mgC)	p_qscPPY	$8.5x10^{-3}$	0.0	0.0	0.0
Nutrient stress threshold for sinking (–)	p_esNI	0.7	0.75	0.75	0.75
Maximum Sinking velocity (m day^{-1})	p_res	5.0	0.0	0.0	5.0
Specific turnover rate for Chla (day^{-1})	p_sdchl	0.2	0.2	0.2	0.2
Initial slope of the P-E curve (mgC s m^2 /mgChl/uE)	p_alpha_chl	$1.38x10^{-5}$	$0.46x10^{-5}$	$1.52x10^{-5}$	$0.46x10^{-5}$
Reference quotum Chla:C (mgChla/mgC)	p_qlcPPY	0.025	0.015	0.02	0.015
Chla-specific extinction coefficient (m^2/mgChla)	p_epsChla	0.03	0.03	0.03	0.03
Relaxation rate towards maximum Chla:C (day^{-1})	p_totchl_relt	0.25	0.25	0.25	0.25
Optimal value of E_PAR/E_K (–)	p_EpEk_or	3.0	3.0	3.0	3.0

Table A.2: List of the parameters in the BFM pelagic equations for microzooplankton.

Parameter	Symbol	$Z^{(5)}$	$Z^{(6)}$
Q10 value for physiological rates (-)	p_q10	2.0	2.0
Respiration rate at 10°C (day^{-1})	p_srs	0.02	0.02
Potential growth rate (day^{-1})	p_sum	2.0	5.0
Mortality rate due to oxygen limitation (day^{-1})	p_sdo	0.25	0.25
Temperature independent mortality (day^{-1})	p_sd	0.0	0.0
Assimilation efficiency (-)	p_pu	0.5	0.3
Fraction of activity excretion (-)	p_pu_ea	0.25	0.35
Half-saturation oxygen concentration ($mmolO_2\ m^{-3}$)	p_chro	30.0	30.0
Half-saturation food concentration for Type II (mgC m^{-3})	p_chuc	200.0	200.0
Half-saturation food concentration for preference factor (mgC m^{-3})	p_minfood	50.0	50.0
Portion of egested calcified shells during grazing (-)	p_pecaco3	0.5	0.5
Maximum quotum N:C (mmolN/mgC)	p_qncMIZ	1.67d-2	1.67d-2
Maximum quotum P:C (mmolN/mgC)	p_qpcMIZ	1.85d-3	1.85d-3

Table A.3: List of the parameters in the BFM pelagic equations for mesozooplankton.

Parameter	Symbol	$Z^{(3)}$	$Z^{(4)}$
Q10 value for physiological rates (-)	p_q10	2.0	2.0
Respiration rate at 10°C (day^{-1})	p_srs	0.01	0.02
Potential growth rate (day^{-1})	p_sum	2.0	2.0
Specific search volume ($m^3 mgC day^{-1}$)	p_vum	0.0025	0.0025
Assimilation efficiency (-)	p_puI	0.6	0.6
Fraction of faeces production (-)	p_peI	0.3	0.35
Specific density-dependent mortality (m^3 mgC day^{-1})	p_p_sdo	0.01	0.01
Background natural mortality (day^{-1})	p_p_sd	0.02	0.01
Exponent of density-dependent mortality (-)	p_p_sds	2.0	2.0
Portion of egested calcified shells during grazing (-)	p_pecaco3	0.75	0.75
Maximum quotum N:C (mmolN/mgC)	p_qncMEZ	0.015	0.015
Maximum quotum P:C (mmolN/mgC)	p_qpcMEZ	1.67d-3	1.67d-3
Half-saturation oxygen concentration ($mmolO_2\ m^{-3}$)	p_p_clO2o	30.0	30.0

Table A.4: Pelagic bacteria parameters description and value.

Parameter	Symbol	$B^{(1)}$
Characteristic Q10 (-)	p_q10	2.95
Half-saturation constant for O_2 (mmolO_2 m^{-3})	p_p_chdo	30.0
Specific mortality rate (day^{-1})	p_sd	0.05
Density dependent specific mortality rate (day^{-1})	p_sd2	0.0
Specific potential uptake for nutrient-rich DOM (day^{-1})	p_suhR1	0.03
Specific potential uptake for nutrient-poor DOM (day^{-1})	p_sulR1	0.0
Specific potential uptake for semi-labile DOC (day^{-1})	p_suR2	0.0
Specific potential uptake for semi-refractory DOC (day^{-1})	p_suR3	0.0
Specific potential uptake for POM (day^{-1})	p_suR6	0.01
Specific potential growth rate (day^{-1})	p_sum	8.38
Activity respiration fraction (-)	p_pu_ra	0.06
Additional respiration fraction at low O_2 concentration (-)	p_pu_ra_0	0.02
Specific rest respiration (day^{-1})	p_srs	0.01
Optimal N/C ratio (mmolN/mgC)	p_qncPBA	0.0126
Optimal P/C ratio (mmolP/mgC)	p_qpcPBA	0.7862e-3
Minimal N/C ratio (mmolN/mgC)	p_qlnc	0.0167
Minimal P/C ratio (mmolP/mgC)	p_qlpc	0.0018
Membrane affinity for N (mmolN/mgC/day)	p_qun	0.0
Membrane affinity for P (mmolP/mgC/day)	p_qup	0.0
Half saturation ammonium conc. for uptake ($mmolN/m^3$)	p_chn	5.0
Half saturation phosphate conc. for uptake ($mmolP/m^3$)	p_chp	1.0
Relaxation timescale for N uptake/remin. (day^{-1})	p_ruen	1.0
Relaxation timescale for P uptake/remin. (day^{-1})	p_ruep	1.0
Relaxation timescale for semi-labile excretion (day^{-1})	p_rec	1.0
Excretion of semi-refractory DOC (-)	p_pu_ea_R3	0.0

Predators	**Preys**								
	$P_i^{(1)}$	$P_i^{(2)}$	$P_i^{(3)}$	$P_i^{(4)}$	$Z_i^{(3)}$	$Z_i^{(4)}$	$Z_i^{(5)}$	$Z_i^{(6)}$	$B_i^{(1)}$
$Z_i^{(3)}$	0.0	0.0	0.0	0.0	1.0	1.0	1.0	0.0	0.0
$Z_i^{(4)}$	1.0	0.75	0.7	0.5	0.0	1.0	1.0	0.0	0.0
$Z_i^{(5)}$	1.0	1.0	0.1	0.4	0.0	0.0	1.0	1.0	0.1
$Z_i^{(6)}$	0.0	0.2	1.0	0.0	0.0	0.0	0.0	0.2	1.0

Table A.5: Pelagic food matrix.

A.2 Sensitivity Analysis Results

A.2.1 SHB

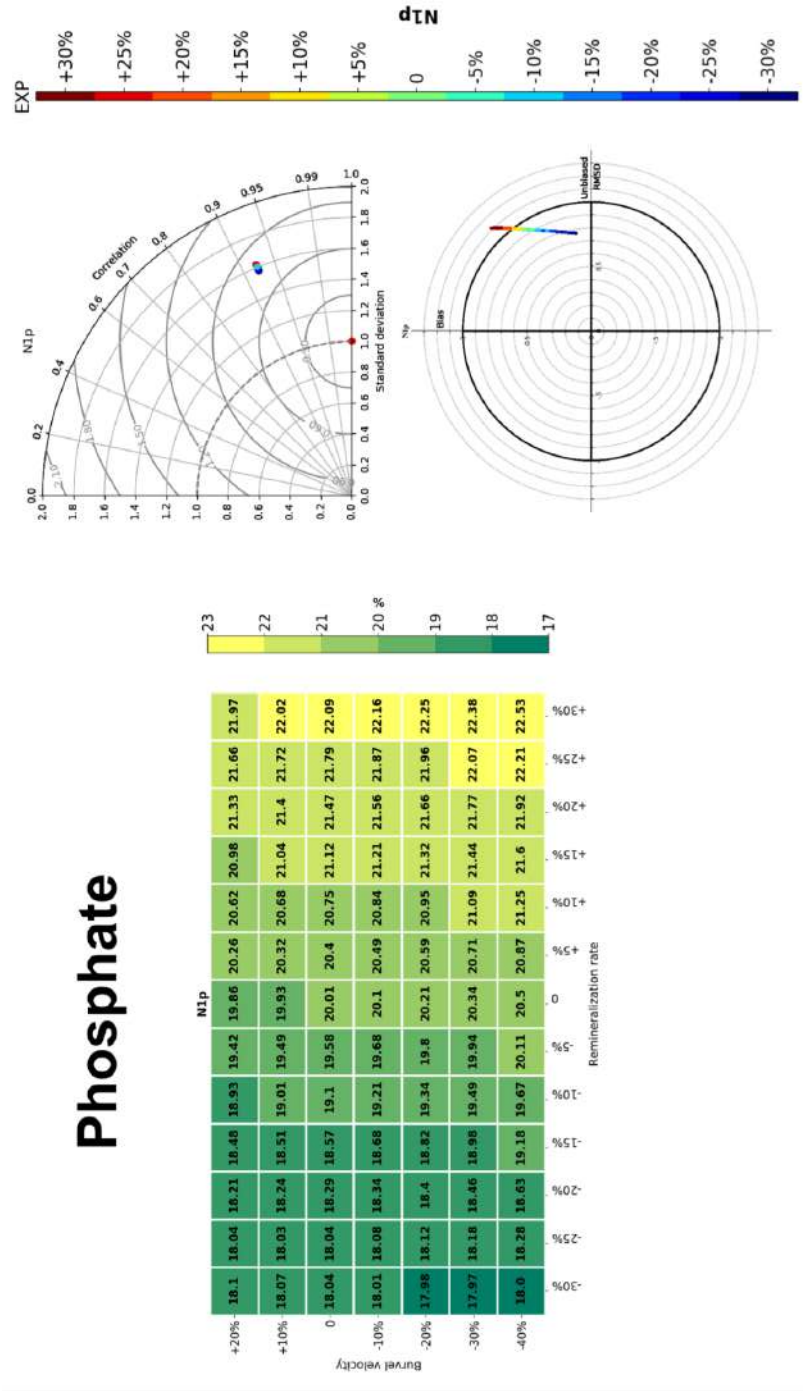

Figure A.1: Sensitivity Analysis results. RMSE analysis, Summary Taylor and target diagrams for the phosphate

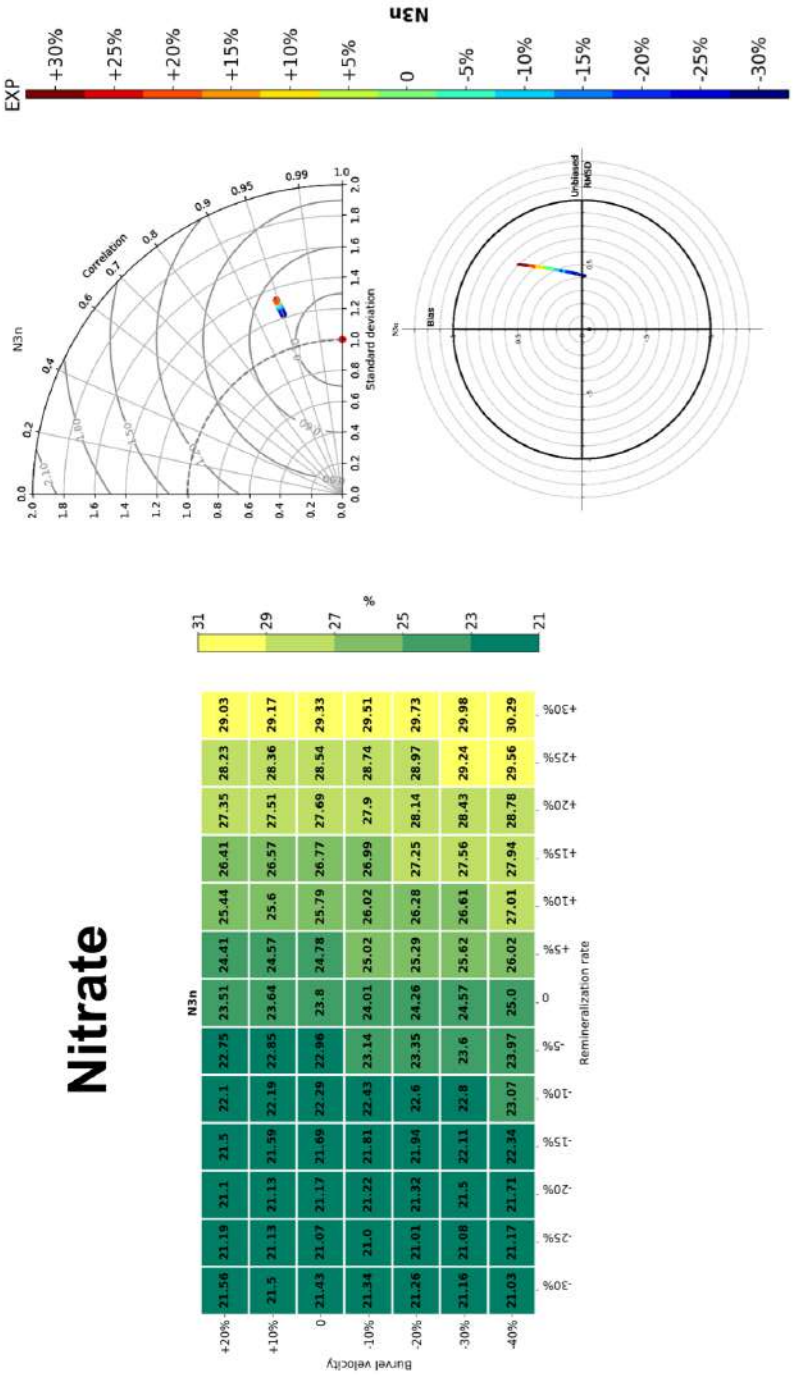

Figure A.2: Sensitivity Analysis results. RMSE analysis, Summary Taylor and target diagrams for the nitrate

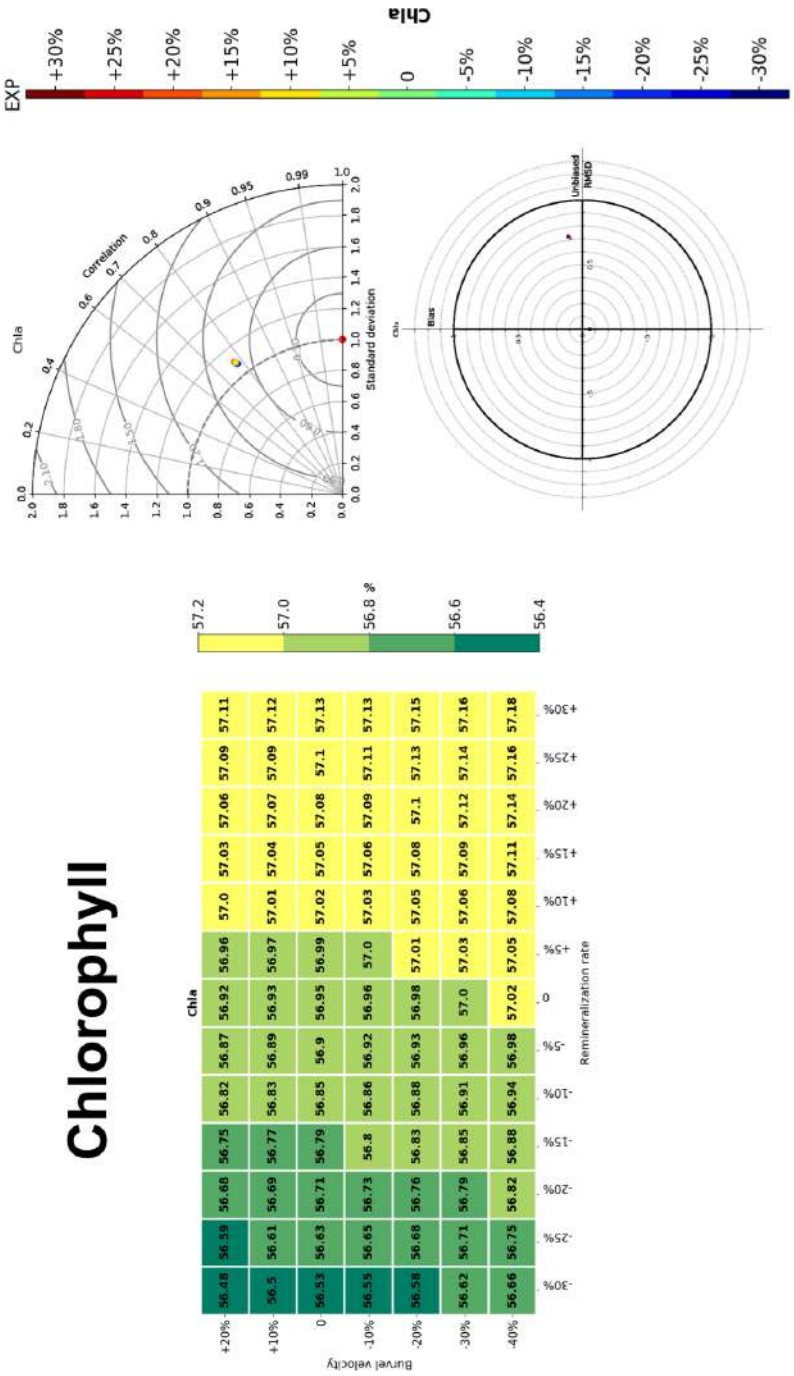

Figure A.3: Sensitivity Analysis results. RMSE analysis, Summary Taylor and target diagrams for the chlorophyll

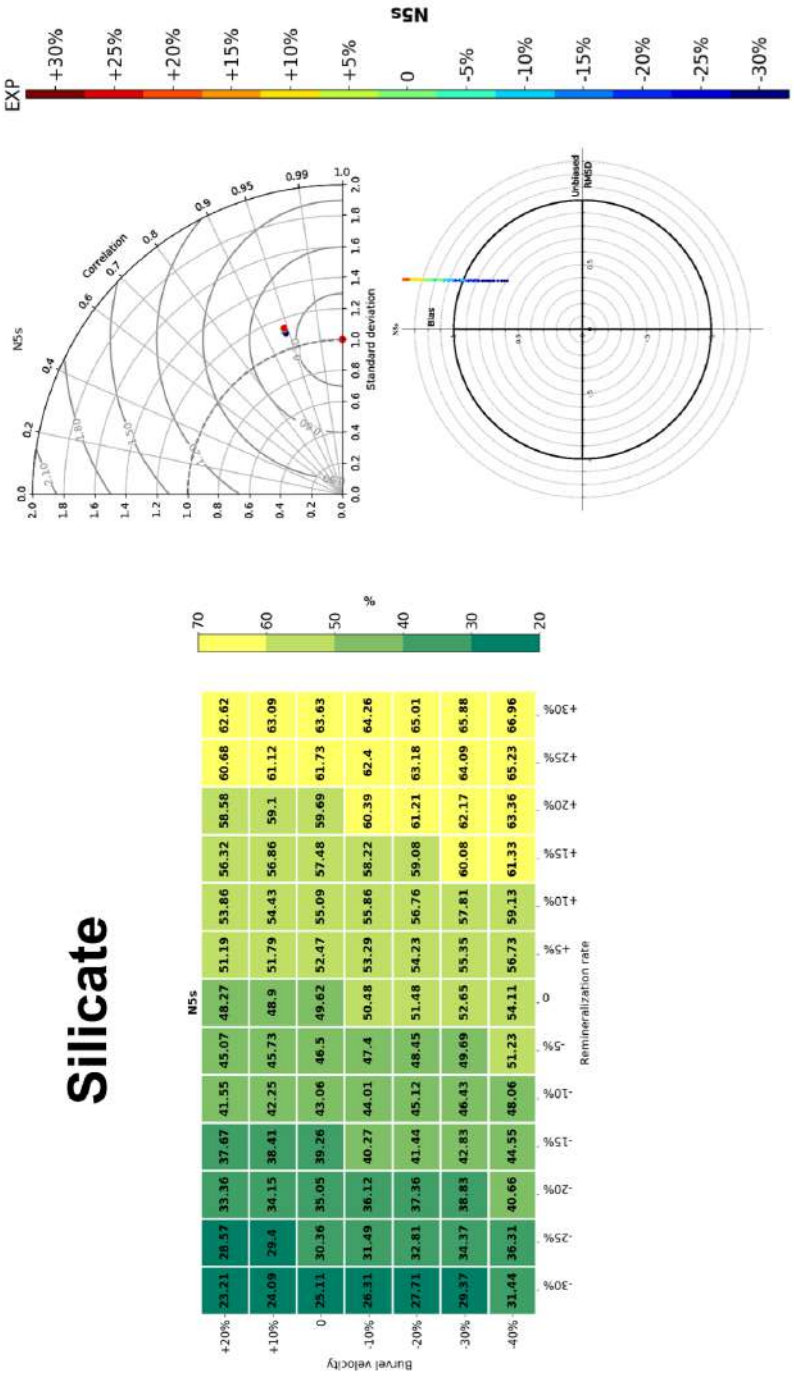

Figure A.4: Sensitivity Analysis results. RMSE analysis, Summary Taylor and target diagrams for the Silicate

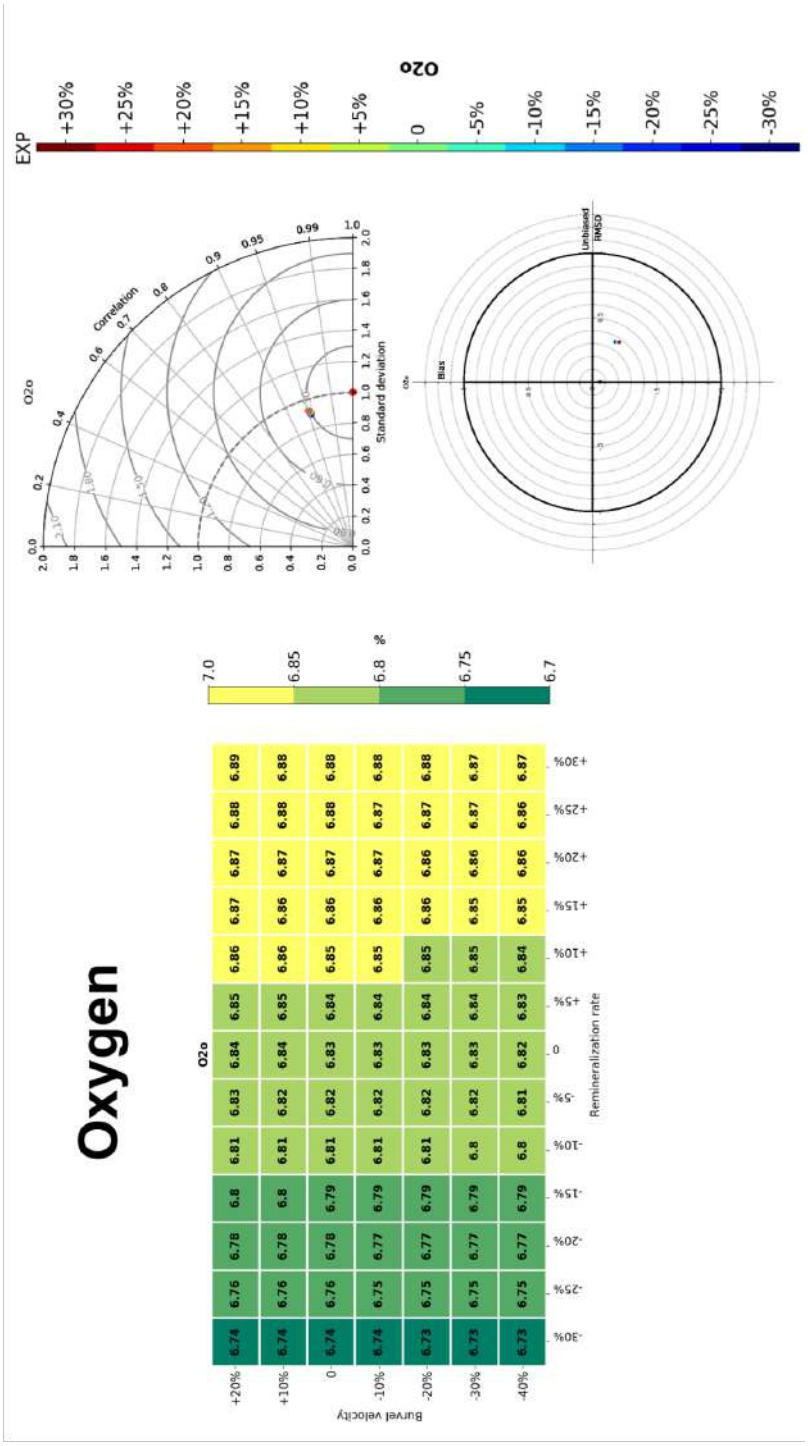

Figure A.5: Sensitivity Analysis results. RMSE analysis, Summary Taylor and target diagrams for the oxygen

A.2.2 Svinøy Fyr

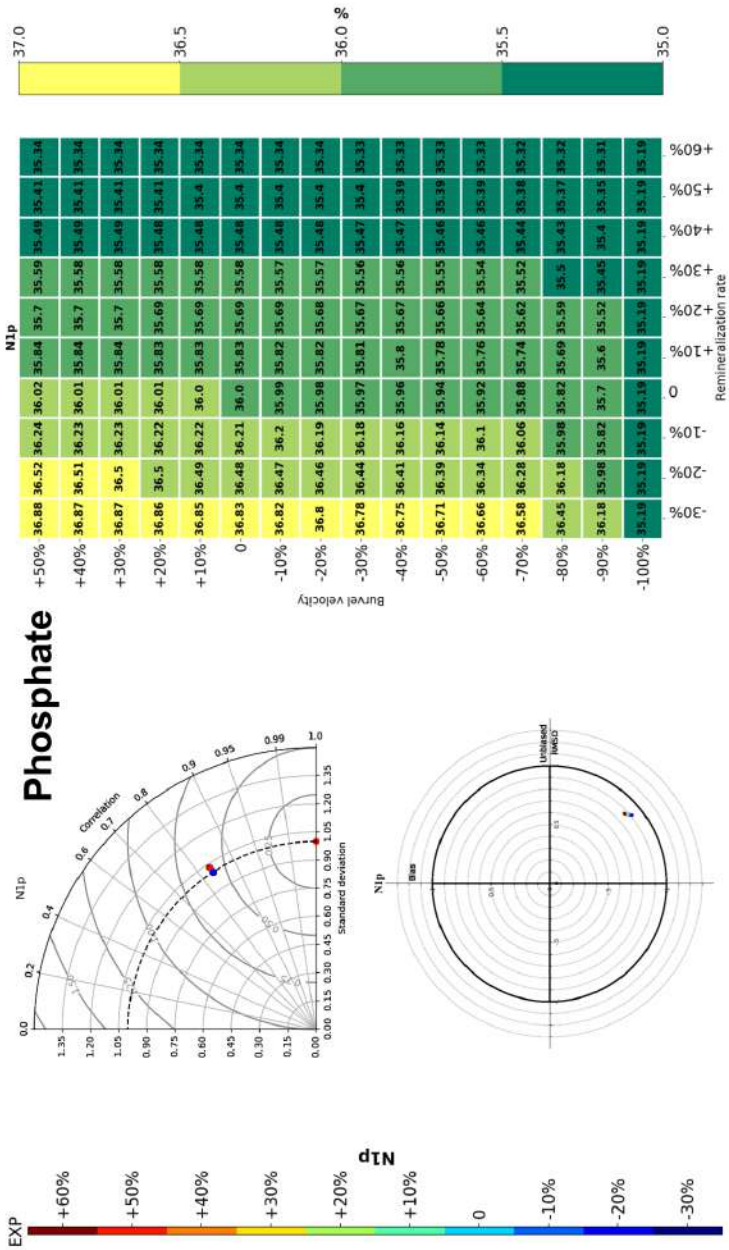

Figure A.6: Sensitivity Analysis results. RMSE analysis, Summary Taylor and target diagrams for the phosphate

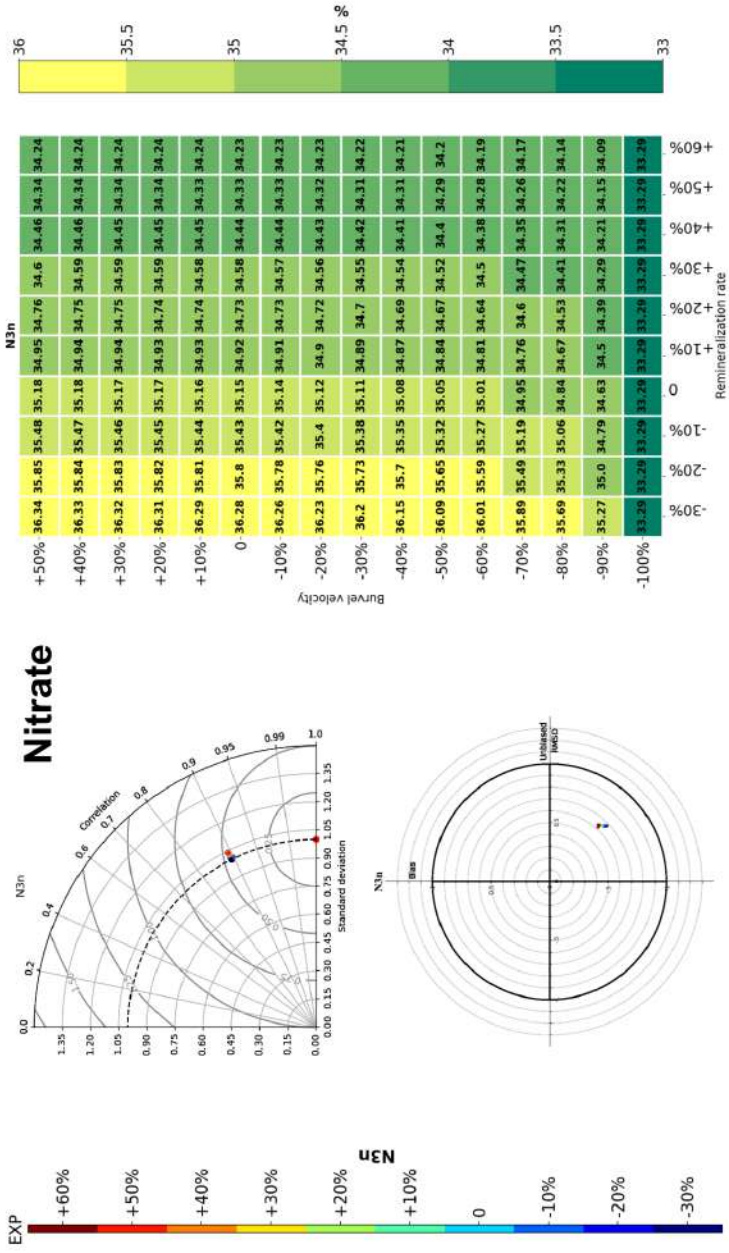

Figure A.7: Sensitivity Analysis results. RMSE analysis, Summary Taylor and target diagrams for the nitrate

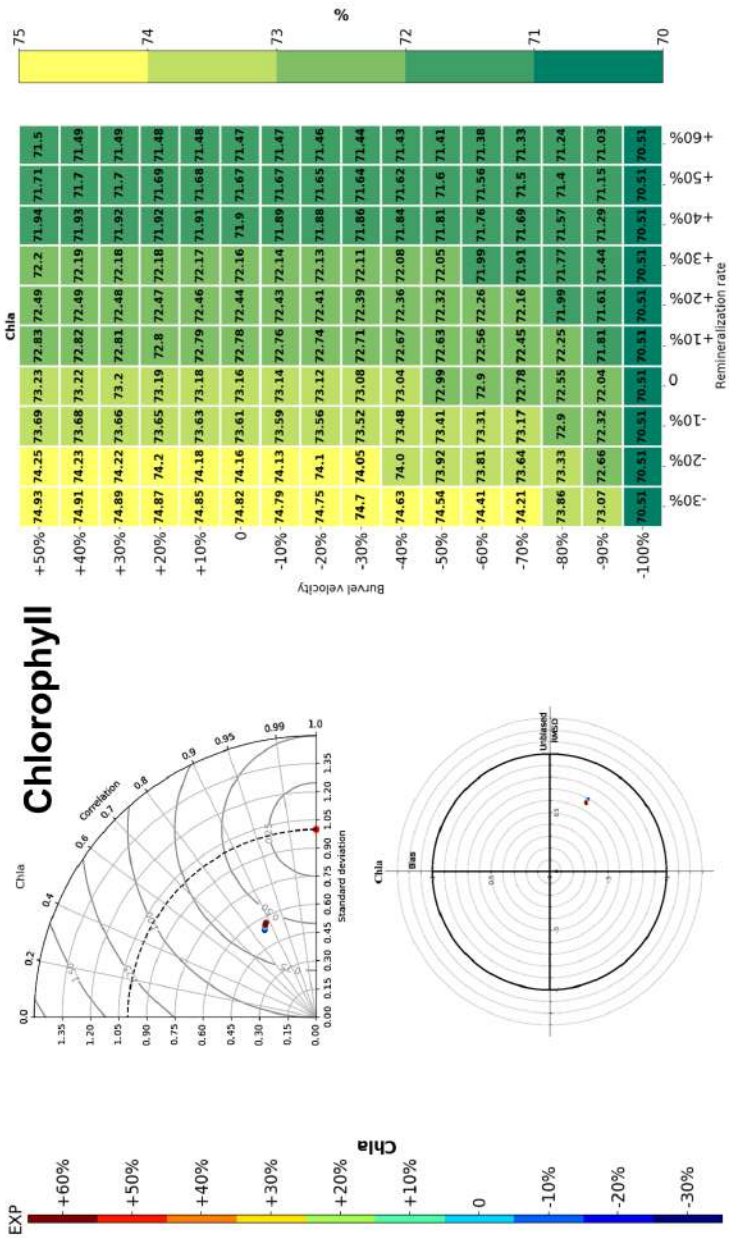

Figure A.8: Sensitivity Analysis results. RMSE analysis, Summary Taylor and target diagrams for the chlorophyll

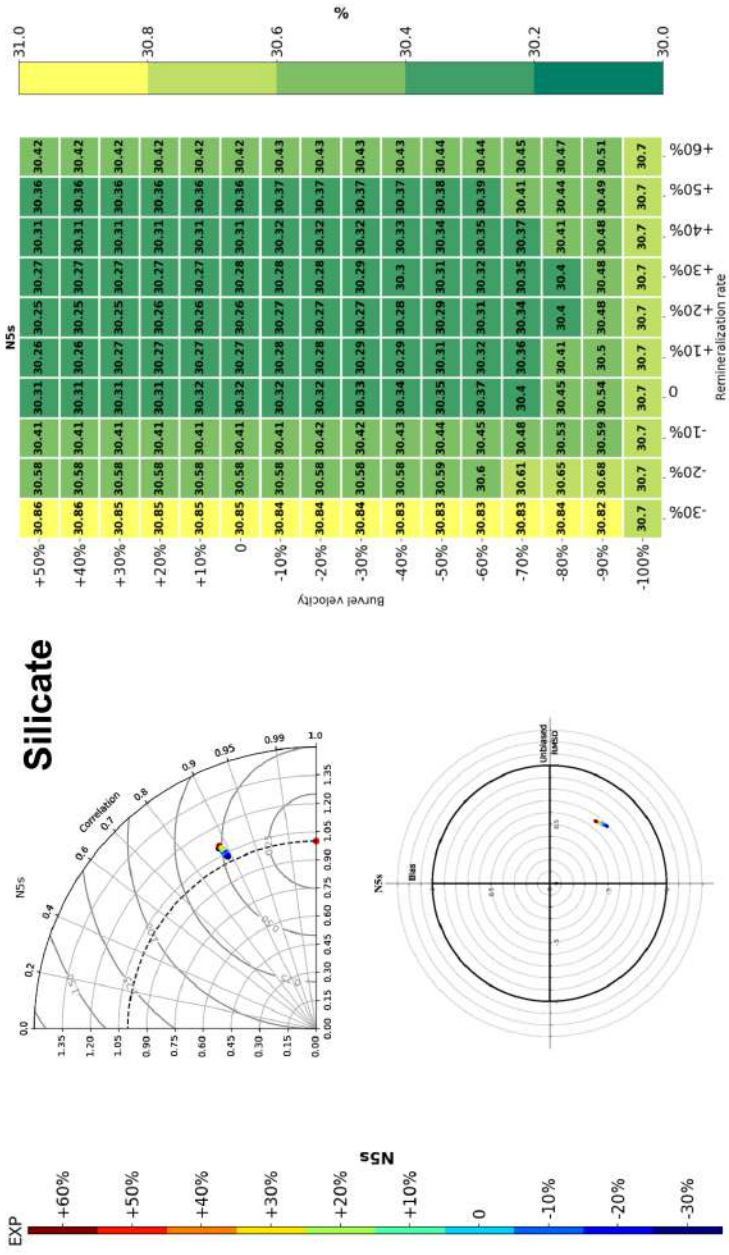

Figure A.9: Sensitivity Analysis results. RMSE analysis, Summary Taylor and target diagrams for the silicate

A.2.3 MA21

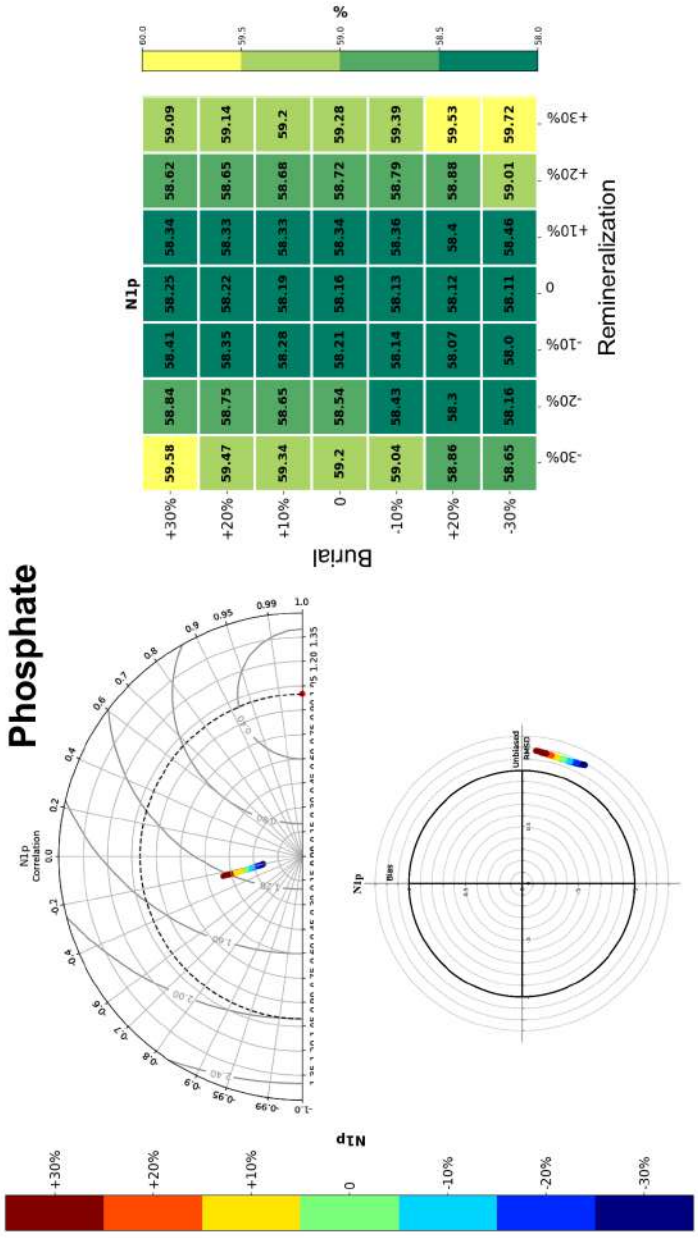

Figure A.10: Sensitivity Analysis results. RMSE analysis, Summary Taylor and target diagrams for the phosphate

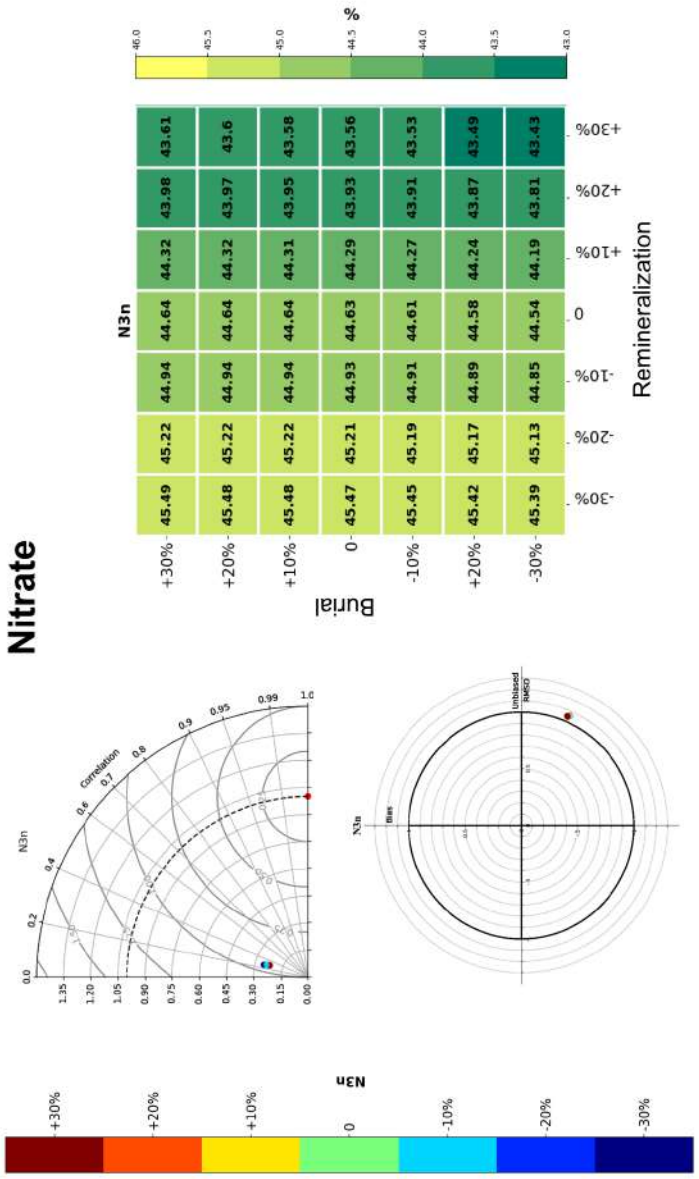

Figure A.11: Sensitivity Analysis results. RMSE analysis, Summary Taylor and target diagrams for the nitrate

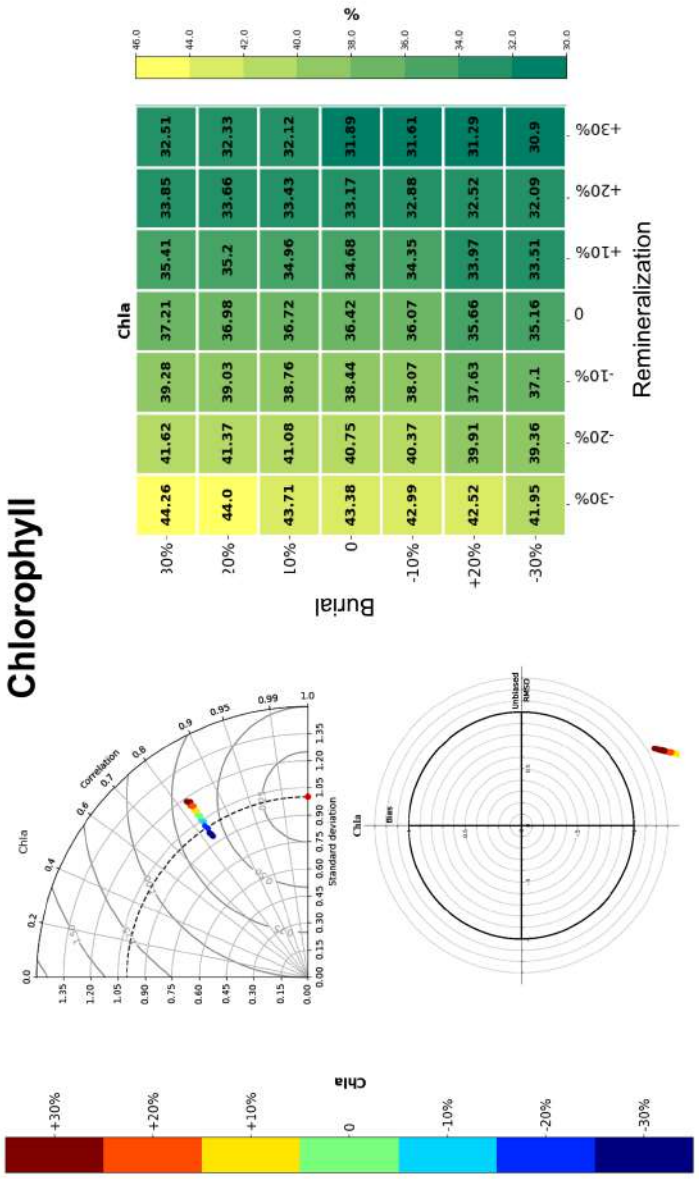

Figure A.12: Sensitivity Analysis results. RMSE analysis, Summary Taylor and target diagrams for the chlorophyll

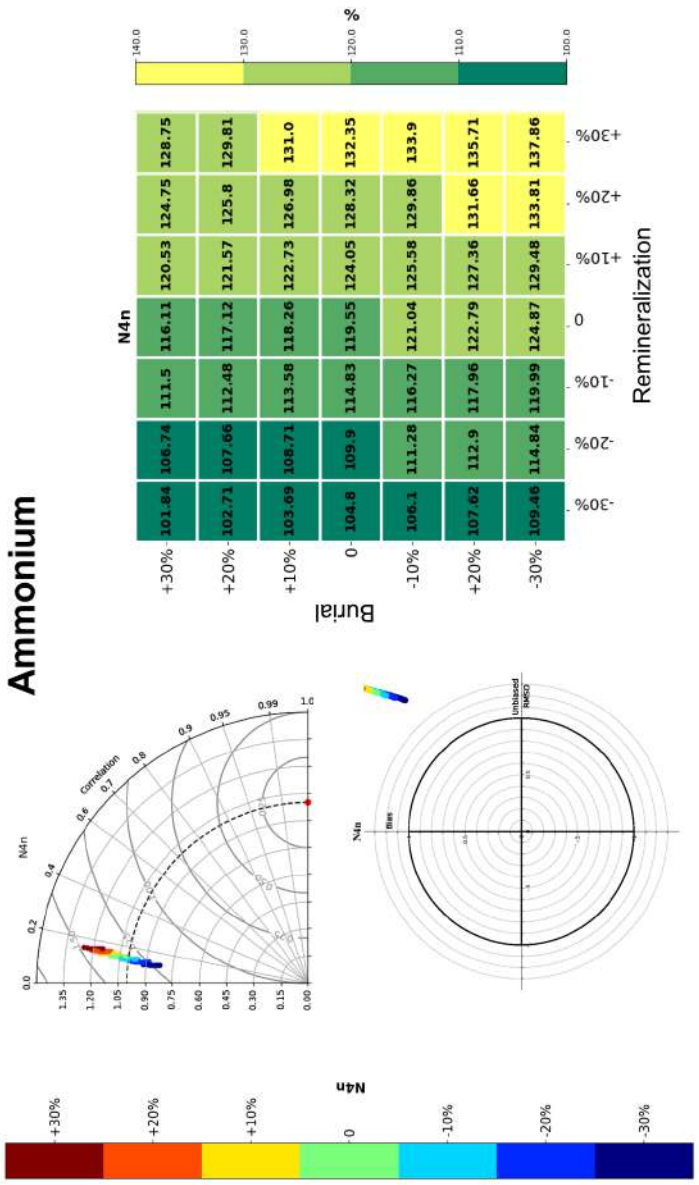

Figure A.13: Sensitivity Analysis results. RMSE analysis, Summary Taylor and target diagrams for the ammonium

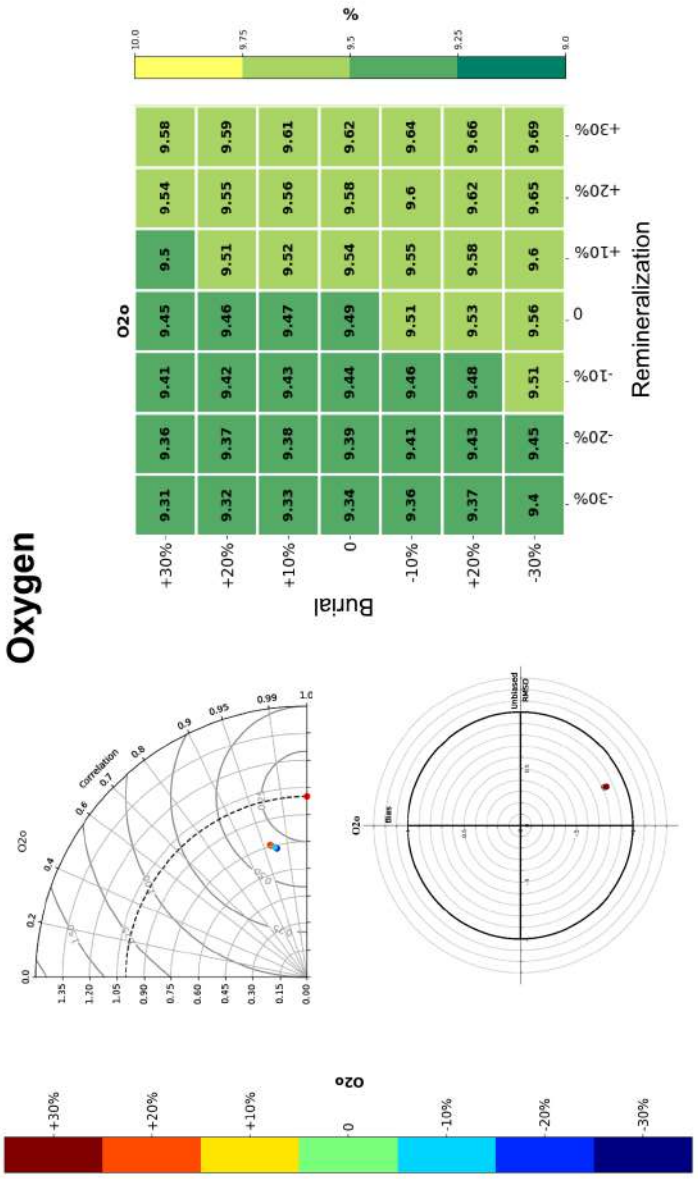

Figure A.14: Sensitivity Analysis results. RMSE analysis, Summary Taylor and target diagrams for the oxygen

Bibliography

[1] Peter Burt. "The oceans and climate. By Grant Bigg. Cambridge University Press, second edition 2003. xi + 273pp. ISBNs 0 521 01634 7, 0 521 81570 3". In: *Weather* 59 (Dec. 2006), pp. 190–190. DOI: 10.1256/wea.36.04.

[2] A Ganachaud and C Wunsch. "Improved estimates of global ocean circulation, heat transport and mixing from hydrographic data (vol 408, pg 453, 2000)". In: *Nature* 410 (Mar. 2001), pp. 240–240. DOI: 10.1038/35065660.

[3] K. Maier-Reimer E. Hasselmann. "Transport and storage of CO2 in the ocean ——an inorganic ocean-circulation carbon cycle model". In: *Climate Dynamics* 2 (Sept. 1987), pp. 63–90. DOI: https://doi.org/10.1007/BF01054491.

[4] Ernst Maier-Reimer. "Geochemical cycles in an ocean general circulation model. Preindustrial tracer distributions". In: *Global Biogeochemical Cycles* 7.3 (1993), pp. 645–677. DOI: 10.1029/93GB01355.

[5] Jorge L. Sarmiento, James C. Orr, and Ulrich Siegenthaler. "A perturbation simulation of CO2 uptake in an ocean general circulation

model". In: *Journal of Geophysical Research: Oceans* 97.C3 (1992), pp. 3621–3645. DOI: 10.1029/91JC02849.

[6] Moore J.K. Doney S.C. Lindsay K. "Global Ocean Carbon Cycle Modeling". In: *Fasham M.J.R. (eds) Ocean Biogeochemistry. Global Change — The IGBP Series (closed)* (2003). Ed. by Springer-Verlag Berlin Heidelberg. DOI: https://doi.org/10.1007/978-3-642-55844-3_10.

[7] Ernst Maier-Reimer, Uwe Mikolajewicz, and Arne Winguth. "Future ocean uptake of CO2: interaction between ocean circulation and biology". In: *Climate Dynamics* 12.10 (1996), pp. 711–722.

[8] Fortunat Joos et al. "Global warming and marine carbon cycle feedbacks on future atmospheric CO2". In: *Science* 284.5413 (1999), pp. 464–467.

[9] G-K Plattner et al. "Feedback mechanisms and sensitivities of ocean carbon uptake under global warming". In: *Tellus B* 53.5 (2001), pp. 564–592.

[10] A. Navarra. "Ensembles, Forecasts and Predictability". In: (2002). Ed. by Springer-Verlag Berlin Heidelberg New York, pp. 131–148.

[11] Christopher L Sabine and Richard A Feely. "The oceanic sink for carbon dioxide". In: *Greenhouse gas sinks* 31 (2007).

[12] Jason Holt et al. "Modelling the global coastal ocean". In: *Philosophical transactions. Series A, Mathematical, physical, and engineering sciences* 367 (Mar. 2009), pp. 939–51. DOI: 10.1098/rsta.2008.0210.

[13] Amber K. Hardison et al. "Arctic shelves as platforms for biogeochemical activity: Nitrogen and carbon transformations in the Chukchi Sea, Alaska". In: *Deep Sea Research Part II: Topical Studies in Oceanography* 144 (2017). The Hanna Shoal Ecosystem of the Northeastern Chukchi Seashelf, pp. 78–91. ISSN: 0967-0645. DOI: https://doi.org/10.1016/j.dsr2.2017.08.004.

[14] K Soetaert et al. "On the coupling of benthic and pelagic biogeochemical models". In: *Earth-Science Reviews* 51 (Aug. 2000), pp. 173–201. DOI: 10.1016/S0012-8252(00)00004-0.

[15] Jennifer R. Griffiths et al. "The importance of benthic–pelagic coupling for marine ecosystem functioning in a changing world". In: *Global Change Biology* 23.6 (2017), pp. 2179–2196. DOI: 10.1111/gcb.13642. eprint: https://onlinelibrary.wiley.com/doi/pdf/10.1111/gcb.13642. URL: https://onlinelibrary.wiley.com/doi/abs/10.1111/gcb.13642.

[16] Sandra Arndt et al. "Quantifying the degradation of organic matter in marine sediments: A review and synthesis". In: *Earth-Science Reviews* 123 (2013), pp. 53–86. ISSN: 0012-8252. DOI: https://doi.org/10.1016/j.earscirev.2013.02.008. URL: http://www.sciencedirect.com/science/article/pii/S0012825213000512.

[17] Pierre Regnier et al. "Anthropogenic perturbation of the carbon fluxes from land to ocean". In: *Nature geoscience* 6.8 (2013), pp. 597–607.

[18] Giulia Mussap and Marco Zavatarelli. "A numerical study of the benthic–pelagic coupling in a shallow shelf sea (Gulf of Trieste)". In: *Regional studies in marine science* 9 (2017), pp. 24–34.

[19] Erwin Suess. "Particulate organic carbon flux in the oceans: Surface and oxygen utilization". In: *Nature* (Jan. 1980).

[20] Jefferson T Turner. "Zooplankton fecal pellets, marine snow and sinking phytoplankton blooms". In: *Aquatic microbial ecology* 27.1 (2002), pp. 57–102.

[21] L Christina and Uta Passow. "Factors influencing the sinking of POC and the efficiency of the biological carbon pump". In: *Deep Sea Research Part II: Topical Studies in Oceanography* 54.5-7 (2007), pp. 639–658.

[22] Panagiotis D Dimitriou et al. "One step forward: benthic pelagic coupling and indicators for environmental status". In: *PloS one* 10.10 (2015), e0141071.

[23] M Kralj et al. "Hypoxia and dissolved oxygen trends in the northeastern Adriatic Sea (Gulf of Trieste)". In: *Deep Sea Research Part II: Topical Studies in Oceanography* (2019).

[24] Josep-Maria Gili and Rafel Coma. "Benthic suspension feeders: their paramount role in littoral marine food webs". In: *Trends in ecology & evolution* 13.8 (1998), pp. 316–321.

[25] MM Baustian et al. "Linking the bottom to the top in aquatic ecosystems: mechanisms and stressors of benthic-pelagic coupling". In: *Eco-DAS X Symposium Proceedings (ed Kemp PF)*. 2014, pp. 25–47.

[26] Kim Hansen, Steen Mouridsen, and Erik Kristensen. "The impact of Chironomus plumosus larvae on organic matter decay and nutrient (N, P) exchange in a shallow eutrophic lake sediment following a phy-

toplankton sedimentation". In: *Hydrobiologia* 364.1 (1997), pp. 65–74.

[27] Andrew M Lohrer, Simon F Thrush, and Max M Gibbs. "Bioturbators enhance ecosystem function through complex biogeochemical interactions". In: *Nature* 431.7012 (2004), p. 1092.

[28] Anthony F D'Andrea and Theodore H DeWitt. "Geochemical ecosystem engineering by the mud shrimp Upogebia pugettensis (Crustacea: Thalassinidae) in Yaquina Bay, Oregon: Density-dependent effects on organic matter remineralization and nutrient cycling". In: *Limnology and Oceanography* 54.6 (2009), pp. 1911–1932.

[29] Robert A Berner. *Early diagenesis: a theoretical approach*. 1. Princeton University Press, 1980.

[30] CHR Heip et al. "The role of the benthic biota in sedimentary metabolism and sediment-water exchange processes in the Goban Spur area (NE Atlantic)". In: *Deep Sea Research Part II: Topical Studies in Oceanography* 48.14-15 (2001), pp. 3223–3243.

[31] Gennadi Lessin et al. "Modelling marine sediment biogeochemistry: Current knowledge gaps, challenges, and some methodological advice for advancement". In: *Frontiers in marine science* 5 (2018), p. 19.

[32] Dominik Hülse et al. "Understanding the causes and consequences of past marine carbon cycling variability through models". In: *Earth-science reviews* 171 (2017), pp. 349–382.

[33] J Val Klump and Christopher S Martens. "Biogeochemical cycling in an organic rich coastal marine basin—II. Nutrient sediment-water ex-

change processes". In: *Geochimica et Cosmochimica Acta* 45.1 (1981), pp. 101–121.

[34] Steven Emerson, Richard Jahnke, and David Heggie. "Sediment-water exchange in shallow water estuarine sediments". In: *Journal of Marine Research* 42.3 (1984), pp. 709–730.

[35] C P Slomp, JFP Malschaert, and W Van Raaphorst. "The role of adsorption in sediment-water exchange of phosphate in North Sea continental margin sediments". In: *Limnology and Oceanography* 43.5 (1998), pp. 832–846.

[36] Gurvan Madec et al. "NEMO ocean engine". In: (2015).

[37] M Vichi et al. "The biogeochemical flux model (BFM): Equation description and user manual, BFM version 5.1". In: *BFM Rep. Ser* 1 (2015), p. 104.

[38] M Vichi et al. "Coupling BFM with Ocean models: the NEMO model (Nucleus for the European Modelling of the Ocean)". In: *BFM Report series* 2 (2015).

[39] Guillaume Reffray, Romain Bourdallé-Badie, and Christophe Calone. "Modelling turbulent vertical mixing sensitivity using a 1-D version of NEMO". In: *Geoscientific Model Development* 8 (Jan. 2015), pp. 69–86. DOI: 10.5194/gmd-8-69-2015.

[40] Lars Umlauf and Hans Burchard. "A generic length-scale equation for geophysical turbulence models". In: *Journal of Marine Research* 61 (Mar. 2003), pp. 235–265. DOI: 10.1357/002224003322005087.

[41] Giulia Mussap et al. “A management oriented 1-D ecosystem model: Implementation in the Gulf of Trieste (Adriatic Sea)”. In: *Regional Studies in Marine Science* 6 (2016), pp. 109–123.

[42] William George Large and Stephen G Yeager. “Diurnal to decadal global forcing for ocean and sea-ice models: the data sets and flux climatologies”. In: (2004).

[43] Letizia Tedesco and Marcello Vichi. “A new implementation of the Biogeochemical Flux Model in sea ice”. In: *CMCC Research Paper* 81 (2010).

[44] Marcello Vichi, Pinardi Nadia, and Simona Masina. “A generalized model of pelagic biogeochemistry for the global ocean ecosystem. Part I: Theory”. In: *Journal of Marine Systems* 64 (Jan. 2007), pp. 89–109. DOI: 10.1016/j.jmarsys.2006.03.006.

[45] J.G. Baretta-Bekker, J.W. Baretta, and W. Ebenhöh. “Microbial dynamics in the marine ecosystem model ERSEM II with decoupled carbon assimilation and nutrient uptake”. In: *Journal of Sea Research* 38.3 (1997). European Regional Seas Ecosystem Model II, pp. 195–211. ISSN: 1385-1101. DOI: https://doi.org/10.1016/S1385-1101(97)00052-X. URL: http://www.sciencedirect.com/science/article/pii/S138511019700052X.

[46] Thomas Smith et al. “Plant Functional Types”. In: Jan. 1993, pp. 272–292. ISBN: 0-412-03671-1. DOI: 10.1007/978-1-4615-2816-6_14.

[47] Corinne Le Quéré et al. “Ecosystem dynamics based on plankton functional types for global ocean biogeochemistry models”. In: *Global*

Change Biology 11.11 (2005), pp. 2016–2040. DOI: 10.1111/j.1365-2486.2005.1004.x.

[48] J.C. Blackford and P.J. Radford. "A structure and methodology for marine ecosystem modelling". In: *Netherlands Journal of Sea Research* 33.3 (1995), pp. 247–260. ISSN: 0077-7579. DOI: https://doi.org/10.1016/0077-7579(95)90048-9. URL: http://www.sciencedirect.com/science/article/pii/0077757995900489.

[49] Nancy H. Marcus and Nancy H. Marcus. "Minireview: The importance of benthic-pelagic coupling and the forgotten role of life cycles in coastal aquatic systems". In: *Limnology and Oceanography* 43.5 (1998), pp. 763–768. DOI: 10.4319/lo.1998.43.5.0763. eprint: https://aslopubs.onlinelibrary.wiley.com/doi/pdf/10.4319/lo.1998.43.5.0763. URL: https://aslopubs.onlinelibrary.wiley.com/doi/abs/10.4319/lo.1998.43.5.0763.

[50] Jorge L Sarmiento and Nicolas Gruber. *Ocean biogeochemical dynamics*. Princeton University Press, 2006.

[51] Kent A Fanning, Kendall L Carder, and Peter R Betzer. "Sediment resuspension by coastal waters: a potential mechanism for nutrient re-cycling on the ocean's margins". In: *Deep Sea Research Part A. Oceanographic Research Papers* 29.8 (1982), pp. 953–965.

[52] Sam C. Wainright. "Stimulation of heterotrophic microplankton production by resuspended marine sediments." In: *Science* 238 4834 (1987), pp. 1710–2.

[53] M Zavatarelli et al. "Diagnostic and prognostic model studies of the Adriatic Sea general circulation: Seasonal variability". In: *Journal of Geophysical Research: Oceans* 107.C1 (2002), pp. 2–1.

[54] M. Vichi et al. "Calibration and validation of a one-dimensional complex marine biogeochemical flux model in different areas of the northern Adriatic shelf". In: *Annales Geophysicae* 21.1 (2003).

[55] L. Tedesco et al. "NW Adriatic Sea biogeochemical variability in the last 20 years (1986?2005)". In: *Biogeosciences* 4.4 (2007), pp. 673–687. URL: `https://hal.archives-ouvertes.fr/hal-00297639`.

[56] Serena Fonda Umani and Alfred Beran. "Seasonal variations in the dynamics of microbial plankton communities: first estimates from experiments in the Gulf of Trieste, Northern Adriatic Sea". In: *Marine Ecology Progress Series* 247 (2003), pp. 1–16.

[57] Serena Fonda Umani et al. "Major inter-annual variations in microbial dynamics in the Gulf of Trieste (northern Adriatic Sea) and their ecosystem implications". In: *Aquatic Microbial Ecology* 46.2 (2007), pp. 163–175.

[58] LV Shannon and G Nelson. "The Benguela: large scale features and processes and system variability". In: *The south atlantic*. Springer, 1996, pp. 163–210.

[59] T Lamont et al. "Hydrographic variability in the S t. Helena Bay region of the southern Benguela ecosystem". In: *Journal of Geophysical Research: Oceans* 120.4 (2015), pp. 2920–2944.

[60] Gerhard Graf et al. “Benthic-pelagic coupling in the Greenland-Norwegian Sea and its effect on the geological record”. In: *Geologische Rundschau* 84.1 (1995), pp. 49–58.

[61] D Bianchi et al. “Simulations of ecosystem response during the sapropel S1 deposition event”. In: *Palaeogeography, Palaeoclimatology, Palaeoecology* 235.1-3 (2006), pp. 265–287.

[62] P Berrisford et al. “The ERA-Interim archive. Technical ERA report series 1, ECMWF”. In: *Reading, United Kingdom* (2009).

[63] Copernicus Climate Change Service (C3S). “ERA5: Fifth generation of ECMWF atmospheric reanalyses of the global climate”. In: (2017).

[64] Alfred Clarence Redfield. “On the proportions of organic derivatives in sea water and their relation to the composition of plankton”. In: *James Johnstone memorial volume* (1934), pp. 176–192.

[65] H Hersbach and D Dee. “ERA5 reanalysis is in production, ECMWF Newsletter 147, ECMWF”. In: *Reading, UK* (2016).

[66] Stefano Cozzi et al. “Recent evolution of river discharges in the Gulf of Trieste and their potential response to climate changes and anthropogenic pressure”. In: *Estuarine, Coastal and Shelf Science* 115 (2012), pp. 14–24.

[67] TS Hopkins et al. “A discussion of the northern Adriatic circulation and flushing as determined from the ELNA hydrography”. In: *The Adriatic Sea*. Vol. 32. European Commission Brussels, 1999, pp. 85–106.

[68] Pierre-Marie Poulain and Fabio Raicich. “Forcings”. In: *Physical Oceanography of the Adriatic Sea*. Springer, 2001, pp. 45–65.

[69] A Boldrin et al. “Effects of bora wind on physical and biogeochemical properties of stratified waters in the northern Adriatic”. In: *Journal of Geophysical Research: Oceans* 114.C8 (2009).

[70] Vassiliki H Kourafalou. “Process studies on the Po River plume, north Adriatic Sea”. In: *Journal of Geophysical Research: Oceans* 104.C12 (1999), pp. 29963–29985.

[71] Momme Butenschön, Marco Zavatarelli, and Marcello Vichi. “Sensitivity of a marine coupled physical biogeochemical model to time resolution, integration scheme and time splitting method”. In: *Ocean Modelling* 52 (2012), pp. 36–53.

[72] Serena Fonda et al. “Is it possible to identify any plankton succession in the Gulf of Trieste (Northern Adriatic Sea)?” In: (1996).

[73] B Cataletto et al. “Eleven years of time-series analysis on the net-zooplankton community in the Gulf of Trieste”. In: *ICES Journal of Marine Science* 52.3-4 (1995), pp. 669–678.

[74] P Mozetiĉ et al. “Seasonal and inter-annual plankton variability in the Gulf of Trieste (northern Adriatic)”. In: *ICES Journal of Marine Science* 55.4 (1998), pp. 711–722.

[75] Alenka Malej et al. “Phytoplankton responses to freshwater inputs in a small semi-enclosed gulf (Gulf of Trieste, Adriatic Sea)”. In: *Marine ecology progress series. Oldendorf* 120.1 (1995), pp. 111–121.

[76] TC Malone et al. “Influences of river flow on the dynamics of phytoplankton production in a partially stratified estuary.” In: *Marine ecology progress series. Oldendorf* 48.3 (1988), pp. 235–249.

[77] Thomas E Jordan et al. “Long-term trends in estuarine nutrients and chlorophyll, and short-term effects of variation in watershed discharge”. In: *Marine Ecology Progress Series* (1991).

[78] M Zavatarelli et al. “Climatological biogeochemical characteristics of the Adriatic Sea”. In: *Journal of Marine Systems* 18.1-3 (1998), pp. 227–263.

[79] A Hill et al. *Eastern ocean boundaries. InThe sea. II. The global coastal ocean*. 1998.

[80] FA Shillington et al. “4 Large scale physical variability of the Benguela Current Large Marine Ecosystem (BCLME)”. In: *Large marine ecosystems*. Vol. 14. Elsevier, 2006, pp. 49–70.

[81] G Nelson and L Hutchings. “The Benguela upwelling area”. In: *Progress in Oceanography* 12.3 (1983), pp. 333–356.

[82] Thomas D Potter, Bradley R Colman, et al. *Handbook of weather, climate, and water*. Wiley Online Library, 2003.

[83] L Hutchings et al. “St Helena Bay (southern Benguela) then and now: muted climate signals, large human impact”. In: *African Journal of Marine Science* 34.4 (2012), pp. 559–583.

[84] Andrew Bakun et al. “Anticipated effects of climate change on coastal upwelling ecosystems”. In: *Current Climate Change Reports* 1.2 (2015), pp. 85–93.

[85] CM Duncombe Rae, AJ Boyd, and RJM Crawford. “” Predation” of anchovy by an Agulhas ring: a possible contributory cause of the very poor year-class of 1989”. In: *South African Journal of Marine Science* 12.1 (1992), pp. 167–173.

[86] CM Duncombe Rae et al. “An Agulhas ring in the South Atlantic Ocean and its interaction with the Benguela upwelling frontal system”. In: *Deep Sea Research Part A. Oceanographic Research Papers* 39.11-12 (1992), pp. 2009–2027.

[87] PMS Monteiro et al. “Shellfish mariculture in the Benguela system: estimates of nitrogen-driven new production in Saldanha Bay using two physical models”. In: *Journal of Shellfish Research* 17.1 (1998), pp. 3–14.

[88] PMS Monteiro and J Ll Largier. “Thermal stratification in Saldanha Bay (South Africa) and subtidal, density-driven exchange with the coastal waters of the Benguela upwelling system”. In: *Estuarine, Coastal and Shelf Science* 49.6 (1999), pp. 877–890.

[89] GC Pitcher, PC Brown, and BA Mitchell-Innes. “Spatio-temporal variability of phytoplankton in the southern Benguela upwelling system”. In: *South African Journal of Marine Science* 12.1 (1992), pp. 439–456.

[90] Pedro MS Monteiro and Anja K van der Plas. “5 Low oxygen water (LOW) variability in the Benguela system: Key processes and forcing scales relevant to forecasting”. In: *Large Marine Ecosystems*. Vol. 14. Elsevier, 2006, pp. 71–90.

[91] L Hutchings. “Fish harvesting in a variable, productive environment—searching for rules or searching for exceptions?” In: *South African Journal of Marine Science* 12.1 (1992), pp. 297–318.

[92] Claude Roy. "An upwelling-induced retention area off Senegal: a mechanism to link upwelling and retention processes". In: *South African Journal of Marine Science* 19.1 (1998), pp. 89–98.

[93] Pedro MS Monteiro and Alakendra N Roychoudhury. "Spatial characteristics of sediment trace metals in an eastern boundary upwelling retention area (St. Helena Bay, South Africa): a hydrodynamic–biological pump hypothesis". In: *Estuarine, Coastal and Shelf Science* 65.1-2 (2005), pp. 123–134.

[94] GC Pitcher, DR Walker, and BA Mitchel-Innes. "Phytoplankton sinking rate dynamics in the southern Benguela upwelling system." In: *Marine ecology progress series. Oldendorf* 55.2 (1989), pp. 261–269.

[95] Osmund Holm-Hansen et al. "Fluorometric determination of chlorophyll". In: *ICES Journal of Marine Science* 30.1 (1965), pp. 3–15.

[96] KR Ridgway, JR Dunn, and JL Wilkin. "Ocean interpolation by four-dimensional weighted least squares—Application to the waters around Australasia". In: *Journal of atmospheric and oceanic technology* 19.9 (2002), pp. 1357–1375.

[97] PMS Monteiro et al. "Interannual hypoxia variability in a coastal upwelling system: Ocean–shelf exchange, climate and ecosystem-state implications". In: *Deep Sea Research Part I: Oceanographic Research Papers* 55.4 (2008), pp. 435–450.

[98] Stephanie de Villiers. *Biogeochemical climatology for the Southern Benguela Upwelling System, constructed from in situ monthly monitoring data collected from 2001 to 2012*. data set. Department of

Environmental Affairs, 2017. DOI: 10.1594/PANGAEA.882218. URL: https://doi.org/10.1594/PANGAEA.882218.

[99] Bjørn Helland-Hansen and Fridtjof Nansen. *The Norwegian Sea: its physical oceanography based upon the Norwegian researches 1900-1904*. Det Mallingske bogtrykkeri, 1909.

[100] Kjell Arild Orvik and Martin Mork. "Atlantic water transport from long term current measurements in the Svinoy section". In: *ICES Annual Science Conference, Reykjavik, Iceland, CM*. 1996.

[101] H Haakenstad and JE Haugen. "A 15-year high resolution meteorological". In: (2017).

[102] Kenneth Henry Mann and John RN Lazier. *Dynamics of marine ecosystems: biological-physical interactions in the oceans*. John Wiley & Sons, 2013.

[103] Ahmed Ibrahim et al. "Seasonal variations of the surface nutrients and hydrography in the Norwegian Sea". In: *International Journal of Environmental Science and Development* 5.5 (2014), p. 496.

[104] Kjell Arild Orvik and Øystein Skagseth. "The impact of the wind stress curl in the North Atlantic on the Atlantic inflow to the Norwegian Sea toward the Arctic". In: *Geophysical Research Letters* 30.17 (2003). DOI: 10.1029/2003GL017932.

[105] Harald Loeng and Ken Drinkwater. "An overview of the ecosystems of the Barents and Norwegian Seas and their response to climate variability". In: *Deep Sea Research Part II: Topical Studies in Oceanography* 54.23-26 (2007), pp. 2478–2500.

[106] EG Atkinson and JW Wacasey. "Sedimentation in Arctic Canada: particulate organic carbon flux to a shallow marine benthic community in Frobisher Bay". In: *Polar biology* 8.1 (1987), pp. 3–7.

[107] PAUL Wassmann. "Dynamics of primary production and sedimentation in shallow fjords and polls of western Norway". In: *Oceanogr Mar Biol Annu Rev* 29 (1991), pp. 87–154.

[108] Keith A Hobson, William G Ambrose Jr, and Paul E Renaud. "Sources of primary production, benthic-pelagic coupling, and trophic relationships within the Northeast Water Polynya: insights from δ13C and δ15N analysis". In: *Marine Ecology Progress Series* 128 (1995), pp. 1–10.

[109] Francesca Pianosi et al. "Sensitivity analysis of environmental models: A systematic review with practical workflow". In: *Environmental Modelling & Software* 79 (2016), pp. 214–232.

[110] Jason K Jolliff et al. "Summary diagrams for coupled hydrodynamic-ecosystem model skill assessment". In: *Journal of Marine Systems* 76.1-2 (2009), pp. 64–82.

[111] Watson W Gregg et al. "Skill assessment in ocean biological data assimilation". In: *Journal of Marine Systems* 76.1-2 (2009), pp. 16–33.

[112] Karl E Taylor. "Summarizing multiple aspects of model performance in a single diagram". In: *Journal of Geophysical Research: Atmospheres* 106.D7 (2001), pp. 7183–7192.

[113] Craig A Stow et al. "Skill assessment for coupled biological/physical models of marine systems". In: *Journal of Marine Systems* 76.1-2 (2009), pp. 4–15.

[114] Katja Fennel et al. "Testing a marine ecosystem model: sensitivity analysis and parameter optimization". In: *Journal of Marine Systems* 28.1-2 (2001), pp. 45–63.

[115] Liana Zambresky. *A verification study of the global WAM model: December 1987-November 1988*. na, 1989.

[116] Lorenzo Mentaschi et al. "Problems in RMSE-based wave model validations". In: *Ocean Modelling* 72 (2013), pp. 53–58.

[117] Steven R Hanna and David W Heinold. *Development and application of a simple method for evaluating air quality models*. 4409. American Petroleum Institute, 1985.

[118] Ket Fedra et al. "On the ecology of a North Adriatic benthic community: distribution, standing crop and composition of the macrobenthos". In: *Marine Biology* 38.2 (1976), pp. 129–145.

[119] V Solis-Weiss et al. "A regional GIS for benthic diversity and environmental impact studies in the Gulf of Trieste, Italy". In: *Proceedings of the Colour of Ocean Data: International Symposium on Oceanographic Data and Information Management with Special Attention to Biological Data (IOC Workshop Report 188). UNESCO, Paris*. 2004, pp. 245–255.

[120] Vivianne Solis-Weiss et al. "The benthic macrofauna at the outfalls of the underwater sewage discharges in the Gulf of Trieste (northern

Adriatic Sea)". In: *Annales, Series Historia Naturalis*. Vol. 17. 2007, pp. 1–16.